



TECHNISCHE  
UNIVERSITÄT  
DRESDEN

DRESDEN  
concept



Fakultät Mathematik und Naturwissenschaften, Institut für Festkörperphysik

# MODELLING AND DESIGN OF HIGH COMPRESSION ELECTRON GUNS FOR EBIS/T CHARGE BREEDERS

Robert Mertzig

Dissertation  
zur Erlangung des wissenschaftlichen Grades  
Doktor rerum naturalium

vorgelegt von

Robert Mertzig  
geboren am 05.03.1984 in Finsterwalde

Institut für Festkörperphysik  
der Technischen Universität Dresden  
2016

Eingereicht am 18.05.2016

1. Gutachter: Prof. Dr. J. Fassbender
2. Gutachter: PD Dr. G. Zschornack
3. Gutachter: Dr. J. Lettry

## Abstract

In der vorliegenden Arbeit wird die Optimierung des REXEBIS-Ladungsbrüters an der ISOLDE präsentiert. Die REXEBIS in der aktuellen Konfiguration erzeugt eine Elektronenstromdichte in der Fallenregion bei 2 T von 200 A/cm<sup>2</sup> und wird bis zu ihren physikalischen Grenzen optimiert.

Um diese Begrenzung zu überwinden wurde eine neue Elektronenkanone, die HEC<sup>2</sup>-Elektronenkanone, in Kooperation mit BNL konstruiert und an der TestEBIS in Betrieb genommen. Diese Elektronenkanone verspricht eine Elektronenstromdichte von mehr als 10 kA/cm<sup>2</sup> bei 5 T, welche die Ladungsbrütungszeit entscheidend verkürzt. In dieser Dissertation werden neuartige Simulationstechniken vorgestellt, welche die Inbetriebnahme durch Untersuchung der Mechaniken von auftretenden Verlustströmen beschreiben. Dazu wird der Elektronenkollektor der TestEBIS nach Kompatibilität bezüglich der HEC<sup>2</sup>-Elektronenkanone, die nahe derer Designwerte betrieben wird, evaluiert.

Die gewonnenen Erfahrungen von der Inbetriebnahme der HEC<sup>2</sup>-Elektronenkanone und den etablierten, numerischen Techniken führen zur Entwicklung einer kleineren hochkomprimierenden Elektronenkanone für medizinische Anwendungen, die MEDeGUN. Diese Elektronenkanone sollte einen qualitativ hochwertigen Elektronenstrahl generieren, welcher eine Elektronenstromdichte von 7.5 kA/cm<sup>2</sup> in der Fallenregion bei 5 T axialen Magnetfeld erzeugt. Eine EBIS/T, ausgestattet mit einer MEDeGUN, wird bezüglich Pulsfrequenz und bereitgestellten Ionenstrom zu Hochfrequenz-Therapiezentren der zweiten Generation kompatibel sein.

## Abstract

In this thesis the optimization of the REXEBIS charge breeder at the ISOLDE facility is presented. REXEBIS in its current state provides a current density of 200 A/cm<sup>2</sup> inside the trapping region at 2 T and will be optimized to the physical limit of its design.

To overcome this limit a new electron gun, the HEC<sup>2</sup> gun, was designed in collaboration with the BNL and is in commission at TestEBIS. This electron gun promises a current density of >10 kA/cm<sup>2</sup>, which decreases the charge breeding time significantly. This thesis presents novel simulation techniques supporting the commissioning phase by explaining the sources of occurring loss current and, in addition, evaluate the currently installed collector for compatibility with the HEC<sup>2</sup> gun operating at its design limit.

The experience gained from the commission of the HEC<sup>2</sup> gun and the established numerical techniques lead to the development of a smaller high-compression electron gun for medical purposes, the MEDeGUN. This electron gun should provide a high-quality beam, which generates a calculated current density of 7.5 kA/cm<sup>2</sup> inside the trapping region immersed in a 5 T axial magnetic field. An EBIS/T equipped with a MEDeGUN will be compatible regarding the pulse frequency and deliver the mandatory ion current required for second generation therapy centers.



"Habe nun, ach! Philosophie,  
Juristerey und Medicin,  
Und leider auch Theologie!  
Durchaus studirt, mit heißem Bemühn.  
Da steh' ich nun, ich armer Thor!  
Und bin so klug als wie zuvor;  
[...]

O sähst du, voller Mondenschein,  
Zum letztenmal auf meine Pein,  
Den ich so manche Mitternacht  
An diesem Pult herangewacht:  
Dann über Büchern und Papier,  
Trübsel'ger Freund, erschienst du mir!"

Faust - Der Tragödie erster Teil (1808), J.W. von Goethe

# CONTENTS

|       |   |    |
|-------|---|----|
| 1     | Introduction  | 1  |
| 1.1   | List of acronyms . . . . .                          | 3  |
| 1.2   | List of symbols . . . . .                           | 4  |
| 2     | Theory  | 5  |
| 2.1   | The Electron Beam Ion Source/Trap . . . . .         | 5  |
| 2.2   | Physical processes . . . . .                        | 6  |
| 2.2.1 | Charge breeding processes . . . . .                 | 6  |
| 2.2.2 | Charge breeding dynamics . . . . .                  | 6  |
| 2.2.3 | Secondary electrons . . . . .                       | 7  |
| 2.2.4 | Back-scattered electrons . . . . .                  | 8  |
| 2.3   | Electron gun physics . . . . .                      | 8  |
| 2.3.1 | Immersed electron gun . . . . .                     | 9  |
| 2.3.2 | Brillouin electron gun . . . . .                    | 9  |
| 2.4   | Cathode physics . . . . .                           | 11 |
| 2.4.1 | Emission regimes . . . . .                          | 11 |
| 2.4.2 | The work function . . . . .                         | 12 |
| 2.4.3 | Cathode roughness . . . . .                         | 12 |
| 2.5   | Electron beam dynamics in magnetic fields . . . . . | 13 |
| 2.5.1 | Magnetic mirror effect . . . . .                    | 13 |
| 2.5.2 | The Bursian limit . . . . .                         | 14 |
| 2.5.3 | Electron beam radius . . . . .                      | 14 |
| 2.5.4 | Two stream plasma instability . . . . .             | 15 |
| 2.5.5 | Electron beam quality . . . . .                     | 15 |

|       |  |    |
|-------|--|----|
| 3     | Automatized calculation of ionization potentials             | 17 |
| 4     | Computational physics  | 21 |
| 4.1   | General numerical recipes . . . . .                          | 21 |
| 4.1.1 | Meshing . . . . .  | 21 |
| 4.1.2 | Time steps . . . . .   | 22 |
| 4.1.3 | The residual value . . . . .                                 | 22 |
| 4.1.4 | Convergence . . . . .  | 23 |
| 4.1.5 | Cluster calculation . . . . .                                | 23 |
| 4.2   | Optimization of the simulation via volume division . . . . . | 24 |
| 4.2.1 | The technique . . . . .                                      | 25 |
| 4.2.2 | Errors due to volume slicing . . . . .                       | 28 |
| 4.3   | Applications . . . . .                                       | 29 |
| 4.3.1 | Side-emission from the electron cathode . . . . .            | 29 |
| 4.3.2 | Mixed regime emission . . . . .                              | 30 |
| 4.3.3 | Particle microscope . . . . .                                | 31 |
| 4.3.4 | Back-scattered electrons . . . . .                           | 33 |
| 5     | Characterization of TwinEBIS                                 | 37 |
| 5.1   | TwinEBIS - Machine description . . . . .                     | 37 |
| 5.2   | The LaB <sub>6</sub> cathode . . . . .                       | 39 |
| 5.3   | The IrCe cathode . . . . .                                   | 43 |
| 5.4   | Poisoning effects on LaB <sub>6</sub> . . . . .              | 45 |
| 5.4.1 | Cathode revival using oxygen . . . . .                       | 45 |
| 5.4.2 | Effects of hydrocarbons on the cathode . . . . .             | 46 |
| 5.4.3 | Effects of neon on LaB <sub>6</sub> . . . . .                | 47 |
| 5.5   | Alignment dependent current losses . . . . .                 | 48 |
| 5.6   | Approaching the design value of REXEBIS . . . . .            | 50 |

|       |   |    |
|-------|---|----|
| 6     | Simulations of the HEC <sup>2</sup> gun                           | 53 |
| 6.1   | TestEBIS - machine description . . . . .                          | 53 |
| 6.2   | Evaluation of the loss current occurring at the anode . . . . .   | 54 |
| 6.2.1 | Side-emission of the cathode . . . . .                            | 55 |
| 6.2.2 | Reflection of the side-emitted current . . . . .                  | 58 |
| 6.2.3 | Results . . . . .   | 61 |
| 6.3   | Optimization of the TestEBIS collector . . . . .                  | 61 |
| 6.3.1 | Investigations of ERPE inside the collector . . . . .             | 63 |
| 6.3.2 | Investigations of the power deposition inside the collector . . . | 65 |
| 6.3.3 | Investigations of the redistribution of deposited power by BSE    | 66 |
| 6.3.4 | Suggested collector geometry . . . . .                            | 68 |
| 6.4   | Summary of the HEC <sup>2</sup> -simulation results . . . . .     | 70 |
| 7     | Design of MEDeGUN   | 71 |
| 7.1   | Design . . . . .  | 71 |
| 7.2   | 1 <sup>st</sup> order characteristics . . . . .                   | 73 |
| 7.3   | Influence of electron temperature . . . . .                       | 75 |
| 7.4   | Influence of the Wehnelt potential . . . . .                      | 77 |
| 7.5   | Setting of the electron gun compensation coils . . . . .          | 77 |
| 7.6   | Sensitivity of the design to mechanical tolerances . . . . .      | 79 |
| 7.6.1 | Influence of the axial position of the gun assembly . . . . .     | 82 |
| 7.6.2 | Summarized error discussion . . . . .                             | 83 |
| 7.7   | MEDeGUN versus HEC <sup>2</sup> . . . . .                         | 84 |
| 7.8   | Modification of the TwinEBIS collector . . . . .                  | 86 |
| 7.9   | Beam transport into high B-field . . . . .                        | 87 |
| 7.10  | Charge-breeding efficiency . . . . .                              | 90 |
| 8     | Conclusion and outlook  | 92 |

|     |   |    |
|-----|---|----|
| A   | Appendix                                      | 94 |
| A.1 | Derivation of reflection conditions . . . . . | 94 |
| A.2 | Permeability of ARMCO iron . . . . .          | 96 |
|     | Bibliography                                  | 97 |

# 1 Introduction

Highly Charged Ions (HCI) are widely used in scientific, medical and industrial fields. Their charge makes HCI attractive for accelerator related applications [Beyer et al. 1997] and suitable for evaluating theories in quantum electrodynamics, such as electron-electron interaction or scattering effects [von Lindenfels et al. 2013, Zaytsev et al. 2015]. For medical applications such as light hadron therapy ions are suitable for their biological effectiveness [Zschornack et al. 2009]. HCI are used in industry for doping semi-conductor wavers [Williams and Poate 1984] and producing meta materials [Chowdhury et al. 2013].

The most common machine types for producing HCI are here Electron Cyclotron Resonance Ion Sources (ECRIS) and Electron Beam Ion Sources or Traps (EBIS/T), where the ionization is carried out by electron impact ionization. The general principle of an EBIS/T is shown in Fig. 1.0.1. An indirect method is foil stripping of lowly charged ions. While ECRIS sources produce a high current ion beam with a stable background contamination, EBIS/T generate more rapidly HCI of less current but with a smaller contamination [Vondrasek et al. 2012]. An ion source in combination with a stripping foil has the advantage of high current emission of HCI on the costs of a pre-accelerator for a high  $A/q$  value between source and stripping foil [Ames et al. 2006].

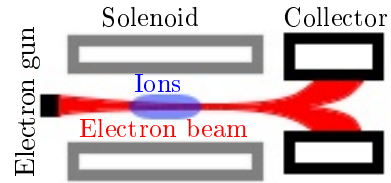


Figure 1.0.1: A general sketch of an EBIS/T. The electron beam **electron beam** is emitting from the electron gun, gets compressed by the magnetic field of the solenoid and recovered in the collector. **Ions** are generated and confined in the trapping region.

Beside the generation of ions, HCI sources can be used for charge breeding as in **R**adioactive **I**on **E**eam (RIB) facilities where nuclei are used for experiments investigating nuclear structure properties [Gaffney et al. 2013]. The ISOLDE facility at CERN for instance specializes in investigations of exotic isotopes, neutron- or proton-rich, produced in targets by proton-matter interaction. These radioactive isotopes are charge bred to match the  $A/q$  value between 2.5 and 4.5 before being injected into an accelerator [Borge 2016]. The charge breeding time should be as short as possible to minimize decay losses. This requirement becomes especially important when focusing on exotic nuclei far off the line of stability with very short half-lives.

At the ISOLDE facility the charge breeding is realized by REXEBIS equipped with an immersed electron gun, which provides an electron current beam of 250 mA at an electron energy of 4.5 keV, which results in a current density of 200 A/cm<sup>2</sup> in the trapping region at 2 T [Wolf et al. 2003]. This thesis treats the optimization of

the current density towards the immersed gun limit of on-line REXEBIS. An off-line replica, the TwinEBIS setup, was assembled to allow development and research without interfering with user experiments at ISOLDE. At TwinEBIS the physical limits of the REXEBIS design were investigated and its ability to generate an electron beam at and above the design value of 500 mA emission current under stable conditions was studied. Immersed electron guns are reliable and provide medium-density electron beams of several 100 A/cm<sup>2</sup>. The compression of the electron beam provided by this type of gun is governed by the ratio between the magnetic field at the cathode and inside the trapping volume [Becker and Kester 2012].

To overcome this limit and to achieve higher current densities a Brillouin electron gun is used. In this gun the cathode is shielded from the magnetic field of the solenoid. First the emitted electron beam is electrostatically compressed inside the electron gun and then injected into a magnetic field, where the beam is compressed further, similar to the compression taking place in immersed guns. The obtained current densities are in the order of a few kA/cm<sup>2</sup>, and thus significantly higher than in an immersed gun [Shornikov et al. 2013]. The shorter breeding times make an EBIS/T equipped with a Brillouin gun highly attractive for medical applications, where a rapid production of HCI is required [Amaldi et al. 2009]. Because of the difficulties to inject the electron beam into the magnetic field the Brillouin electron gun is highly challenging to design and to operate.

A High Energy Compression and Current (HEC<sup>2</sup>) gun, capable of providing an electron current density of > 10 kA/cm<sup>2</sup> in a 5 T solenoid, is studied in the frame of the HIE-ISOLDE upgrade at CERN [Shornikov et al. 2015]. This electron gun capable of generating an electron beam of 10 A with an electron energy of 49 keV is being developed in a cooperation between CERN and Brookhaven National Laboratory (BNL) and is currently under commission at the TestEBIS setup at BNL.

Excessive loss current on the anode power supply occurred during the commission and prevent the HEC<sup>2</sup> gun from operating according to its design values [Pikin et al. 2014]. These terminating electrons do not directly reach this electrode from the cathode. One explanation is the reflection of electrons at the magnetic field gradient. These reflected electrons return towards the electron gun and terminate on the anode. To numerically investigate the reflection, this electron beam has to be traced  $\approx$  1 m into the magnetic field gradient and back. Supportive numerical methods are developed and presented in this thesis to simulate the reflection in such a remote area. These methods allow to investigate the electron beam propagation in an extended volume, for instance a complete ion source. This extended tracing includes correct modeling of beam emission at the cathode, beam compression respectively propagation in high magnetic fields and the recovery in the collector. In addition, it has to be ensured that the installed collector is capable of recovering the electron beam generated by the HEC<sup>2</sup> gun operating at its design values. For this the electron beam propagation and the correlated power deposition considering secondary electron processes are simulated, evaluated and discussed in this thesis.

The experience gained during the commissioning of the HEC<sup>2</sup> gun has been used to develop a down-scaled high-compression electron gun for medical purposes, called MEDeGUN. This device is compatible to all medical accelerators such as cyclotron linacs [Garonna et al. 2010] and high frequency linacs [Vretenar et al. 2014], which demand pulses of  $\approx 10^9$  C<sup>6+</sup> ions at a frequency of 400 Hz. MEDeGUN should generate an electron beam of 1 A with an extraction potential of 10 kV, resulting in a current density of 7.5 kA/cm<sup>2</sup> in a magnetic field of 5 T allowing rapid charge breeding. The focus of the design is the electron beam quality as well as sufficient safety margins for the mechanical design. This ensures easy gun assembly and operation. The design and properties of the MEDeGUN will be discussed in detail in the final chapter. An brief overview of the EBIS/T and the focus of this work is shown in Fig. 1.0.2.

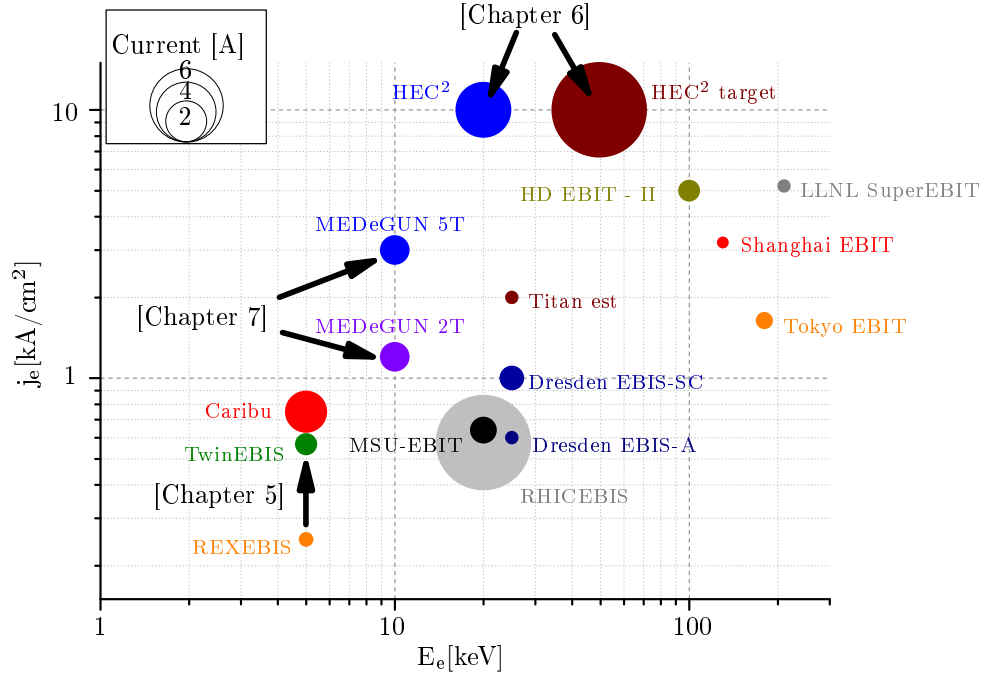


Figure 1.0.2: An overview of the different sources and the EBIT/T-types treated in this thesis.

## 1.1 List of acronyms

|                  |   |
|------------------|---|
| EBIS/T           | Electron Beam Ion Source / Trap         |
| ISOLDE           | Isotope Separator On Line DEvice        |
| REX-ISOLDE       | Radioactive Beam EXperiment at ISOLDE   |
| HIE-ISOLDE       | High Intensity and Energy - ISOLDE      |
| HEC <sup>2</sup> | High Energy Current and Compression     |
| PE               | Primary Electrons                       |
| SE               | Secondary Electrons                     |
| BSE              | Back-Scattered Electrons                |
| SEE              | Side-Emitted Electrons                  |
| ERPE             | Elastically Reflected Primary Electrons |
| FP               | Field Precision                         |



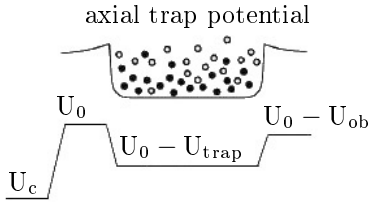
## 1.2 List of symbols

| general            |   | potentials                     |                                |
|--------------------|---|--------------------------------|--------------------------------|
| $k_B$              | Boltzmann's constant                    | $U_c$                          | cathode                        |
| $\mu$              | magnetic momentum                       | $U_0$                          | reference                      |
| $\epsilon$         | emissivity                              | $U_{\text{trap}}$              | trap                           |
| $A$                | surface                                 | $U_{\text{ob}}$                | outer-barrier                  |
| $A_R$              | Richardson constant                     | $U_{\text{sc}}$                | space-charge                   |
| $t$                | time                                    | $U_{\text{an}}$                | anode                          |
| $\tau$             | ionization time                         | $U_{\text{dt}}$                | drift-tube                     |
| $E$                | electric field $\perp$ surface          | $U_{\text{coll}}$              | collector                      |
| $B$                | magnetic field strength                 | $U_{\text{rep}}$               | repeller                       |
| $B_c$              | magnetic field strength on cathode      | $U_{\text{ext}}$               | collector extractor            |
| $B_0$              | matching magnetic field                 | $U_{\text{ex}}$                | extraction                     |
| $I_e$              | electron current                        | $U_{\text{ldt}}$               | last drift tube                |
| $I_B$              | Bursian-limited electron current        | $U_{\text{ib}}$                | inner-barrier                  |
| $I_{\text{loss}}$  | loss current                            | $U_w$                          | Wehnelt                        |
| $I_{\text{coll}}$  | current deposited on the collector      | dimensions                     |                                |
| $E_e$              | kinetic electron energy                 | $r_e$                          | electron-beam radius           |
| $T_{c,m}$          | measured cathode temperature            | $r_B$                          | Brillouin radius               |
| $T_c, T_{c,t}$     | true cathode temperature                | $r_H$                          | Herrmann radius                |
| $j_e$              | current density                         | $r_L$                          | Larmor radius                  |
| $j_{e,0}$          | maximum current density                 | $r_{f,\text{min}}$             | $r_e$ in the focus point       |
| $\omega_c$         | cyclotron frequency                     | $\Delta r_e$                   | electron-beam ripple-size      |
| $\omega_p$         | plasma frequency                        | $r_{\text{dt}}$                | drift tube radius              |
| $\Phi$             | work function                           | $r_c$                          | cathode radius                 |
| $\Delta\Phi$       | work-function correction                | $r_{\text{an}}$                | anode hole radius              |
| $P_d$              | power density                           | $d_{\text{cw}}$                | gap between cathode-Wehnelt    |
| numerics           |   | $r, z$                         | position                       |
| $r_i^n$            | residual value                          | $dr, dz$                       | volume length, height          |
| $\Phi_i$           | space-charge solution                   | $dz(t)$                        | axial distance per time step   |
| $I_i$              | ionization potential                    | $\Delta x, \Delta y, \Delta r$ | misalignment                   |
| $\bar{\epsilon}_r$ | emittance                               | $\Delta z_c$                   | axial cathode shift            |
| $\Theta$           | angle between BSE and surface           | $\Delta r_{\text{cwa}}$        | misalignment cathode vs. anode |
| $B(\Theta)$        | angular dependent weighting factor(BSE) | $\Delta d_{\text{an}}$         | anode hole error               |
|                    |   | $\Delta_m r, \Delta_m z$       | radial/axial mesh size         |
|                    |   | $\Delta z_c$                   | cathode roughness              |

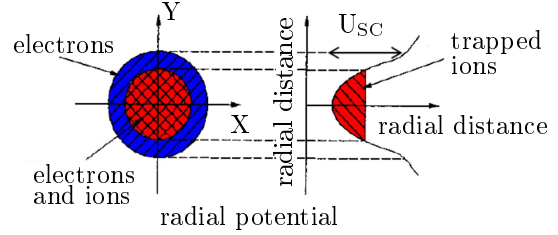
## 2 Theory

### 2.1 The Electron Beam Ion Source/Trap

An EBIS/T generates ion by electron impact ionization and confines ions via the space charge field of the electron beam, which is compressed by a high solenoidal magnetic field. The axial confinement is ensured by applying potentials at the outer drift tubes for setting up an axial potential trap, see Fig. 2.1.1(a). The radial confinement, shown in Fig 2.1.1(b), is mainly established by the space charge field of the compressed electron beam, which is highly attractive for positively charged ions.



(a) Axial potential distribution of an electron beam. The cathode is on a potential  $U_c$ , which is lower than the reference potential  $U_0$ . The axial trap is realized by a potential  $U_{\text{trap}}$ . For injecting and ejecting ions, the trap can be opened and closed by adjusting the corresponding potential  $U_{\text{ob}}$  on the last drift tube.



(b) Radial confinement of ions. The potential distribution of an electron beam is dependent on the trap/beam geometry, which determines the electric field distribution.

Figure 2.1.1: Confinement in radial and axial direction of ions inside an EBIS/T

The radial potential generated by the electron beam,  $U_{\text{sc}}$ , can be described as:

$$U_{\text{sc}}[\text{V}] = \frac{I_e[\text{A}]}{4\pi\epsilon_0 \sqrt{1 - \left(\frac{E_e[\text{keV}]}{511} + 1\right)^{-2}}} \times \begin{cases} \frac{r_e^2}{r_e^2}, & r < r_e \\ \left(2\ln\frac{r}{r_e} + 1\right), & r > r_e \end{cases} \quad (2.1.1)$$

with  $E_e$  being the kinetic energy of the electron beam,  $I_e$  the electron beam current,  $r_e$  the electron beam radius and  $\epsilon_0$  the vacuum permittivity.

## 2.2 Physical processes

### 2.2.1 Charge breeding processes

The charge breeding process in an EBIS/T is mainly driven by single electron impact ionization, radiative recombination and charge exchange. The cross section of a single electron impact ionization can be described with the Lotz equation [Lotz 1970]. The cross section  $\sigma_{SI}$  is the sum of the cross sections of each sub-shell  $i$ .  $E_e$  is the energy of the incident electron in [eV],  $I_i$  is the ionization potential of the specific sub-shell in [eV],  $q_i$  is the electron occupation of the sub-shell,  $q$  as the charge state and  $a, b$  and  $c$  are tabled constants.

$$\sigma_{SI} [\text{cm}^2] = \sum_{i=1}^N a_i \cdot q_i \frac{\ln(E_e/I_i)}{E_e \cdot I_i} (1 - b_i \cdot e^{-c_i [E_e/I_i - 1]}) \quad (2.2.1)$$

The radiative recombination as the dominating recombination process can be semi-empirically described by the equation

$$\sigma_{RR}^q [\text{cm}^2] = \frac{8\pi}{3\sqrt{3}} \alpha \lambda_e^2 \chi_q \ln \left( 1 + \frac{\chi_q}{2\hat{n}} \right), \quad (2.2.2)$$

which was derived by Kim and Pratt [Kim and Pratt 1983]. In this equation,  $\chi_q = (Z + q)^2 \frac{I_H}{4E_e}$ ,  $I_H = 13.6 \text{ eV}$ ,  $\alpha \approx 1/137.037$ ,  $\lambda_e = 2.426 \cdot 10^{-10} \text{ cm}$  and the effective quantum number is defined as  $\hat{n} = n + (1 - W_n) - 0.3$  with  $W_n$  as the number of non-occupied states.

The third dominating process is the charge exchange between the confined ions. The charge exchange can be expressed by the semi-empirical equation by Müller and Salzborn [Mueller and Salzborn 1977]:

$$\sigma_{q \rightarrow q-1} [\text{cm}^2] \approx (1.43 \pm 0.76) \cdot 10^{-12} q_i^{1.17} I_i^{-2.76} \quad (2.2.3)$$

Here,  $q_i$  is the initial charge state of the projectile ion and  $I_i$  is the ionization potential of the target ion.

### 2.2.2 Charge breeding dynamics

The time dependent evolution of ions of an observed charge state  $q$  in an EBIS/T can be described by this rate equation, which detailed in [Mertzig 2011, p. 17f]:

$$\frac{dN^q}{dt} = N^{q-2}\lambda^{q-2} + N^{q-1}\lambda^{q-1} - N^q\lambda^q + N^{q+1}\lambda^{q+1} + N^{q+2}\lambda^{q+2} \quad (2.2.4)$$

$$\lambda^{q-1} = \textcolor{red}{j}_e \sigma_{\text{SI}}^{q-1 \rightarrow q} + \lambda^{*,q-1} \quad (2.2.5)$$

Here,  $\lambda$  are the summarized rate coefficients including all physical processes occurring during the charge-breeding process, such as single/double electron impact ionization, charge exchange, recombination and other processes. Re-expressing  $\lambda^{q-1}$  for separately showing  $\sigma_{\text{SI}}^{q-1 \rightarrow q}$  as the dominating single-electron impact-ionization process reveals that the ionization rate linearly depends on the current density  $j_e$ . Here,  $\lambda^{*,q-1}$  is the residual rate coefficient without the separately expressed ionization process. Only considering single ionization one can express the total ionization time  $\bar{\tau}_q$  for an ion of a charge state  $q$  as [Wenander 2014]:

$$\bar{\tau}_q = \sum_{i=1}^{q-1} \bar{\tau}_{i \rightarrow i+1} = \frac{e}{\textcolor{red}{j}_e} \sum_{i=1}^{q-1} \frac{1}{\sigma_{\text{SI}}^{i \rightarrow i+1}} \quad (2.2.6)$$

### 2.2.3 Secondary electrons

Secondary electrons (SE) are generated by atom-electron interaction, when fast electrons penetrate into a solid. The transferred energy excites electrons in the valence or conduction band of the penetrated solid. If the transferred energy is higher than the work function, those electrons are able to escape into the vacuum. Their kinetic energy is in the range of few 10 eV [Singh et al. 2002] and are therefore called “slow SE”. A second process of SE generation is the Auger process, where the penetrating electrons transfer enough energy to an electron bound in the inner sub-shells of an atom to eject the electron into the vacuum. The created inner-shell vacancy will be compensated by electrons from the outer shells. Owing to energy re-distribution during the reorganization process the least bound electron can also receive enough energy to escape into the vacuum. Their kinetic energy is in general higher than for slow SE [Lander 1953] and thus they are called “fast SE”.

In the case of accelerator beam-lines or EBIS/T collectors, the emitted SE build up an electron bulk in front of the emission surface [Furman and Pivi 2002, Pimpec et al. 2003]. That electron cloud creates a background potential in front of the surface.

### 2.2.4 Back-scattered electrons

Back-scattered electrons (BSE) occur when electrons from the primary beam (PE) intercept the solid, scatter inelastically at the atoms and re-emit into the vacuum. The energy distribution of BSE has a peak at a fraction of the incident energy. The peak position depends on the material and reaches about 80% for such collector materials as copper. The peak position shifts to higher values for heavier elements [Ali and Rogers 2008, Darlington and Cosslett 1972, Fang and Fukuda 2009, Gruzin et al. 1972, Hershcovitch and Kponou 1993, Matsukawa et al. 1974, Staub 1994, Sternglass 1954, Werner et al. 1982]. The peak of the angular distribution of the re-emission obeys optical reflection ( $\theta_{\text{in}} = \theta_{\text{out}}$ ) in combination with diffuse Lambert emission [Ali and Rogers 2008, Darlinkski 1981, Valfells et al. 2002]. As opposed to secondary electrons, BSE have due to the higher kinetic energy a significant contribution to the power redistribution and current loss inside an EBIS/T. The average kinetic energy of BSE is sufficient to re-enter the trap region in an EBIS/T, so they are capable of reaching the anode and impose loss current.

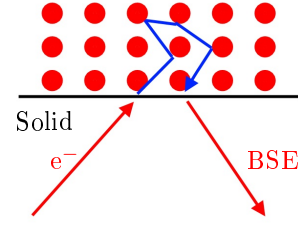


Figure 2.2.1: A general sketch of the back-scattering of electrons impinging a solid.

## 2.3 Electron gun physics

The characteristics of an electron beam in an EBIS/T depend on the physical environment of the electron generating device. Two major approaches for generating an electron beam have been established: the immersed and the Brillouin electron beam. Both approaches will be introduced in the following sections.

The immersed gun can be designed, built and operated with relatively low technical effort, because the electrons are guided by the applied B-field as soon they leave the cathode surface. The disadvantage of this realization is the low compression factor of the electron beam, which depends on the B-fields at the cathode and in the trap region.

In the Brillouin electron gun design the cathode is shielded from the magnetic field, which is realized either by a compensation coil or with an iron shield. The electron beam is compressed in two stages. In the first stage the electron beam is compressed purely by the electrostatic field inside the gun. When passing the anode and entering the magnetic field, the electrostatically compressed beam is frozen by the magnetic field. The final beam compression is therefore the product of electrostatic and magnetic compression, which is usually higher than the compression achieved with an immersed electron gun.

### 2.3.1 Immersed electron gun

With immersed electron guns the cathode is exposed to an axial magnetic field  $B_z$ , which counteracts the space-charge caused defocusing effect of the generated electron beam. The electrons are pinned to their corresponding magnetic field lines. The motion of the beam envelope can be expressed as

$$\frac{d^2R}{dZ^2} = \left( \frac{\omega_p}{\gamma\omega_c} \right)^2 \frac{1}{2R} - \frac{R}{4} \left( 1 - \frac{1}{R^4} \right) \quad (2.3.1)$$

with  $\omega_c = \frac{eB}{\gamma m_e}$  being the magnetic gyro frequency,  $\omega_p = \sqrt{\frac{e^2 n_0}{\gamma m_e \epsilon_0}}$  the plasma frequency,  $R = \frac{r}{r_0}$  the ratio between the beam radius  $r$  and the beam radius at the injection point into the magnetic field  $r_0$ , and  $Z = \frac{z\omega_c}{\beta c}$  the normalized axial position [Humphries 2013, p. 441]. This equation is valid for a paraxial electron beam with a current below the space-charge limit, where all electrons have the same kinetic energy. According to Eq. 2.3.1 the beam oscillation is zero, when  $\omega_p = 0$ . A typical electron beam of an immersed electron gun is shown in Fig. 2.3.1.

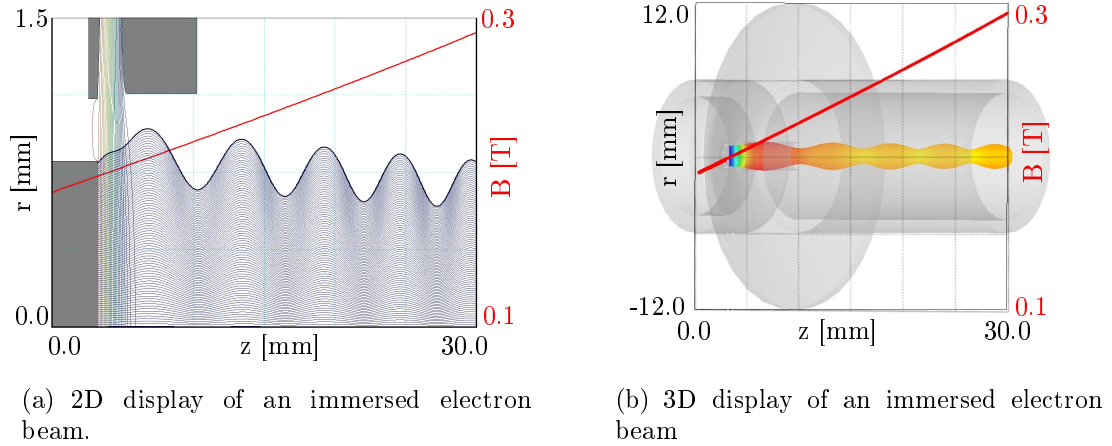


Figure 2.3.1: Simulation of an electron beam in TwinEBIS, as an example from an immersed gun.

### 2.3.2 Brillouin electron gun

The general equation of motion of an electron in an magnetic field can be described as [Humphries 2013, p. 459]

$$m_e \frac{d^2r}{dt^2} = \frac{e^2 n_0 r}{2 \epsilon_0} + \frac{m_e}{2} \left( \frac{e r B}{2 m_e} \right)^2 - \frac{(eB)^2 r}{2 m_e} \quad (2.3.2)$$

The radial position of the electron is here  $r$ . The terms on the right hand side are space charge force, centrifugal force and Lorentz force. In order to avoid the beam

oscillation, the sum of these forces must equal zero, i.e.

$$\frac{e^2 n_0}{2 m_e \epsilon_0} = \left( \frac{e B}{2 m_e} \right)^2. \quad (2.3.3)$$

This can be expressed using the magnetic gyro-frequency and plasma frequency as

$$\frac{\omega_p}{\omega_c} = \frac{1}{\sqrt{2}} \quad (2.3.4)$$

Eq. 2.3.4 is the Brillouin condition. The technical realization of a Brillouin beam is done in two steps: The electron is generated and electrostatically compressed inside a region with  $B \approx 0$  mT and then injected into a matching magnetic field. At the injection point the electron beam has to be parallel to the local magnetic field lines in order to keep the transverse momentum and therefore the oscillations minimal. A typical example of a Brillouin beam is shown in Fig. 2.3.2.

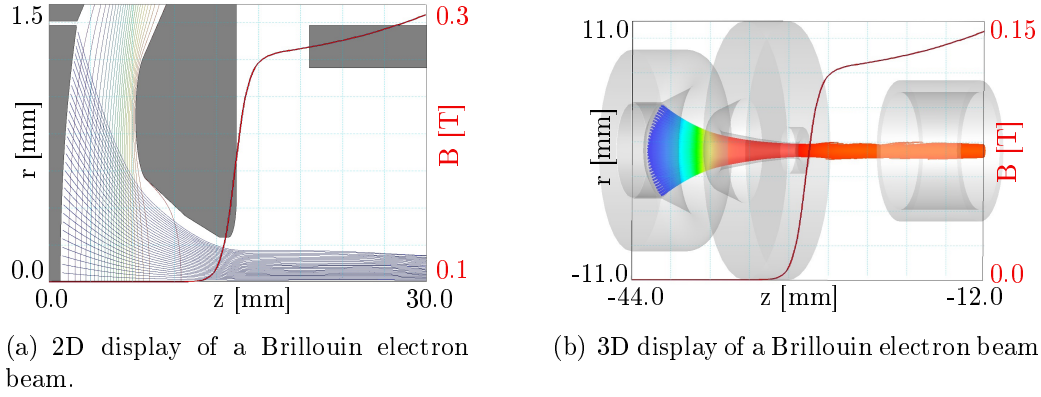


Figure 2.3.2: Simulation of an electron beam in TestEBIS, as an example from a Brillouin electron gun.

The electron beam is compressed electrostatically inside the gun region. When injected into the B-field, the compression is realized owing to the magnetic compression as the electron beam propagates towards a higher magnetic field.

An electron gun operating in the Brillouin regime generates an electron beam satisfying the relation[Brewer 1967, p. 98]:

$$I_e = 1.45 \cdot 10^6 B_0^2 \sqrt{E_e} r_e^2 \quad \longrightarrow \quad B_0 = \sqrt{\frac{\pi j_e}{145 \sqrt{E_e}}} \quad (2.3.5)$$

Eq. 2.3.5 defines the matching magnetic field,  $B_0$ , of a gun operating in the Brillouin regime.

## 2.4 Cathode physics

The emission current of the cathode crystal depends mainly on the applied electric field, cathode temperature, work function and the quality of the crystal surface. In this section the influence of these four parameters will be introduced.

### 2.4.1 Emission regimes

A typical characterization curve for a cathode is shown in Fig. 2.4.1. The curve can be separated into three regimes. The first is the so-called space-charge limited emission regime (SC-regime). In the SC-regime the electron beam emission is limited by the electron beam itself. The electrons already emitted compensate the applied electric field with their space-charge field. This leads to reduced emission of the cathode. The emitted current for a certain applied extraction potential,  $U_{\text{ex}}$ , depends on the gun geometry, which governs the electric field strength and distribution. This relation can be expressed with the Child-Langmuir law  $I_e = \text{perv} \cdot U_{\text{ex}}^{1.5}$ .

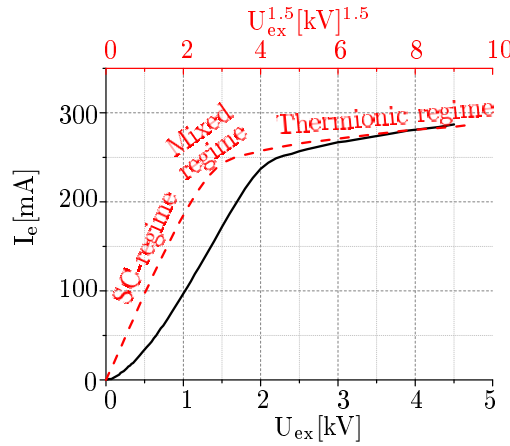


Figure 2.4.1: Characteristic emission curve of a cathode with a certain temperature. The black curve shows the  $I(U)$  dependency and the red curve shows the  $I(U^{1.5})$  plot for evaluating the perveance.

The parameter  $\text{perv}$  is called “perveance” in  $[\text{A}/\text{V}^{1.5}]$  and describes the maximum current an electron gun with a certain geometry can provide. For simple geometries the perveance can be calculated analytically. In order to evaluate the perveance of an electron gun, the current distribution has to be plotted versus  $U_{\text{ex}}^{1.5}$ , as shown in Fig. 2.4.1 with the red curve. The slope of the red graph at low extraction potentials equals the perveance of the gun. When the applied extraction potential is increased the space-charge field of the emitted electron beam is no longer sufficient to compensate the electric field as the cathode is emitting in the “thermionic regime”. In this regime the emission of a cathode is limited by the number of electrons having enough energy to surpass the energy gap between the Fermi level and the potential energy at the surface. The emitted current density in this regime can be calculated according to the Richardson-Dushman equation:

$$j_e = A_R^* T_c^2 \exp \left[ -\frac{\Phi - \Delta\Phi}{k_B T_c} \right] \quad \Delta\Phi = \sqrt{\frac{e^3 E}{4\pi \epsilon_0}} \quad (2.4.1)$$



In this equation  $A_R^*$  is the so-called Richardson-constant, which is a product of the theoretical value  $A_{R,0} = 120 \text{ Acm}^{-2}\text{K}^{-2}$  and an experimentally determined, material-dependent factor  $A$ .  $\Phi$  is the material-dependent work function, which is the amount of energy necessary for ejecting an electron from the conducting band into the vacuum.  $T_c$  is the cathode temperature,  $k_B$  is the Boltzmann constant and  $\Delta\Phi$  is the Schottky-correction considering the tunneling of electrons through the Schottky-barrier due to the electric field  $E$  applied perpendicular to the cathode surface. The third regime is the so-called “mixed regime”. Here the cathode emits partially in SC-regime and thermionic regime.

## 2.4.2 The work function

The work function (eV) is the minimum energy necessary to eject an electron from the solid into the vacuum. This value is dependent on the material, the purity of the surface and the temperature. For mono-crystal cathodes the surface orientation expressed by the Miller index contributes to the work function. The most commonly used, commercially available cathode materials are  $\text{LaB}_6$  ( $\Phi \approx 2.7 \text{ eV}$ ),  $\text{IrCe}$  ( $\Phi \approx 2.6 \text{ eV}$ ), transition metal carbides (for instance  $\text{TiC}$  with  $\Phi \approx 4.9 \text{ eV}$ ) or refractory metals (for instance  $\text{W}$  with  $\Phi \approx 4.3 \text{ eV}$ ).

Another influence on the work function are surface impurities, which are caused by ion implantation or thermochemical reactions [Avdienko and Malev 1977, Goldstein and D.J.Szostak 1978]. A source for implantation of ions is the ionization of background residual gas in the gun volume. In [Goldstein and D.J.Szostak 1978] various pressure dependent reaction rates of  $\text{LaB}_6$  with for instance  $\text{N}$ ,  $\text{H}_2\text{O}$  or  $\text{CO}_2$  are discussed. The general strategy for avoiding surface impurities is to ensure a low pressure in the cathode containing volume.

Besides the material dependence, the work function varies also for different Miller indexes [Gesley and Swanson 1984]. In case of  $\text{LaB}_6$  the work function can vary from  $\Phi = 2.42 \text{ eV}$  with a Miller index of  $\langle 310 \rangle$  up to  $\Phi = 2.92 \text{ eV}$  with a Miller index of  $\langle 211 \rangle$ .

The fourth effect is the temperature dependency of the work function, which is measured as a linear gradient  $[d\Phi/dT]$  in defined temperature ranges [Gesley and Swanson 1984, Kuznetsov 1994]. This work function gradient is positive within the temperature range of an operating EBIS/T, which leads to a non-linear increase of necessary cathode temperature in order to provide a higher emission current density according to Eq. 2.4.1. Higher temperatures lead to higher evaporation rates of the cathode material and therefore to a shorter cathode lifetime.

## 2.4.3 Cathode roughness

Cathode surfaces have a certain roughness by default due to the limits of the manufacturing processes. Electrons starting off from an uneven surface create local areas of higher and lower electron densities, which act as lenses. Deflected electrons gain an additional transverse momentum, which can decrease the maximal current density of the generated electron beam and can be treated as additional electron temperature. Kuznetsov pointed out that the additional possible temperature increase due to surface roughness is  $\approx 1 - 2 \text{ eV}$  for a  $\text{LaB}_6$  cathode with a temperature

of  $T_c = 1850^\circ\text{C}$  and a surface roughness of  $\Delta z_c = 10\text{ }\mu\text{m}$  [Kuznetsov 1997]. In order to estimate approximately the effect of the temperature gain one can compare the surface roughness with the distance between the cathode surface and the potential minimum in front of the cathode. The potential difference  $U - U_M$  between the cathode and potential minimum can be approximated with the equation [Suits and Way 1961, p. 379]:

$$U - U_M [\text{V}] = \frac{T_c}{5040} \log \left( \frac{j_{e,0}}{j_e} \right) \quad (2.4.2)$$

The maximum current density at a certain temperature  $T_c$ ,  $j_{e,0}$ , is given by the material, while  $j_e$  is the actual operational current density of the cathode operating at a temperature  $T_c$ . The potential difference gives the distance between the virtual cathode and the physical cathode surface as:

$$\Delta z [\text{cm}] = \sqrt{2.334 \cdot 10^{-6} \frac{(U - U_M)^{1.5}}{j_e} \left[ 1 + 0.0247 \sqrt{\frac{T_c}{U - U_M}} \right]} \quad (2.4.3)$$

The additional temperature is in the range of the potential difference  $(U - U_M)$ , if  $\Delta z$  is approximately equal to the manufacturing uncertainties. In order to keep the contribution from the surface imperfections small, one has to operate the source at a low ratio between extracted current density and maximum current density.

## 2.5 Electron beam dynamics in magnetic fields

### 2.5.1 Magnetic mirror effect

When operating an electron gun it is of interest if the electrons are accepted by the EBIS/T solenoid. For charged particles propagating in magnetic fields the magnetic momentum  $\mu = mv_\perp^2/2B$  is invariant [Bittencourt 2013, p. 44f]. For any non-zero value there exists a maximum magnetic field at which the particle can not enter. This effect is used in magnetic bottles. By evaluating the acceptance angle between the magnetic field lines and the incident angle of the charged particle one can estimate the maximal magnetic field where a particle will be reflected.

By comparing the Hamiltonian

$$H = \frac{p^2}{2m} + V = \frac{1}{2m} [p_r^2 + p_z^2 + p_\theta^2] + qU_{sc} + qU_{dt} \quad (2.5.1)$$

of particles in a plane in the low magnetic field and inside the high magnetic field one can derive the full acceptance angle and its two special cases.

The step-by-step derivation is executed in the appendix. The explicit acceptance angle for an electron ( $q=e$ ) is:

$$\alpha = \arcsin \left[ \frac{1}{v_{\text{tot},1}} \sqrt{v_{\theta,2}^2 - v_{z,1}^2 + \frac{2e}{m} (\Delta U_{\text{sc}} + \Delta U_{\text{dt}})} \right] \quad (2.5.2)$$

The acceptance angle for an electron beam without the space charge effects is:

$$\alpha = \arcsin \sqrt{\frac{B_1}{B_2}} \quad (2.5.3)$$

This is the magnetic mirror condition for free electrons [Geller 1996]. Consider an electron beam with a transverse kinetic energy of  $E_{\text{kin},\perp,1} = 345 \text{ eV}$ , an axial velocity of  $v_{z,1} = 5.24 \cdot 10^7 \text{ m/s}$  and a total velocity of  $v_{\text{tot},1} = 5.66 \cdot 10^7 \text{ m/s}$  at a position in front of the solenoid, where a magnetic field of  $B_1 = 0.16 \text{ T}$  is applied. Inside the main solenoid, where  $B_2 = 4.91 \text{ T}$ , the outer particles of the beam have the azimuthal velocity  $v_{\theta,2}^2 = 5.56 \cdot 10^7 \text{ m/s}$ . The space charge difference due to beam compression is  $\Delta U_{\text{sc}} = 1.35 \text{ kV}$ . Further assume that the ion trap is open, i.e.  $\Delta U_{\text{dt}} = 0 \text{ V}$ . The general acceptance angle according to Eq. 2.5.2 is  $\alpha = 0.21 \text{ rad}$ . Eq. 2.5.3 results in an acceptance angle of  $\alpha = 0.18 \text{ rad}$  for a free electron.

## 2.5.2 The Bursian limit

The space-charge field of an electron beam with a specific current propagating through drift tubes decreases the potential inside the beam. If the propagating beam current is increased, the potential will be decreased further due to the space-charge field. At a certain current, the potential is zero and a virtual cathode, which reflects electrons, is formed. The current at which the reflecting virtual cathode is formed can be calculated according to [Nezlin 1993, p.13]:

$$I_B [\text{A}] = 25.4 \cdot 10^{-6} \frac{(E_e [\text{V}])^{3/2}}{1 + 2 \ln(r_{\text{dt}}/r_e)} \quad (2.5.4)$$

This equation is valid for the condition  $2 \ln(r_{\text{dt}}/r_e) \gg 1$ , which indicates that the drift tube radius is much larger than the electron beam radius. A higher current leads to the formation of a reflecting virtual cathode, which is due to the buildup of a space charge barrier.

## 2.5.3 Electron beam radius

The electron beam radius of a Brillouin electron beam, the Brillouin radius, can be described with:

$$r_B = \frac{0.15 \sqrt{I_e}}{B E_e^{0.25}} (\text{mm}). \quad (2.5.5)$$

This Brillouin radius is the minimum radius of an electron beam emitted in the space-charge limited regime into a magnetic field. For an electron beam originating from a heated cathode exposed to a non-zero magnetic field, G. Herrmann introduced an extension of the formula for the Brillouin radius [Herrmann 1958].

$$r_H = r_B \left( 0.5 + 0.5 \left[ 1 + 4 \left( \frac{8 m_e k_B T_c r_c^2}{e m_e^2 B^2 r_b^4} + \frac{B_c^2 r_c^4}{B^2 r_b^4} \right) \right]^{0.5} \right)^{0.5} \quad (2.5.6)$$

In both equations  $B$  is the magnetic field strength in [T].  $k_B T_c$  is the cathode temperature in eV,  $m_e$  is the electron mass,  $r_c$  is the cathode radius,  $B_c$  is the B-field at the cathode and  $E_e$  is in keV. In general the Herrmann radius is defined as the radius containing 80 % of the total beam current. For a 1 A electron beam with a kinetic energy of  $E_e = 10$  keV, emitted from a cathode of a radius of  $r_c = 6$  mm at a temperature of  $k_B T_c = 0.11$  eV and  $B_c = 0.05$  mT, the Brillouin and Herrmann radius is  $r_B = 17 \mu\text{m}$  and  $r_H = 54 \mu\text{m}$  at a B-field of  $B = 4.91$  T.

#### 2.5.4 Two stream plasma instability

As introduced in [Cap 2012] and discussed in detail in [Shornikov et al. 2016] the Two Stream plasma Instability (TSI) occurs when two charge distributions propagate with different velocities relative to each other. In a charge breeder with finite trap length this instability may occur when Brillouin-gun generated electrons propagate relative to stationary ions. TSI may cause extraordinary ion heating and therefore increases the emittance of the ejected ion bunch [Litwin et al. 1982]. The criterion for stability is:

$$j_e > \frac{1.96 I_e^2}{10^{-4} \pi r_c^2 \sqrt{E_e}} \quad L < \sqrt{106 \frac{E_e^{1.5}}{[f \phi \frac{q}{A}]^{2/3} j_e}} \quad (2.5.7)$$

Here,  $f$  is the space charge neutralization factor,  $\phi$  is the overlap factor the electron and ion beam and  $A$  is the ion mass number. The left criterion indicates the minimal current density in the trapping region for a finite trap length. The right criterion indicates the maximal trap length for a certain electron and ion beam in the trapping region. Both criteria have to be fulfilled to avoid TSI.

#### 2.5.5 Electron beam quality

To establish a quality parameter for electron beams, a limited number of parameters are available. For numerical simulations where the electron temperature is not considered and where the electrons are emitted perpendicularly to the emission surface, the parameters "laminarity" or the radius variation of beam envelope are suitable [Pikin et al. 2013]. Laminarity is the degree of parallelism of the particle trajectories within the calculated beam. Crossing trajectories indicate beam aberration and distortions. This parameter can be investigated visually from the tracing plots of the beam propagation calculations. The laminarity will not be conserved when propagating the electron into high magnetic fields [Bobin et al. 1993] and is therefore only

suitable for evaluating the Brillouin beam near the gun volume. The radius variation of the beam envelope compares the radius of the first beam minimum and maximum at similar magnetic fields as  $\Delta r_e = r_{e,\max} - r_{e,\min}$ . For an electron beam propagating under Brillouin conditions  $\Delta r_e = 0$ , compare to Eq. 2.3.3. When considering electron temperature in the simulations other quality parameters have to be introduced, because the laminarity parameter is not valid at electron trajectories with an initial random transverse momentum. Due to the smoothing effect of the beam radius from the thermal electrons, the parameter  $\Delta r_e$  is also unavailable and has to be substituted by the radial current-density variation  $\Delta j_e(r)$ . The calculation of the emittance is here another possibility for evaluating the beam quality. The emittance in a radially symmetric geometry can be calculated as [Lee and R.K.Cooper 1976]:

$$\epsilon_r = 2.0 \sqrt{\overline{r^2} \left[ \overline{(p_r/p_z)^2} + \overline{(p_\theta/p_z)^2} \right] - \left( \overline{rp_r/p_z} \right)^2 - \left( \overline{rp_\theta/p_z} \right)^2} \quad (2.5.8)$$

The weighted emittance is:

$$\overline{\epsilon}_r [\text{mm mrad}] = \gamma \beta \epsilon_r \quad \text{with} \quad \gamma = \frac{1}{\sqrt{1 - \beta^2}} \quad \text{and} \quad \beta = v_{\text{tot}}/c \quad (2.5.9)$$

Here,  $c$  is the speed of light.

### 3 Automatized calculation of ionization potentials

Experimentally measured values of sub-shell dependent ionization potentials are not available for most medium-charged heavier elements. While high and low charged ions are well investigated and described, the intermediate charge states are not yet covered. When evaluating charge breeding efficiencies of heavier elements in an EBIS/T, approximations are the only sources for ionization potential input parameters to approximate cross sections. The established method is described by Carlson [Carlson et al. 1970]:

$$\begin{aligned} \epsilon_{(nlj)}^*(N) = \epsilon_{(nlj)}^*(N) + \sum_{nlj} \frac{q_{nlj}(N)}{\bar{r}_{nlj}} & \quad \left[ \text{if } \bar{r}_{nlj} \geq \bar{r}_{nlj}^* \right] \\ + \sum_{nlj} \frac{q_{nlj}(N)}{\bar{r}_{nlj}^*} & \quad \left[ \text{if } \bar{r}_{nlj} < \bar{r}_{nlj}^* \right] \end{aligned} \quad (3.0.1)$$

The ionization potential  $\epsilon_{(nlj)}^*(N)$  of an observed certain sub-shell is defined by a sum over all contributing electrons  $q$  in the corresponding sub-shells  $nlj$ , the Bohr-radius of the corresponding sub-shell  $\bar{r}_{nlj}$  of neutral atoms respectively its intermediate charge states  $\bar{r}_{nlj}^*$  and  $\epsilon_{(nlj)}(N)$  being the ionization potential for removing a particular electron from the sub-shell.

In order to generate more accurate ionization potentials for elements from hydrogen up to meitnerium the FA (Flexible Atomic)-code [Gu 2003] was used. The FA-code is a [Python]-accessible environment for performing relativistic corrected distorted-wave approximation calculations. Due to the extended amount of sub-shell dependent ionization potentials an assignation-bot ("Alice") was developed in order to perform automatized potential calculation on single elements. The electron configurations before and after the ionization process need to be given as input parameters. The bot takes the electron configuration of a neutral element as an initial starting configuration for the super-cycle. It then iterates the possible charge states of an atom with the super-cycle. Within a super-cycle a loop iterates the ionization process from the available sub-shells. Within one super-cycle all sub-shell dependent ionization potentials are calculated and the lowest total energy of each final electron configuration is evaluated. The bot chooses the electron configuration with the lowest energy level as the initial electron configuration for the next super-cycle. Every iteration of a cycle generates a solution file in which the lowest electron states with their quantum numbers and energy difference to the ground state is saved.

---

Algorithm 1 The pseudo code for carbon of the FAC-calculation bot “Alice”

---

```

1: function Input( $e_{\text{init}}$ )                                 $\triangleright e_{\text{init}}$  = initial electron configuration
2: end function
3:  $e_{\text{init}, C^q=0} = [2, 2, 2, 0, \dots, 0]$ 
4: for  $i = 0$  do to  $\sum e$                                  $\triangleright$  number of charge states
5:   for  $j = 0$  do to  $\sum n$                                  $\triangleright$  number of sub-shells
6:      $\text{str}(e_{\text{final}, C^q=i+1, j})$ 
7:     function Input to FAC( $e_{\text{init}}, e_{\text{final}}$ )
8:     end function
9:     save lowest energy levels of  $e_{\text{final}}$  and  $e_{\text{init}}$  in txt-file
10:   end for
11:    $\text{str}(e_{\text{init}, C^q=i+1}) = \text{str}(e_{\text{final}, C^q=i, j(E_{\text{min}})})$ 
12: end for

```

---

An example of a solution file of a cycle iteration is shown in Table 3.0.1. The first column lists the order of energy levels, the third is the energy difference of a quantum state relative to the ground energy level in [eV], the fourth column indicates the parity, the fifth column indicates the quantum numbers by  $100 \cdot n + l$  with  $n$  as the principle quantum number and  $l$  as the orbital angular momentum. In the sixth column the first number indicates the total angular momentum  $2J$  followed by the occupation numbers of open electron sub-shells in case of coupling of all electrons in the open sub-shells, the seventh column is the chemical writing and the eight column indicates the configuration of coupling. For instance,  $2p+3(3)3 \quad 3s+1(1)4$ “ indicates the coupling “ $[2p_{3/2}^3(J = 3/2) \quad 3s_{1/2}^1(J = 1/2)](J = 2)$ ”.

Table 3.0.1: An example of a solution file: The lowest energy levels of neutral C and  $C^{1+}$  before and after the ionization process removing an electron from the 2p-subshell. Energy level 5 is here considered as ionization potential.

| ILEV | IBASE | ENERGY    | P | VNL | 2J        |     |                   |
|------|-------|-----------|---|-----|-----------|-----|-------------------|
| 0    | -1    | 0.00E+00  | 0 | 201 | 0 1*2 2*4 | 2p2 | 2p-2(0)0          |
| 1    | -1    | 9.16E-02  | 0 | 201 | 4 1*2 2*4 | 2p2 | 2p+2(4)4          |
| 2    | -1    | 1.27E-01  | 0 | 201 | 2 1*2 2*4 | 2p2 | 2p-1(1)1 2p+1(3)2 |
| 3    | -1    | 2.01E+00  | 0 | 201 | 4 1*2 2*4 | 2p2 | 2p-1(1)1 2p+1(3)4 |
| 4    | -1    | 4.80E+00  | 0 | 201 | 0 1*2 2*4 | 2p2 | 2p+2(0)0          |
| 5    | -1    | 1.083E+01 | 1 | 201 | 1 1*2 2*3 | 2p1 | 2p-1(1)1          |
| 6    | -1    | 1.084E+01 | 1 | 201 | 3 1*2 2*3 | 2p1 | 2p+1(3)3          |

$\left. \begin{array}{l} \text{2p-2(0)0} \\ \text{2p+2(4)4} \\ \text{2p-1(1)1 2p+1(3)2} \\ \text{2p-1(1)1 2p+1(3)4} \\ \text{2p+2(0)0} \end{array} \right\} C^{0+}$   
 $\left. \begin{array}{l} \text{2p-1(1)1} \\ \text{2p+1(3)3} \end{array} \right\} C^{1+}$

After an element is calculated iteratively,  $n = \sum_{q, \sum_{\text{sub}}} \text{solution files}$  with the lowest energy levels before and after an ionization process are available. For instance, there are 877 files containing 34.6 Mbyte of ASCII data for uranium. A second bot ("Bob") acquires the generated library of solutions and searches for matching energy levels according to the final electron configuration. Since the final ionization potential should also consider spin-orbit coupling, the output data has to be separated according to the “-” and “+” orbitals. Bob takes the lowest energy configuration

matching the sub-shell applied coupling rule. The acquired energy and electron occupation value is saved into a triangle matrix into the entry [charge state i, sub-shell j]. Those two triangle matrices containing all sub-shell dependent ionization energies and the charge state dependent electron configurations of the calculated element are saved into a txt-file.

---

Algorithm 2 The pseudo code of the FAC-assembly bot “Bob”

---

```

1: function Input( $e_{\text{init}}$ )                                 $\triangleright e_{\text{init}}$  = initial electron configuration
2: end function
3:  $e_{\text{init}, C^q=0} = [2, 2, 2, 0, \dots, 0]$ 
4: for  $i = 0$  do to  $\sum e$                                  $\triangleright$  number of charge states
5:   for  $j = 0$  do to  $\sum n$                                  $\triangleright$  number of sub-shells
6:     - load solution file
7:     - enable sub-shell dependent selection rule
8:     - search for the energy level of matching quantum number
9:     - save the energy level in matrix into entry i,j
10:   end for
11: end for
12: saving matrix in a data-file

```

---

As an example, the solution for carbon is shown in the following two matrices. The left matrix shows the sub-shell dependent ionization potential, the right matrix shows the corresponding electron population at the lowest energy level of the corresponding charge state.

$$\begin{pmatrix}
 q & 1s & 2s & 2p \\
 0 & 2.954E+02 & 1.456E+01 & 1.084E+01 \\
 1 & 3.146E+02 & 2.869E+01 & 2.384E+01 \\
 2 & 3.391E+02 & 4.569E+01 & 0 \\
 3 & 3.621E+02 & 6.418E+01 & 0 \\
 4 & 3.908E+02 & 0 & 0 \\
 5 & 4.900E+02 & 0 & 0
 \end{pmatrix}
 \begin{pmatrix}
 q & 1s & 2s & 2p \\
 0 & 2 & 2 & 2 \\
 1 & 2 & 2 & 1 \\
 2 & 2 & 2 & 0 \\
 3 & 2 & 1 & 0 \\
 4 & 2 & 0 & 0 \\
 5 & 1 & 0 & 0
 \end{pmatrix}$$

The generated library of charge state dependent binding energies and electron configurations include all elements from hydrogen up to meitnerium in the recent state. This equals more than 48.000 files (1.23 Gbyte ASCII-data) of energy level solutions, which makes it necessary to use the Bob-algorithm for evaluation and matrix generation. As an example the ionization of three elements are shown in Fig. 3.0.1 and Table 3.0.2. The solution of the Carlson-approximation  $I_q(X)$  and the corresponding entries of the generated matrices of the Alice/Bob-algorithms are compared with measured data provided by [NIST]. Comparing the tabled values shows that the FAC-generated values are closer to the measured values than the solutions of the Carlson-approach. The advantage is significant especially at highly charged and heavy ions, where the Carlson-approach fails.

Fig. 3.0.1 shows the relative derivation of the Carlson and FAC values from the NIST-values. Both approaches underestimate the ionization potentials of neutral atoms and low charged ions. As was shown with carbon and aluminum, the fewer electrons remaining, the better are the results of the FAC compared to the Carlson approximation. As opposed to the Carlson approach, FAC calculates the sub-shell



Table 3.0.2: Measured ionization potentials  $I_q(A)[\text{eV}]$  and calculated ionization potentials  $I_q(X)[\text{eV}]$  according to Carlson and the FAC generated potentials  $I_q[\text{eV}]$  for carbon, aluminum and bismuth.

| q  | Carbon (Z = 6) |          |       | Aluminum (Z=13) |          |       | Bismuth (Z=83) |          |       |
|----|----------------|----------|-------|-----------------|----------|-------|----------------|----------|-------|
|    | $I_q(A)$       | $I_q(X)$ | $I_q$ | $I_q(A)$        | $I_q(X)$ | $I_q$ | $I_q(A)$       | $I_q(X)$ | $I_q$ |
| 0  | 11.3           | 10.6     | 10.8  | 6.0             | 5.7      | 5.4   | 7.3            | 6.8      | 6.8   |
| 1  | 24.4           | 26.1     | 23.8  | 18.8            | 18.7     | 17.6  | 16.7           | 17.2     | 16.4  |
| 2  | 47.9           | 50.4     | 45.7  | 28.4            | 29.2     | 28.2  | 25.6           | 26.9     | 25.4  |
| 3  | 64.5           | 67.6     | 64.2  | 120             | 116      | 118   | 45.4           | 46.1     | 43.1  |
| 4  | 392            | 374      | 390.8 | 154             | 162      | 152   | 54.9           | 48.2     | 54.8  |
| 5  | 490            | 476      | 490   | 190             | 207      | 189   | 88.4           | 85.8     | 85.8  |
| 6  |                |          |       | 242             | 252      | 242   |                |          |       |
| 7  |                |          |       | 285             | 298      | 285   |                |          |       |
| 8  |                |          |       | 330             | 343      | 330   |                |          |       |
| 9  |                |          |       | 399             | 427      | 394   |                |          |       |
| 10 |                |          |       | 442             | 471      | 441   |                |          |       |
| 11 |                |          |       | 2086            | 1984     | 2085  |                |          |       |
| 12 |                |          |       | 2304            | 2211     | 2304  |                |          |       |

dependent ionization potentials, which allows improved charge breeding estimations. According to Eq. 2.2.1, the potentials of all sub-shells are required for calculating the total cross section. Therefore the Carlson approach underestimates the cross section at low charged ions significantly. Another limitation is the insufficient number of measured sub-shell dependent ionization potentials of heavier ions. The generated ion potential map can provide for the first time potential values to cover all sub-shell dependent ionization potentials for all elements, which allows the breeding time to be estimated more precisely. The calculated solutions assembled in matrix files or by raw data can be obtained at [Onlinelib].

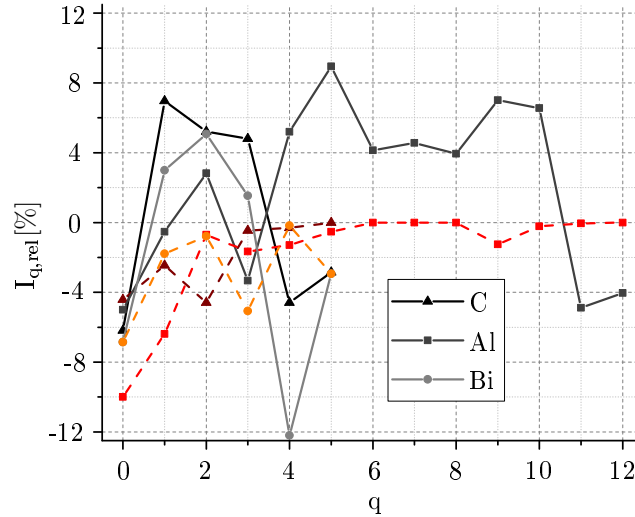


Figure 3.0.1: Carlson and FAC values from Table 3.0.2 in comparison to NIST values. The solid lines are the values generated with the Carlson approach, while the dashed lines are solutions from the FA-code. The ionization potentials of carbon are represented by triangles, the aluminum by squares and the bismuth-values by circles. A value of 0 % is a solution which agrees with the measured value.

## 4 Computational physics

This chapter covers the basic techniques for simulations discussed in this thesis. Simulations of an electron beam under special conditions allow a deeper understanding of measured cathode performance or the occurrence of loss current. For calculating electromagnetic fields and beam tracing one can take advantage of the radial symmetry of the EBIS/T setup. There the electron beam is calculated in a cylindrical coordinate system with the coordinates  $\theta, r, z$  as the azimuthal, radial and axial dimensions. This numerical approach is considered to be a 2D beam-tracing, because only the radial and axial dimensions of the EBIS/T geometry can be treated. As opposed to 3D calculations, which are performed in the Cartesian system, 2D calculations are faster and create less data. For 2D calculations the program suite by [Field Precision b] (FP) is used. While FP processes magnetic and electric fields in radial and axial coordinates, the tracing is internally done in the Cartesian system. Owing to ASCII input and output, this program allows the investigation of advanced electron beam problems like the tracing of first- and second-generation electrons in a collector. 3D simulation programs are obligatory when treating radial misalignments of electrodes or electromagnetic fields. For those tasks the program »PARTICLE STUDIO « from [CST] is used.

### 4.1 General numerical recipes

#### 4.1.1 Meshing

For electron beam calculations, meshing of the model is the translation from true geometry into a numerical model. It is a crucial step where the user must compromise between geometric accuracy and data-size. In case the meshing volume contains emitting surfaces it is very important to ensure equal meshing along the surface in order to minimize numerical errors and ensure the correct simulation of the emission process of a cathode. During the meshing process the user has to ensure that the mesh precision between fine-meshed regions of interest and coarse-meshed regions transits with a numerical sufficient gradient. The general aspect ratio between the coarsest and finest regions should be generally low. Second, the radial meshing precision must be sufficient to resolve the space-charge field of calculated particles. An approximate rule suggests more than 10 field points per beam radius. The axial meshing should resolve more than one time step per mesh cell. When meshing geometries used to calculate the magnetic field, the user must provide a sufficient amount of the surrounding volume to avoid field errors caused by the boundary conditions. A visual user control is highly recommended after processing the mesh, because the meshing solution can be numerically correct while leaving the input

geometry warped. An example about different meshing ratios and resulting errors due to inappropriate meshing is shown in Fig. 4.1.1. If improperly assigned mesh-cells or nodes are not corrected they might introduce point sources of electric fields and distort charged particle tracings.

#### 4.1.2 Time steps

The second basic mechanism for setting up calculations is the adjustment of the time steps. In calculations considering B-fields the number of time steps resolving one Larmor revolution determines the accuracy of energy conservation in simulations. According to FP, more than 50 time steps, i.e.  $t < 1/(50\omega_c)$ , are required to suppress the energy conservation error to less than  $\Delta E/E = 1 \times 10^{-3}$ , see Table 4.2.2.

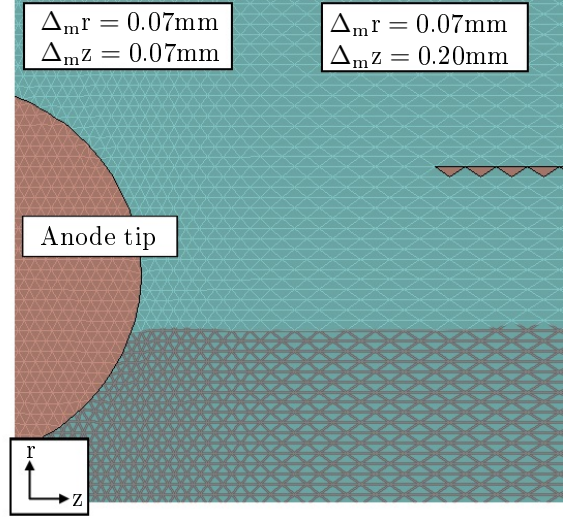


Figure 4.1.1: Example of possible meshing errors of the anode electrode of the HEC<sup>2</sup> gun. Here the meshing is partly colored for better visibility. The meshing ratio varies in the axial direction. Sources of errors include improperly assigned mesh cells and poorly resolved surfaces, which can result in saw-toothed edges.

#### 4.1.3 The residual value

In general beam tracing is performed iteratively, where each iteration contains two steps. The first step is to trace the electron beam according to the electrostatic field solution within the volume. The second step evaluates the electric field generated by the space-charge distribution. This space-charge solution will be super-positioned on to the initial electrostatic field solution. The method for calculating the space-charge field in TRAK, the particle-tracing module of FP, is the so-called successive over-relaxation method [Hageman and Young 2004], which requires two input parameters:  $\omega$  and the AVG-value. The adjustment of these two parameters has a major impact on the calculation time and the quality of the result. The space-charge distribution can be calculated by:

$$Q_i^{(k+1)} = (1 - \text{AVG})Q_i^k + \text{AVG} \cdot Q_i^{(k+1, \text{beam})} \quad (4.1.1)$$

where  $Q_i^{(k+1, \text{beam})}$  is the space-charge density distribution of the traced electron beam in the current iteration, while  $Q_i^{(k)}$  represents the general space-charge density distribution of the last iteration in the calculation volume. A smaller AVG-value leads to slower but more stable convergence towards the solution. Choosing a too high value can lead to a two-stating solution which does not converge. The solution  $\phi_i^n$  on the iteration  $n$  is calculated using the previous iteration  $\phi_i^{n-1}$  and the residual value  $r_i^n$  multiplied by the correction factor  $\omega$

$$\Delta_{ij}\phi_j = Q_i \quad \rightarrow \quad \phi_i^n = \phi_i^{n-1} + \frac{\omega}{\Delta_{ii}} r_i^n \quad (4.1.2)$$

where  $\omega$  is here the over-relaxation parameter, which has a value of  $0 < \omega < 2$ . The adjustment of  $\omega$  follows similar rules as the AVG-value. In converging simulations the residual value reduces at each iteration until it passes a certain value. The residual value defines the end condition of the iterative calculation method. As additional information the number of iterations for recalculating the space-charge field, named "Icycles", indicates the quality of convergence. A number of Icycles not converging towards zero indicates a solution alternating at a residual value lower than the set value, but not converging.

In general  $\omega$  should be chosen close to 2, AVG has to be small and the residual value smaller than  $1 \cdot 10^{-8}$ . Eq. 4.1.1 and 4.1.2 indicate that the calculation matrix increases non-linearly with the volume size to which the number of time steps are related. Therefore more elements have to be considered during the iterative calculations, which reduces the likelihood of a convergence at lower residual values. In addition, to the total number of time steps within the calculation volume, the volume size itself reduces the likelihood of finding a solution. Volume not effected by the space-charge field of the electron beam, the background, will be considered in the iterative recalculation of the space-charge field. An extended recalculation time is another effect, which can be suppressed by reducing the volume of no interest, for instance the volume outside of a drift tube.

#### 4.1.4 Convergence

The likelihood of convergence depends mainly on the size of the matrix of Eq. 4.1.1 and 4.1.2. Examples of converging and non-converging solutions are shown in Fig. 4.1.2. Both calculations have the same input parameters:  $\omega = 1.9$ ,  $\text{AVG} = 0.1$  for the first 10 iterations and  $\text{AVG} = 0.05$  for the next, the residual value was set to  $2 \cdot 10^{-8}$ . A cathode temperature of  $T_c \approx 4600$  K, which caused additional transverse momentum on the particles, was applied in the non-converging solution.

In both cases the residual values were reached during the calculations, which fulfills the first requirement of convergence. When the residual value is reached the beam trajectories vary on a smaller scale and fewer Icycles are required for recalculating the space-charge field. The Icycles of "geo 1" in Fig. 4.1.2 stalled at 40 iterations, which indicates that the solution of the beam trajectories alternates around a solution. The number of Icycles do not converge to zero, because for every small variation the space-charge field has to be re-calculated. In contrast, "geo 2" converges. The numbers of Icycles converge to zero, which fulfills the second requirement for a converged solution. Fulfilling both requirements results in a high conservation of energy and precise tracing of the trajectories.

#### 4.1.5 Cluster calculation

3D beam tracing sets higher demand for computing power. Therefore a specialized cluster was set up. The model has to be configured on the local computer and uploaded to the processing server. A local communicator assigns the model to a free cluster node where the job is queued. Currently there are 13 nodes, each equipped with 32 "Intel Xeon Processor E5-4650", available at the cluster. Eight light nodes with 128GByte RAM and five heavy nodes with 512GByte RAM provide

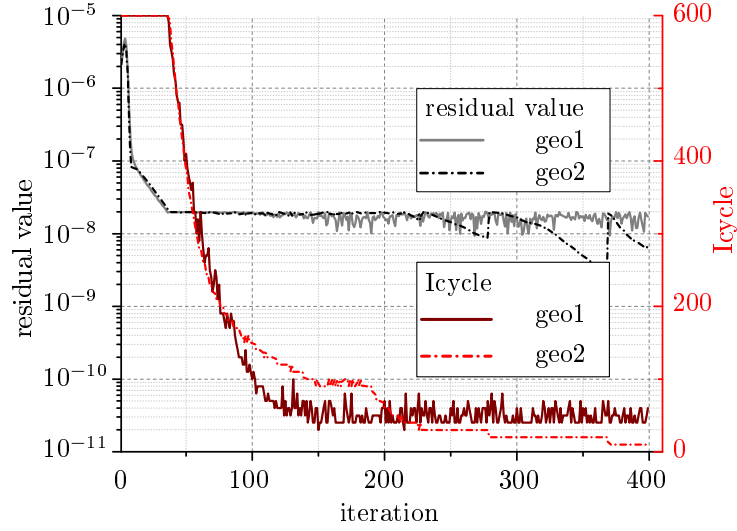


Figure 4.1.2: Converging development of a badly setup geometry (geo 1) shown in solid lines and of a well setup geometry (geo 2) in dashed lines. The upper distributions are the residual value at a certain iteration step and the lower distributions show the number of cycles for recalculating the space-charge field.

sufficient calculation power to calculate 3D models with an adequate spatial sub-millimeter resolution. Because both, cluster and CST, are in constant development, every submitted model has to pass the refinement process. First a simplified model with very coarse meshing has to be submitted in order to verify its functionality. This allows for benchmarking of the model and avoids occupying multiple nodes with a simulation which will eventually fail at an advanced stage. Once it passed the coarse level, a model with finer mesh and lower residual value is sent to the cluster. This procedure has to be repeated until a meshing level is reached where precision and calculation time are optimized. 3D simulations are used in this thesis for investigating beam tracing with radially misaligned electrodes or to investigate electric or magnetic fields when introducing non-radial geometries. An example is the verification of the measured emission properties of the electron gun installed at TwinEBIS, discussed in chapter 5.

## 4.2 Optimization of the simulation via volume division

Tracing charged-particle beams in volumes with a high length-to-radius ratio, for instance an electron beam from the cathode to the collector, is very challenging for a numerical code. The electron beam has to be traced from cathode to collector in a volume with a length of approximately 3 m in the TestEBIS geometry while the electron beam is compressed from  $r_e = 10$  mm at the cathode to  $200 \mu\text{m}$  inside the main solenoid ( $B = 5$  T). Fine meshing near the cathode surface is required in order to correctly resolve the electron emission and electrostatic focusing inside the electron gun. The simulation has to find correct solutions in areas of a magnetic field gradient, where the electron beam compression and electron gyration varies. In addition the Larmor motion has to be resolved, which requires fine radial meshing

on a scale of the radius of the compressed beam. Finally the electron beam has to be traced inside the collector volume where the beam expands and slows down.

Three general approaches exist for investigating electron beam distributions far from the cathode, for instance inside the collector. The first is to assume and generate a self-made electron beam distribution in front of the collector and trace it. The second approach is to simulate the electron beam in the electron gun and translate the beam to a position in front of the investigated area with similar electric and magnetic fields. The third approach is to simulate the electron beam from the cathode to the investigated device.

Most programs fail to achieve a solution in such an extended volume considering all the previously mentioned requirements.

In order to calculate charged-particle beams over this long distance an adapted technique was developed, named "stage-approach". The general volume was divided into locally optimized and overlapping sub-volumes. The electron beam is then serially traced through these sub-volumes until it reaches the area of interest. This section will discuss the stage-approach used for TestEBIS and REXEBIS.

#### 4.2.1 The technique

Volume division consist in dividing the total simulation volume into smaller overlapping sub-volumes. Optimized parameters like meshing and convergence parameters are adjusted to local requirements for each sub-volume. The particle properties will be handed over to the next volume until the desired tracing position is reached. Generally, the user follows this guideline:

1. Split the major volume into a reasonable number of overlapping sub-volumes. For instance, within one sub-volume the beam has to pass a maximal magnetic-field change of  $\Delta B < 400$  mT at a kinetic energy of 10 keV. Volume splitting in electric field gradients has to be avoided.
2. Optimize meshing and the spatial dimension of the sub-volumes.
3. Simulate the electron beam from the emitting cathode to the end of the first sub-volume.
4. Record trajectory properties at a position before the boundary: mass, charge, kinetic energy, position, the momentum vector and the carried current.
5. In the second sub-volume the starting point will correspond to the recording position in the first volume.
6. Repeat point 4 and 5 until the sub-volume of interest is reached.

For the first cathode containing volume it is important to mesh the radial area of the cathode with equal precision. The longitudinal meshing is adjusted according to the electron velocity, difficulties of mechanical geometries and desired precision of electric field. Examples of sub-volume meshing for TestEBIS and REXEBIS are listed in Tab. 4.2.1, which shows the recommended meshing according to the local particle velocities.

Table 4.2.1: Radial (dr) and longitudinal size (dz) of a sub-volume with the smallest and largest mesh size in radial ( $\Delta_{mr}$ ) and longitudinal direction ( $\Delta_{mz}$ ),  $r_L$  is the minimal radial mesh-size to resolve the Larmor motion with 50 time-steps per turn;  $dz(t)$  is the longitudinal travel-distance of the electron per time-step. All distances are in [mm].

|                  | dr  | $\Delta_{mr}$ | dz  | $\Delta_{mz}$ | $r_L$ | $dz(t)$ |
|------------------|-----|---------------|-----|---------------|-------|---------|
| TestEBIS-vol. I  | 45  | 0.07 -> 0.15  | 207 | 0.15 -> 0.25  | 0.38  | 0.354   |
| TestEBIS-vol. V  | 30  | 0.01 -> 1.0   | 520 | 0.1           | 0.02  | 0.006   |
| TestEBIS-vol. XI | 180 | 0.01 -> 0.3   | 500 | 0.1           | 0.79  | 0.006   |
| REXEBS-vol. I    | 15  | 0.01 -> 0.02  | 100 | 0.02->0.01    | 0.04  | 0.007   |
| REXEBS-vol. V    | 10  | 0.01 -> 0.7   | 320 | 0.01          | 0.02  | 0.006   |
| REXEBS-vol. VIII | 35  | 0.05 -> 0.4   | 250 | 0.1 -> 0.2    | >0.08 | <0.7    |

The choice of local radial mesh size depends on the radius of the Larmor motion and therefore on the B-field strength. It is recommended to choose a radial mesh size lower than the indicated  $r_L$  -value. The  $r_L$ -value is calculated by the time for one Larmor turn and the size of time steps. In TRAK the recommended numbers of steps for a desired numerical precision are indicated in [Field Precision a] and are listed in Table 4.2.2. For an energy conservation of less than  $\Delta E/E < 10^{-3}$  throughout the simulation with tolerable calculation time and file sizes, a radial mesh resolution resulting in more than 50 calculation steps per turn is chosen. The longitudinal mesh size is given by the kinetic energy of the particles and the adjusted time steps. The mesh-cell size must be larger than the axial distance traveled by a particle during one time step.

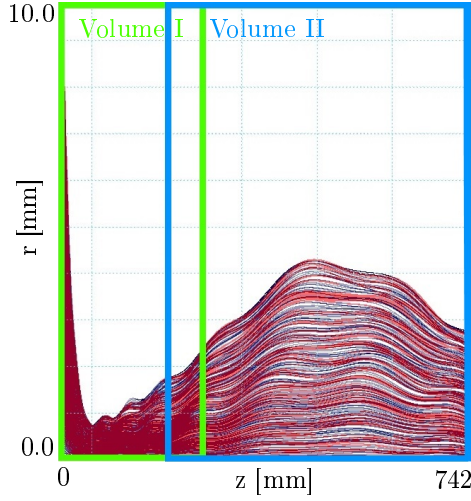
Missed mesh-cells increase the tracing error due to missing information between two time steps. The radial meshing should be chosen to resolve the electron beam radius by more than 10 mesh cells. If those recommendations are not fulfilled, the solution may not converge and the energy conservation would not be guaranteed. This leads to unreliable particle trajectories.

To illustrate the gain of the method, an extended volume with the same dimensions as volume I and II of the HEC<sup>2</sup> gun geometry was created and an electron beam simulated, shown in Fig. 4.2.1(a) as **red** trajectories. The sub-volumes are shown as colored frames and the associated electron beam is blue. While the calculation of the extended volume takes 20 hours to converge, the approach with sub-volumes needs approximately 3-5 hours. Volume I contains the emitting surface, the Wehnelt electrode and the anode. The generated electron beam thereafter propagates to the right boundary, see Fig. 4.2.1(b). Before reaching the boundary of the first sub-volume, the particle properties will be recorded. A recording plane closer to the right volume boundary would intercept a region where the space-charge field is distorted due to boundary conditions.

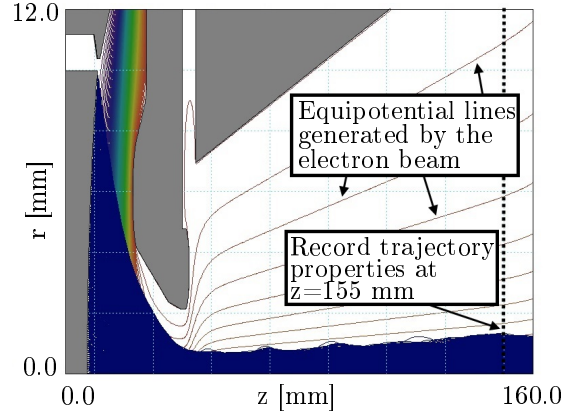
In Fig. 4.2.2(a) the handing over of the trajectories between the first two sub-volumes in the REXEBIS geometry is shown as an example of an electron beam

Table 4.2.2: Conservation of the kinetic energy depending on the number of calculation steps per turn

| Steps/turn | $\Delta E/E$          |
|------------|-----------------------|
| 10         | $8.984 \cdot 10^{-2}$ |
| 20         | $1.297 \cdot 10^{-2}$ |
| 50         | $8.560 \cdot 10^{-4}$ |
| 100        | $1.072 \cdot 10^{-4}$ |
| 200        | $1.340 \cdot 10^{-5}$ |
| 500        | $8.600 \cdot 10^{-7}$ |
| 1000       | $2.200 \cdot 10^{-8}$ |



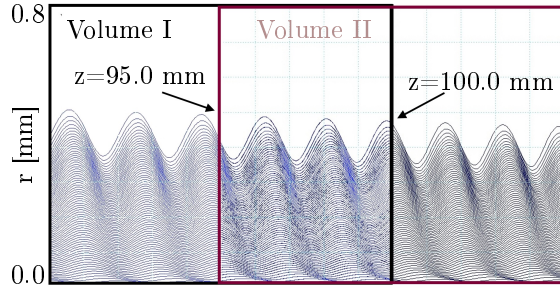
(a) Example of suitable volume slicing of an extended volume. Beam trajectories from simulation of two sub-volumes (blue) overlaid with trajectories from a single full volume simulation (red).



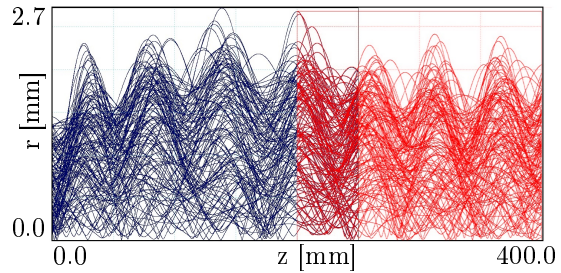
(b) Electron beam from the HEC<sup>2</sup> gun in the first volume as an example for an optimal position of the recording plane in a sub-volume.

Figure 4.2.1: Suggestion for dividing an extended volume into smaller sub-volumes. The recording plane of the first sub-volume defines the left boundary of the second overlapping sub-volume.

emitted from an immersed electron gun. Both volumes and trajectories are overlapping in a region where the electric field gradient can be neglected and the variation of beam radius is caused by the increasing B-field of the main solenoid. Both beams are propagating similarly so a visual separation of overlaid trajectories from two neighbored is not possible. Fig. 4.2.2(b) shows the handing over of a non-laminar electron beam.



(a) Zoom into the intermediate volume (Vol. I and Vol. II at REXEBIS). The resulting trajectories of both sub-volumes are overlaid.



(b) Hand-over of a distorted distribution at the TestEBIS geometry. Trajectories in sub-volume 9 are blue, while red in sub-volume 10.

Figure 4.2.2: Propagation of electron trajectories in the overlap area between two sub-volumes for a laminar and distorted electron beam.



## 4.2.2 Errors due to volume slicing

Slicing an extended volume on a certain axial position into smaller volumes and tracing charged particles in the sub-volumes generates errors at the hand-over points. First of all, dividing an extended volume with field gradients can lead to field-information loss in the sub-volumes. Secondly, the boundary conditions of each volume introduce an error for the starting condition at the left boundary of the following sub-volume.

### 4.2.2.1 Error due to field mismatching in the neighboring sub-volumes

Let us consider an extended volume with two drift tubes at different potentials creating an electric field in the center of the volume. In case the extended volume is divided between these two drift tubes both sub-volumes are lacking the second drift tube to calculate the electric field gradient. This is shown with an example from the REXEBIS geometry with two drift tubes at different potentials, see Fig. 4.2.3. The left drift tube has a potential of 1.2 kV and the right drift tube is at 0 V. The radius of the drift tubes  $r_{dt}$  is 5 mm. The voltage is read out at different axial positions inside the right drift tube in order to evaluate the extension of the field gradient. The correct slicing method is to include both drift tubes into a sub-volume to calculate an electric field gradient. Because the field gradient penetrates into both drift tubes, the slicing position determines the error of the kinetic energy due to the absence of the field gradient in the neighboring sub-volume. For instance, if the volume is sliced at a position where the particle properties are recorded inside the second drift tube at the axial position  $z = 1 \times r_{dt} = 5$  mm and start over in the second field gradient free sub-volume, the particle will have an artificial discrepancy in kinetic energy of 60 eV compared to a particle passing the full electric field gradient. If the recording plane is  $z = 4 \times r_{dt} = 20$  mm inside the second drift tube, the energy error is reduced to 50 meV. In this example, shifting the recording plane by an axial distance of one drift-tube radius deeper into the second drift tube reduces the energy discrepancy by a factor of 10.

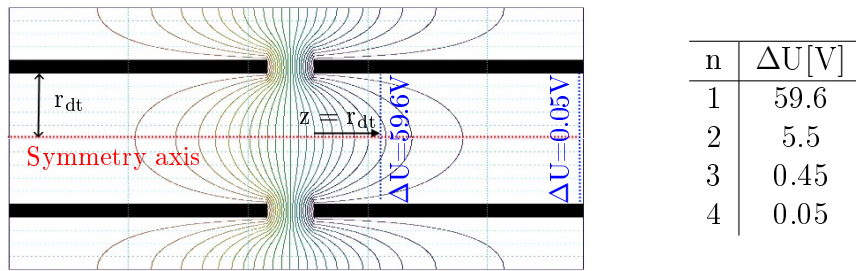


Figure 4.2.3: Resulting electric field between the drift tubes with applied potentials 1.2 kV and 0 kV.  $r_{dt}$  is the drift tube radius. The right table shows the electric potential at distances of  $n \times r_{dt}$  from the entrance of the right drift tube rightwards.

Hence, the slicing of the extended field gradient containing volumes has to be performed at a position where the recording plane is reasonably far away from the gradient to minimize to energy error. For example, when simulating the electron beam in the trapping region of an EBIS/T, the optimal sub-volume is chosen to contain the gap and the resulting electric field gradient in its center.

#### 4.2.2.2 Error due to boundary conditions

An error due to boundary conditions occurs when tracing the beam near the volume boundaries, where usually the Neumann boundary condition is applied. For a differential equation  $y$  defined in a domain  $\Omega \in \mathbb{R}^3$  with its boundary  $\partial\Omega$ :

$$\frac{\partial y}{\partial n} = \Delta y(x) \cdot n(x) = f(x) \quad \forall x \in \partial\Omega \quad (4.2.1)$$

with  $n(x)$  being the normal vector at the boundary. This condition allows electric potential lines reaching the boundary perpendicularly. In contrast, the Dirichlet boundary condition is used for electrodes:

$$y(a) = \alpha \quad \text{and} \quad y(b) = \beta \quad . \quad (4.2.2)$$

Under Dirichlet boundary conditions the potential lines follow the electrode surface, such as the potential lines at the drift tubes in Fig. 4.2.3. As previously discussed, the starting position of the electron beam in the following sub-volume is at the left volume boundary. According to the Neumann condition every component of the electric field vector, which is not parallel to the boundary, is suppressed at this position. When tracing the electron beam in a sub-volume, the particle-beam properties have to be recorded at a certain distance from the boundary in order to reduce the numerical error. In case of calculating magnetic field maps it is recommended to add sufficient space between the geometry and the boundaries. Because magnetic field lines are circulatory, this additional space ensures a non-distorted field distribution in the area of interest far from the boundaries.

### 4.3 Applications

This section covers advanced simulation techniques developed in order to accurately investigate measurements, which will be discussed in the following chapters.

First the emission area of a cathode is extended from the front surface to a connected surface of front and lateral surface. This translates to an extension from an emitting disc to an emitting cylinder.

Second an approach for investigating the electron beam properties in a regime between fully space-charge limited and fully thermionic is discussed. Also in this chapter a technique is presented, which allows to significantly increase the local particle number and the resulting phase space resolution. Most simulation programs globally adjust the particle number, which leads to a limited spatial resolution of the local particle propagation.

Finally, a supportive script is discussed, which allows to generate second-generation electron distributions from surfaces to which primary electrons are impacting.

#### 4.3.1 Side-emission from the electron cathode

Including the lateral surface of the cathode as an emission surface allows considering side-emitted electrons (SEE). In immersed electron guns SEE follow the magnetic

field lines and propagate in the outer rim of the front-emitted electron beam. SEE in Brillouin electron guns over-focus in the gun region and generate a beam halo containing trajectories with extraordinary high transverse momentum. A visual example of SEE from an immersed gun is shown in Fig. 4.3.1(a), where an electron beam emission in the REXEBIS geometry is simulated. Fig. 4.3.1(b) shows an electrostatically compressed Brillouin electron beam generated only from the front surface. Fig. 4.3.1(c) shows the same situation now considering SEE, which are indicated as **red** trajectories. This type of electrons can be suppressed either by applying a negative potential on the Wehnelt electrode, covering the lateral surface with a non-emitting material or by inserting an aperture to filter out the SEE.

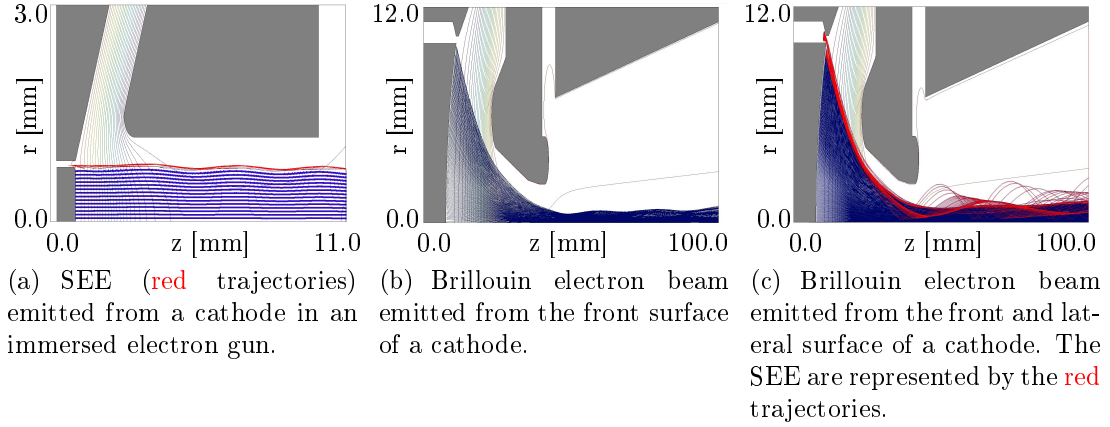


Figure 4.3.1: Influence of SEE on immersed and Brillouin electron beams.

### 4.3.2 Mixed regime emission

Simulating a cathode emitting in the thermionic regime is performed by adjusting the current density limit of the emission surface, which is related to the measured work function and temperature of the cathode. As discussed in Section 2.4.1, the strength of the applied electric field perpendicular to the emission surface governs the emission. When also assigning the lateral cathode surface as an emitting surface, the perpendicular field component is smaller by at least a factor of 10 than the field at the front surface. First the radial field component at cylindrical cathodes in gun geometries are usually small compared to the axial component. Second the Wehnelt electrode with applied negative potential is shielding the positive electric field from penetrating into the gap between cathode and Wehnelt. Nevertheless the field component on the lateral surface is high enough to allow space-charge limited emission, which intermixes with the thermionic front-emitted electron beam. The particles emit from emission nodes distributed as virtual point sources along the emission surface. In order to evaluate the mixing ratio, the maximum current density according to the cathode properties must be adjusted. To determine the emission regime of an area on the cathode surface, the local emission nodes have to be inspected to their emission current density. This is shown in Fig. 4.3.2(a). The extraction potential is varied at fixed maximal emission current and the surface and emitted current of thermionic emission can be established. The calculated emission surfaces for an extraction potential of  $U_{\text{ex}} = 4.5\text{kV}$  are shown in Fig. 4.3.2(b).

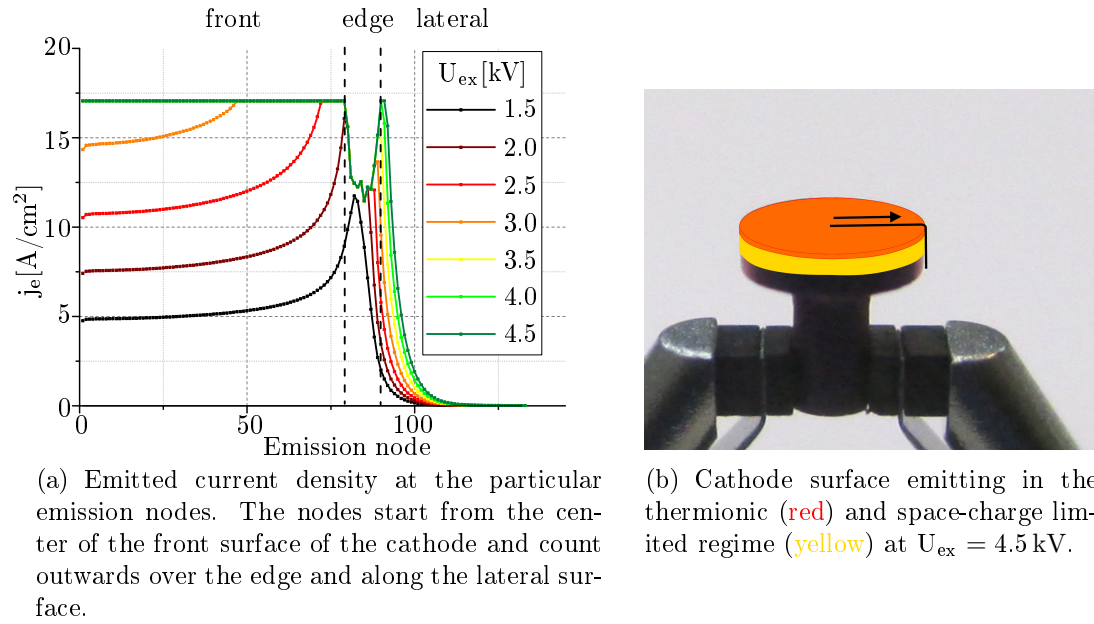


Figure 4.3.2: Spatial separation of emission surfaces emitting in different regimes.

### 4.3.3 Particle microscope

Extra challenges are posed by physical phenomena, which have to be addressed locally by increased particle numbers in the simulations, for instance the reflection of electrons near the beam axis due to the electric field inside a radially aligned electron collector. The total number of particles in simulations is determined by the meshing at the emission surface and can only be generally adjusted. The particle microscope increases locally the particle density in one plane for a higher phase space resolution of the beam. The magnification factor is 200, when substituting 5 trajectories with 1000 substituted. A magnification factor of 100-200 is usual. This script is applied for investigating three phenomena:

- SEE, discussed in Section 6.2
- ERPE (elastically reflected primary electrons), covered in Section 6.3
- The increase of the particle resolution in order to investigate the acceptance of the electron beam by a 5 T magnet in Section 7.9

#### 4.3.3.1 Setting up of the microscope

The particle microscope is introduced by an example how to resolve SEE emitted from the lateral surface of a cathode. The microscope records the electron beam at a certain z-plane in front of the emission surface and substitutes the particles within a specific radius with a defined number of sub-particles. To resolve the side-emitted current, the electron beam was first simulated “as is” in order to have the space-charge field of the primary electrons (PE) and to have a solution for benchmarking the microscope solution. In this example only the vertical recording plane is used, see Fig. 4.3.3. The script can handle both situations: A vertical recording plane in front of the cathode and vertical/horizontal recording planes combined covering directly the electrons emitting from from both lateral and vertical surfaces of the cathode. Both approaches yield equal results.

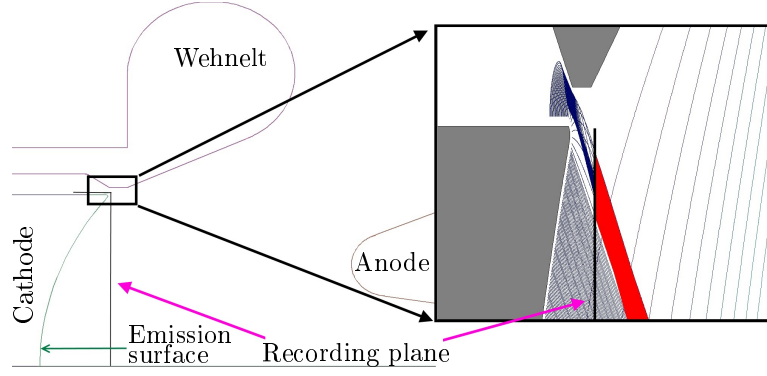


Figure 4.3.3: Recording plane at the cathode edge for recording particle properties with a zoom-in at the region of substitution. The substituted trajectories (red) are overlaid on the original trajectories.

#### 4.3.3.2 Substituting the electrons

In a second simulation with identical conditions the electron beam was traced and the recorded particle properties were handed over to the microscope script. Before executing the script one has to determine the number of trajectories, which have to be substituted, and the number of substituting trajectories. Then all particle properties like position, momentum, current, kinetic energy are linearly interpolated. In the investigations the outer 36 trajectories were substituted by 3600. To compare the correctness of the substitution, the original electron beam with its orbiting SEE was overlaid with the substituted side-emitted electrons, see Fig. 4.3.4(a) and Fig. 4.3.4(b). Those substituted electrons were traced downstream the magnet using the

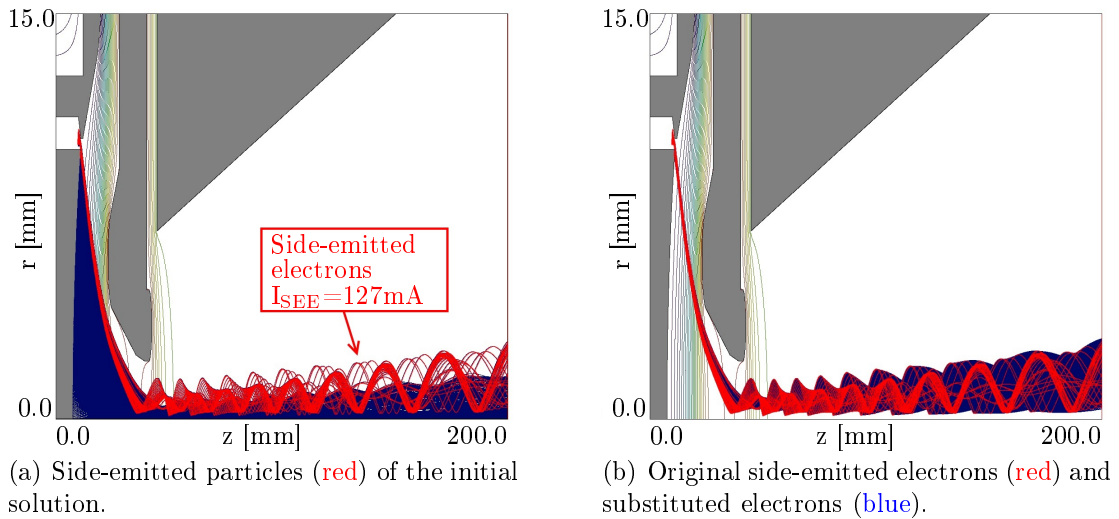


Figure 4.3.4: Tracing results of an applied particle microscope. The left figure shows the propagation of SEE, which generates the input data for the microscope. The right figure shows the propagation of the substituting particles overlaid with the substituted particles.

space-charge field of the non-substituted solution as initial electric fields. Tracing in FP does not consider space-charge interaction between particles. Therefore the substituted electrons follow the resulted space-charge field from the calculation of the initial electron beam.

#### 4.3.4 Back-scattered electrons

To obtain more realistic results of the power deposition inside the collector, back-scattered electrons (BSE) have to be taken into account. The energy distribution of BSE interacting with copper has its peak at approximately 80 % of the incident primary electron beam energy. Therefore they are able to leave the collector volume towards the cathode and constitute a loss current or they redistribute the deposited power among the different collector parts. As a result, a fraction of the deposited power at the water-cooled collector surface gets transported to non-cooled collector parts such as the front plate or the electron repeller. While trajectories are handled by FP, the process of generating BSE has to be treated externally. After simulating the incident PE a script reads out the impact position and energy, interception vector and the carried current. Then the energy and angular distribution of the BSE particles can be calculated. For the sake of statistical reliability the user has to choose a reasonably high number of BSE particles per incident primary electron (PE), while also considering the calculation capability of his computer for tracing their trajectories. For example, 100 BSE per PE fulfill the statistical recommendations of covering the take-off-angle distribution in a range of 180 degrees. In [Fang and Fukuda 2009] 3D calculations of back-scattered electrons for high-current electron beams were performed. Z.Fang recommends and traces 1,000,000 trajectories for reliable results in this simulation. Considering the radial symmetric geometry in our FP simulations, a total number of generated BSE trajectories in the order of 10,000 is in the same range of precision as the 3D calculations. Calculating the take-off distributions, which are governed by the impact angles of the incident PE, can be performed in three steps:

1. Calculate the ratio of BSE current to incident PE current.
2. Calculate the energy distribution of the BSE.
3. Calculate the angular distribution of the BSE.

After evaluating the particle properties of the incident electron beam, the script calculates the necessary distributions and assigns energy and take-off vector via a random generator to a chosen number of BSE per PE. For tracing the trajectories the script generates a trajectory-file for FP.

##### 4.3.4.1 Calculation of the back-scattering coefficient

In the literature a large number of formulas for calculating the BSE coefficient for all energy ranges and elements are suggested, a small selection are [Ali and Rogers 2008, Chaoui and Bouarissa 2004, del Giorgio et al. 1989, Hershcovitch and Kponou 1993, Staub 1994, Werner et al. 1982, Yadav and Shanker 2007a]. In general the formula for the angular dependent coefficient consists of a factor, which contains the back-scattering coefficient for perpendicular intercepting electrons ( $\theta_{in} = 0$ ), and an angular dependent scaling factor. The first factor,  $B_0$ , is calculated according to [Staub 1994]:

$$B(\theta_{in} = 0) = B_0 = \beta \left[ 1 - e^{((-6.6 \times 10^{-3})\beta^{-2.5}Z)} \right] \quad (4.3.1)$$

Here,  $\beta$  is an energy dependent scaling number,  $E_e$  in [keV]:

$$\beta = 0.4 + 0.065 \ln E_e \quad (4.3.2)$$

$Z$  is the atomic number of the target solid, for instance  $Z = 29$  for copper as collector material. Since many measurements were performed for copper and its neighboring elements, this formula is optimal for those elements. With the use of scaling factor  $A_0$  according to [Yadav and Shanker 2007b], where the scaling of  $B(\theta_{in})$  is investigated, the final expression can be written as:

$$B(\theta_{in}) = B_0 \cdot e^{A_0(1-\cos(\theta_{in}))} = B_0 \cdot e^{(-\ln B_0 - 0.119)(1-\cos(\theta_{in}))}. \quad (4.3.3)$$

$B(\theta_{in})$  is dependent of the electron energy and the impact material and scales the current carried by the BSE trajectories. Therefore the total electron current in the iteration for calculating BSE trajectories scales down as shown in Fig. 4.3.5.

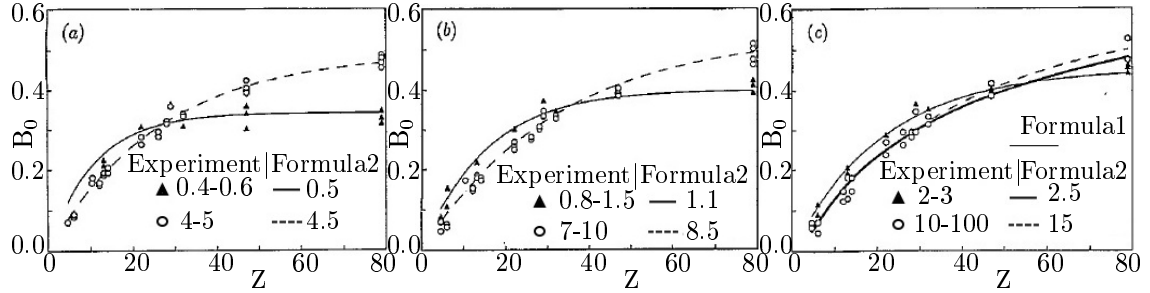


Figure 4.3.5: Back-scattering coefficient at normal incidence  $B_0$  for different  $E_0$  in [keV], as a function of the atomic number  $Z$  of the scattering target. Symbols, experimental data, broken and full curves at representative values for  $E_0$ , [Staub 1994]. Formula (2) is referring to Eq. 4.3.3. Formula (1) is a simplified approximation used in [Staub 1994].

#### 4.3.4.2 Calculation of the energy distribution

The energy distribution of the BSE according to [Staub 1994] can be expressed as:

$$g(E/E_0) = -\frac{\partial \eta(E/E_0)}{\partial E} \quad (4.3.4)$$

$$\eta(E/E_0) = S \exp \left[ - \left( \frac{70 |\ln B(\theta_{in})|^4}{1 - \left( 1 - \exp \left( -6 |\ln B(\theta_{in})|^{-3/2} \right) \right) (E/E_0)^2} \right)^{0.27} \right] \quad (4.3.5)$$

$E_0$  is here the kinetic energy of the incident electron. This distribution is weighted with the normalization factor:

$$S = B(\theta_{in}) \exp \left[ 70 \left( |\ln B(\theta_{in})|^4 \right)^{0.27} \right] \quad (4.3.6)$$

Since this distribution is derived from fittings, all dependencies of angle, energy and material are confined in the  $B(\theta_{in})$ -variable. One has to note that due to the insufficiently fitted origin, see Fig. 4.3.6, this distribution is underestimating the low-energy tail at an electron energy around 1 keV due to non-negligible elastic back-scattering in this range.

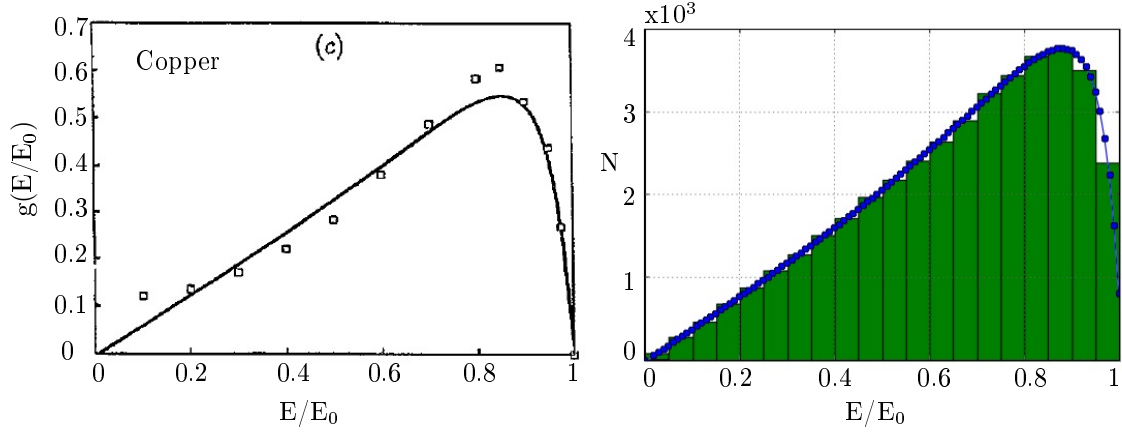


Figure 4.3.6: Left: Energy distribution for an incident energy  $E_e = 20$  keV at normal incidence angle, [Staub 1994]. Right: Energy distribution for an incident energy  $E_e = 11.9$  keV (results of the BSE script) generated with  $2 \cdot 10^5$  particles.

#### 4.3.4.3 Calculation of the angular distribution

First one has to distinguish between two cases: the impact vector of the primary electron is perpendicular to the surface or the PE intercept with a non-perpendicular angle. For the perpendicular case the angular distribution of BSE obeys Lamberts cosine law, see Fig. 4.3.7. In case of non-perpendicular incident angles the approach,

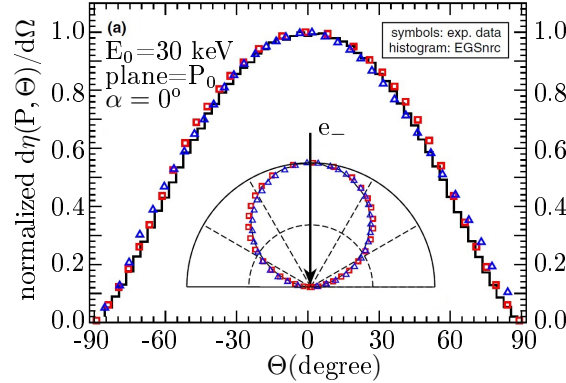


Figure 4.3.7: Solution of Lamberts law [Ali and Rogers 2008] and the resulting distribution using the BSE script.

published by [Valfells et al. 2002], is used. In this equation a perpendicular to the surface intercepting electron has an incident angle  $\theta_{in} = 90^\circ = \pi/2$ . If  $\theta_{in}$  is close to  $\pi/2$ , the results will converge to a cosine-like solution. In the following equations some conventions were made.  $\theta_\pi$  is here the maximal take-off angle of  $180^\circ = \pi$ ,  $n = 3$  and  $\theta_{out}$  is the investigated take-off angle in radians. The angular distribution  $f(\theta_{out})$  of a take-off angle  $\theta_{out}$  in the interval  $[0, \pi]$  is defined as:

$$f(\theta_{out}) = M(\theta_\pi, \xi, n) \frac{\theta_{out}(\theta_\pi - \theta_{out})}{(\theta_{out} + \xi)^n} \quad (4.3.7)$$

The peak of the take-off angle-distribution  $\xi$  is calculated as:

$$\xi = \frac{(n-1)\theta_\pi\theta_{in} + (2-n)\theta_{in}^n}{\theta_\pi - 2\theta_{in}} \quad (4.3.8)$$



$M(\theta_\pi, \xi, n)$  is the normalization constant for this distribution:

$$M(\theta_\pi, \xi, n) = \frac{1}{\theta_\pi(\tau(\theta_\pi) - \tau(0)) - (\rho(\theta_\pi) - \rho(0))} \quad (4.3.9)$$

$\tau(\theta_{\text{out}})$  and  $\rho(\theta_{\text{out}})$  are fitting parameters for the normalization function:

$$\tau(\theta_{\text{out}}) = \frac{-1}{\theta_{\text{out}} + \xi} + \frac{\xi}{2(\theta_{\text{out}} + \xi)^2} \quad \rho(\theta_{\text{out}}) = \frac{2\xi}{\theta_{\text{out}} + \xi} - \frac{\xi^2}{2(\theta_{\text{out}} + \xi)^2} + \ln(\theta_{\text{out}} + \xi) \quad (4.3.10)$$

Two solutions of Eq. 4.3.7 are shown in Fig. 4.3.8 for an incident angle close to  $0^\circ$  and around  $45^\circ$ . Fig. 4.3.9 shows the solution of the previous equation in comparison

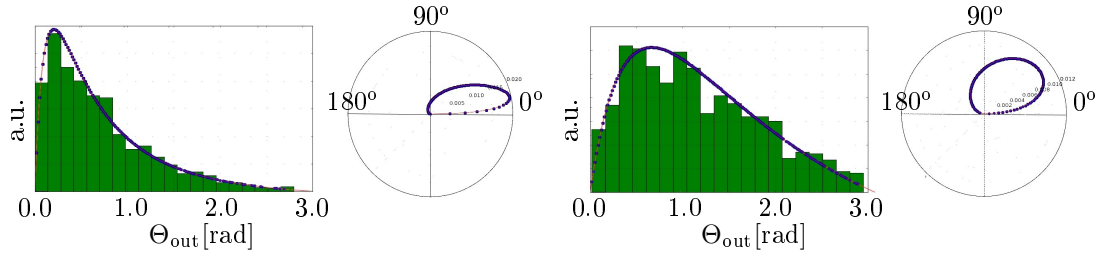


Figure 4.3.8: Solutions of Eq. 4.3.7 for an incident angle  $\Theta_{\text{in}} = 12^\circ$  (left) and for an incident angle of  $\Theta_{\text{in}} = 39^\circ$  (right).

with measured results [Darlinkski 1981]. The calculated angular distribution is energy independent, which is contradictory to the measurements. As a consequence the number of BSE particles, which have the same take-off angle as the incident angle, are under-estimated.

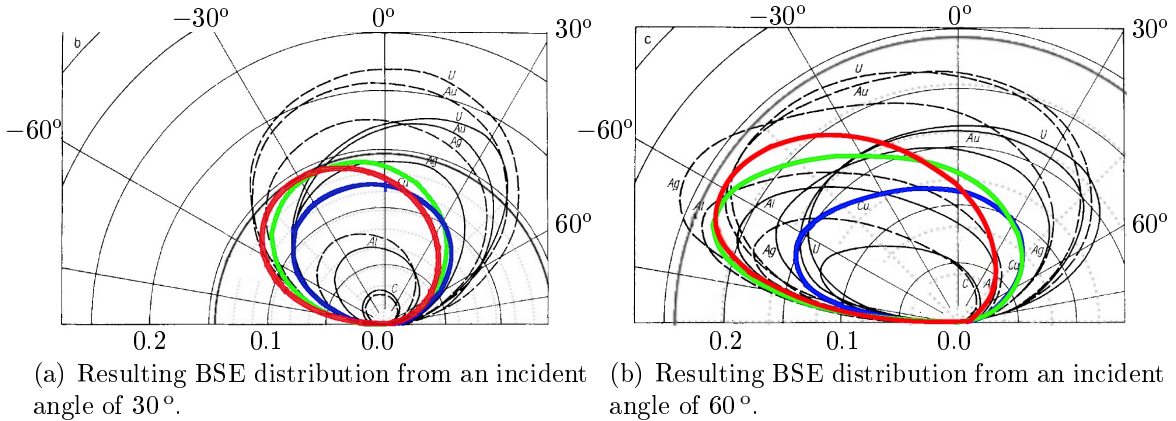


Figure 4.3.9: Angular distribution of BSE from a copper-target. Measured distributions [Darlinkski 1981] compared with calculated results. The blue line shows the measured BSE distribution for an incident energy of 5 keV, the green line represents the measured results with an incident energy of 30 keV, the red line is the energy independent distribution according to Eq. 4.3.7.

## 5 Characterization of TwinEBIS

### 5.1 TwinEBIS - Machine description

The general setup of TwinEBIS is shown in Fig. 5.1.1. In this design the electrostatic assembly, consisting of the electron gun, the drift tube assembly and the electron collector, is mechanically independent from the superconducting solenoid. The electron beam is emitted from the electron gun located in the gun cross, passes the drift tube assembly (consisting of nine separate drift tubes to provide the axial confinement of the ion trap) and is absorbed in the collector located in the collector cross. The superconducting solenoid generates a magnetic field of  $B = 2\text{ T}$  inside the trapping region. The magnetic field at the cathode, positioned at the axial position of the iron shield of the solenoid, is  $B_c \approx 200\text{ mT}$ .

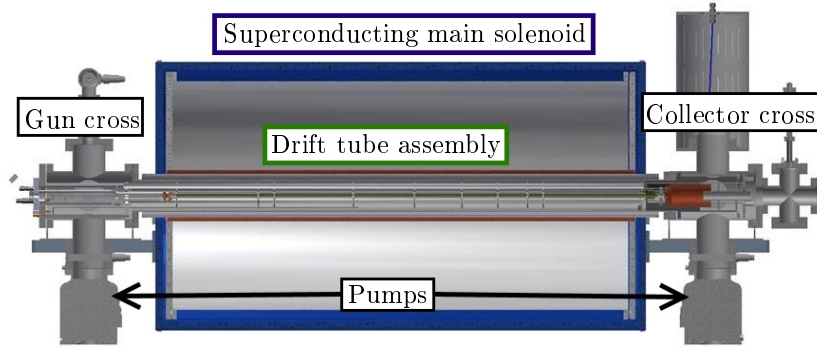


Figure 5.1.1: General setup of TwinEBIS. The electron gun is placed in the gun cross. The generated electron beam is guided through the drift tube assembly and is compressed by the B-field generated by the superconducting solenoid. The electron beam will be recovered in the collector, which is placed in the collector cross.

A more detailed plot of the electron gun is shown in Fig. 5.1.2(a). The electrons are emitted from a heated cathode, a  $\text{LaB}_6$  crystal with a radius of  $r_c = 0.85\text{ mm}$ , where an electric field is applied. This electric field is established by the potential difference between the anode electrode and the cathode, which are assembled with a distance of  $d_{\text{cath-anode}} = 1.34\text{ mm}$ . The Wehnelt electrode can be set on a different potential relative to the cathode potential and fulfills two purposes. First, it ensures that the applied electric field distribution is perpendicular and homogenous to the cathode surface. Second, when applying a potential lower than the cathode potential, it reduces the emission surface of the crystal to suppress SEE and favor front emission. The electron beam enters the trapping region after passing the anode. Here the first

drift tube is on the same electrostatic potential as the anode. The inner barrier of the axial ion trap is established by a positive potential on the second drift tube. The potentials of the following seven drift tubes can be adjusted individually according to the desired potential distribution of the ion trap. Fig. 5.1.2(b) shows the EBIS-assembly in the collector cross, where the electron beam gets absorbed in the collector. The collector potential is adjusted to 2 kV higher than the gun potential. The suppressor is kept on a potential approximately 0.3 kV lower than the collector potential to suppress BSE and ERPE. The extractor is adjusted permanently to  $U_{\text{ext}} = -8.5 \text{ kV}$  relative to the gun potential. The electron beam starts expanding before reaching the suppressor due to the reduction of the magnetic field. This is achieved by the iron shield around the collector assembly.

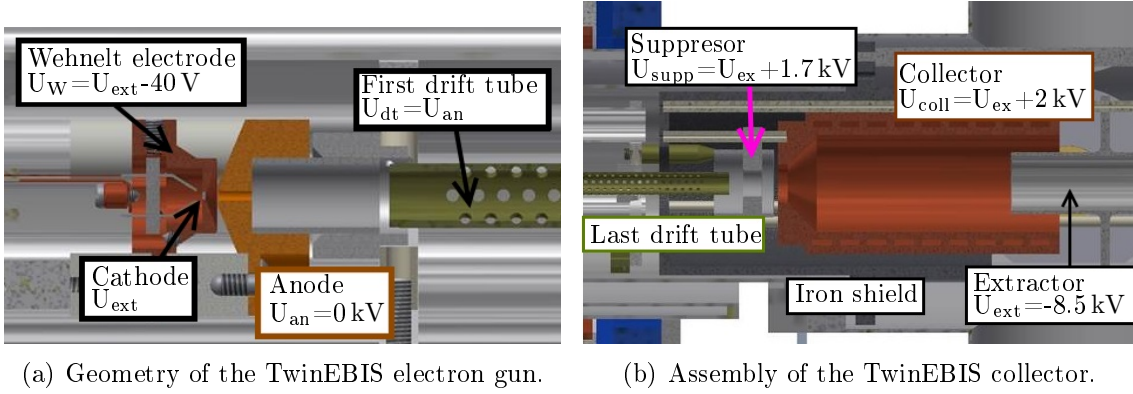


Figure 5.1.2: Detailed view of the gun and collector volumes with operational potentials.

When operating the source equipped with a  $\text{LaB}_6$  cathode, a constant oxygen flow has to be provided. This is realized by a gas-supply tube close to the cathode. Because the pressure is measured at a port at the gun and collector cross, the pressure in the volume between anode and cathode is unknown. With a Monte-Carlo program [Molflow+] the geometry of TwinEBIS can be imported and the oxygen flow in the molecular regime can be simulated as shown in Fig. 5.1.3. Here the gauge at the gun cross is indicated as a red circle. The Wehnelt and anode electrode are shown as red geometries. The green lines are the traced oxygen molecules. Simulation series with varied oxygen pressures show that the pressure in front of the cathode is a factor 10 higher the pressure measured at the gauge. All pressures in this chapter are measured values. To derive the pressure in front of the cathode one has to multiply the stated value with 10.

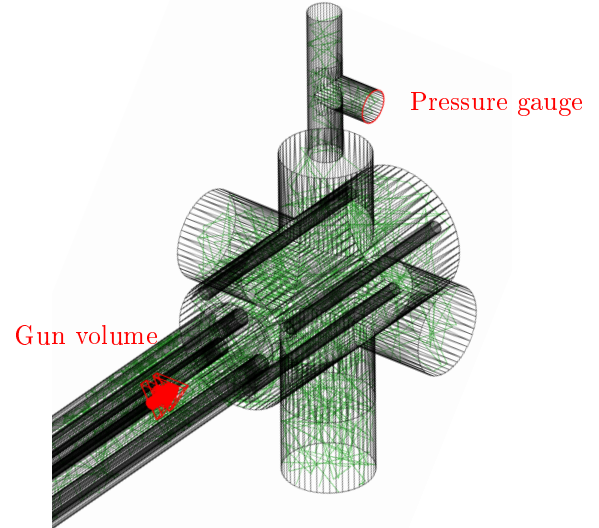


Figure 5.1.3: Meshing of the gun-cross geometry. The red circle is the pressure gauge position. The lower red geometry is the electron gun.

## 5.2 The LaB<sub>6</sub> cathode

The standard cathode providing an electron beam in the REXEBIS charge-breeder is a LaB<sub>6</sub> crystal, which has a work function of  $\Phi \approx 2.7\text{ eV}$ . A typical assembly of the electron gun with an installed cathode is shown in Fig. 5.2.1. The measured perveance of the electron gun is shown in Fig. 5.2.2(a). For the correct fitting range of data points for the perveance evaluation, it is necessary to determine at which extraction potential the cathode emits solely in the space-charge limited regime and at which extraction potential thermionic emitted current contributes to the total emitted current. Fig. 5.2.2(b) shows the emission curve at  $T_c = 1814\text{ K}$  from Fig. 5.2.2(a). With simulations, described in Section 4.3.2, the emission current from the cathode was evaluated for the contribution of space-charge limited and thermionic current to the total emission current. The simulated total emission current follows the measured current distribution. The cathode emits completely in space-charge limited regime at extraction potentials below  $U_{\text{ex}} = 500\text{ V}$ . When the extraction potential increases, the front surface of the cathode close to the cathode edge starts emitting in thermionic limited regime. This area of thermionic emission expands rapidly towards the center of the front surface of the cathode. Above an extraction potential of  $U_{\text{ex}} = 2\text{ kV}$  the complete front surface emits in the thermionic limited regime and space-charge limited current emits only from the lateral surface.

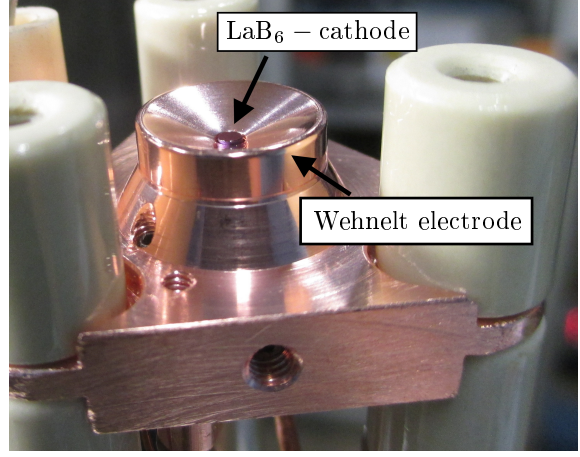
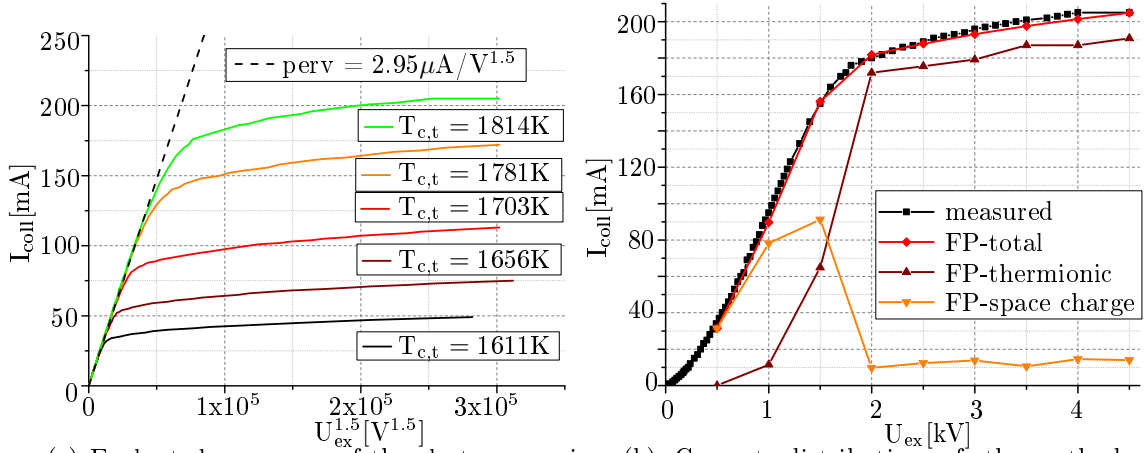


Figure 5.2.1: A LaB<sub>6</sub> cathode mounted into the Wehnelt electrode.



(a) Evaluated perveance of the electron gun installed in the TwinEBIS for different cathode temperatures.  $I_{\text{coll}}$  is the current deposited in the collector.

(b) Current distribution of the cathode at  $T_c = 1814\text{ K}$  compared to simulation results showing the fraction of space charge limited and thermionic current to the total emitted current.

Figure 5.2.2: Evaluation the performance of the electron gun installed in TwinEBIS by simulation-supported measurements.

By increasing the extraction potential the field penetrates deeper into the gap, which extends the thermionic emitting area on the lateral surface and shifts the space-charge emitting surface away from the front surface. This leads to the situation where the total emission current of the cathode always has a constant background of space-charge limited emission current at higher extraction potentials. A summarized evaluation of the contribution of space charge limited and thermionic emitted current is shown in Fig. 5.2.3(a). The lines represent the measured current, compare with Fig. 5.2.2(a), the squares are the total current as results of simulations. Thermionic emitted current is represented by up triangles connected with a dotted line and space-charge limited current by down triangles. Comparing the contribution of space-charge limited current to the total emission current at different cathode temperatures shows that lower cathode temperatures lead to a lower contribution of space-charge limited current. The reason for the lower contribution is that the local emission surface of the cathode reaches the thermionic emission regime at a lower extraction potential. To evaluate the work function, one can express Eq. 2.4.1 so that  $\ln(j_e)$  is a function of  $\sqrt{E} \approx \sqrt{U_{\text{ex}}/d_{\text{cath-anode}}}$ . When the measured emission current is plotted according to the previously mentioned dependencies, it results in a so-called Schottky-plot as shown in Fig. 5.2.3(b). The slope of the thermionic plateau can then be fitted with a line. The field correction term vanishes at the intersection of the fitting line and the y-axis ( $\Delta\Phi = 0$ ). This results in a hypothetical current density of a cathode emitting with a work function without the Schottky correction. This current density inserted into the simplified Richardson-Dushman equation yields the work function. For comparison, the work function from the intersection of the slope of the simulated bare thermionic electron beam, see Fig. 5.2.3(a), is also noted in the legend in Fig. 5.2.3(b). Comparing the work functions evaluated from the measurements and the simulations show that the space-charge current-contribution increases the work function by less than 30 meV.

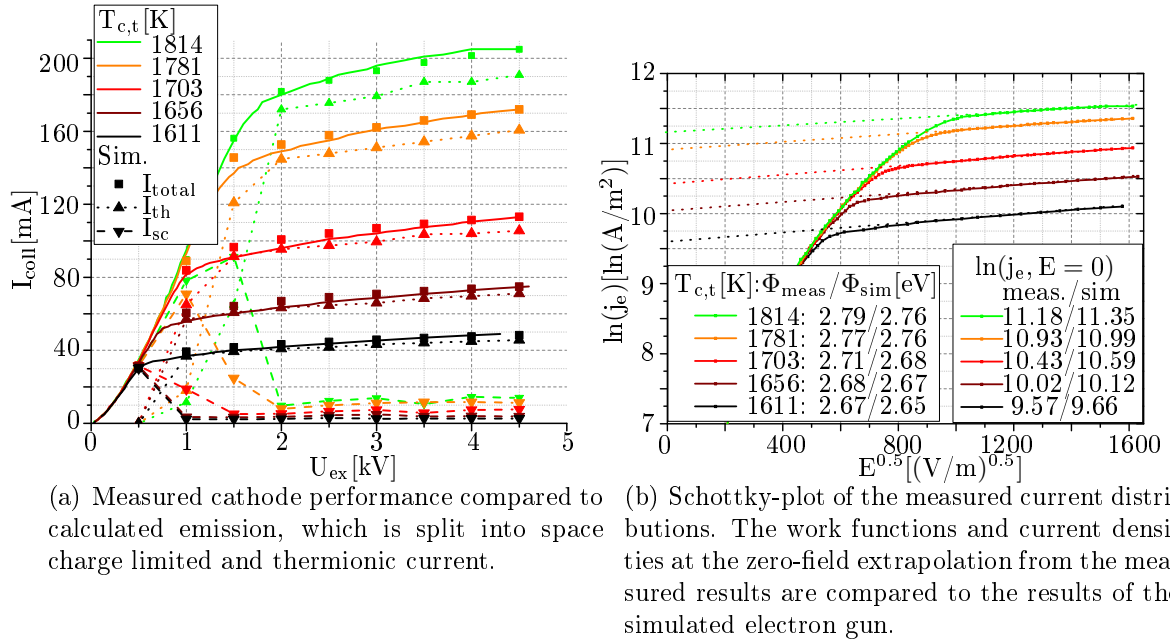


Figure 5.2.3: Results of work-function measurements of the  $\text{LaB}_6$  cathode installed in TwinEBIS.

The cathode temperature is measured during the experiments with a disappearing filament pyrometer. Because the cathode is not a perfect emitter due to a material-dependent emissivity constant, the true cathode temperature is lower than

the measured temperature. If the cathode is a perfect emitter, a so-called black body, the measured temperature would equal the true temperature. The electromagnetic radiation of black bodies is described by Planck's law:

$$\frac{dE(\lambda, T)}{d\lambda} = \frac{\epsilon 2\pi hc^2}{\lambda^5} \frac{1}{e^{hc/\lambda k_B T} - 1} \quad (5.2.1)$$

Here,  $h$  is Planck's constant and for a black body the emissivity  $\epsilon$  has the value 1. For real solids, also called gray bodies, a material-dependent value  $0 < \epsilon < 1$  has to be used. For instance the cathode manufacturer AP-Tech reports an emissivity of a LaB<sub>6</sub> cathode of  $\epsilon = 0.765$  at a wavelength of  $\lambda = 650$  nm. A conversion law between measured and true temperature is established by comparing Eq. 5.2.1 for a black and a gray body.

$$\frac{dE(\lambda, T_m)}{d\lambda} = \frac{2\pi hc^2}{\lambda^5} \frac{1}{e^{hc/\lambda k_B T_m} - 1} = \frac{\epsilon 2\pi hc^2}{\lambda^5} \frac{1}{e^{hc/\lambda k_B T_t} - 1} = \frac{dE(\lambda, T_t)}{d\lambda} \quad (5.2.2)$$

$T_m$  is the measured temperature from the black reference body and  $T_t$  is the true temperature of the gray-body cathode. The exponent in the denominator is greater than  $10^9$  above temperatures of 1000 K. Therefore the denominator can be simplified.

$$\frac{2\pi hc^2}{\lambda^5} \frac{1}{e^{hc/\lambda k_B T_m}} = \frac{\epsilon 2\pi hc^2}{\lambda^5} \frac{1}{e^{hc/\lambda k_B T_t}} \quad \longrightarrow \quad \epsilon = e^{\frac{hc}{\lambda k_B} \left( \frac{1}{T_t} - \frac{1}{T_m} \right)} \quad (5.2.3)$$

This can be further simplified to the conversion equation:

$$\frac{1}{T_t} = \frac{\lambda k_B}{hc} \ln(\epsilon) + \frac{1}{T_m} = 4.518 \cdot 10^{-5} \cdot \ln(\epsilon) + \frac{1}{T_m} \quad (5.2.4)$$

Although the value of emissivity is provided by the manufacturer as a constant temperature-independent value, the emissivity is usually temperature-dependent, as shown in Fig. 5.2.4. The temperature-dependent emissivity used for evaluating the true cathode temperature  $T_{c,t}$  of a LaB<sub>6</sub> cathode in this thesis is shown as the **red** dashed line. The temperature correction  $\Delta T = T_m - T_t$  for different emissivities is shown on the right scale. The black line shows the temperature correction for a constant emissivity of  $\epsilon = 0.765$ . The temperature correction for the emissivity, plotted as **red** dashed curve, is shown as a gray line. Using the temperature-dependent emissivity measured in [Kuznetsov 1994] results in a temperature correction shown as a **dark red** line. Comparing the particular emissivities at higher temperatures above a measured cathode temperature of  $T_{c,m} = 1700$  K shows significant deviations of the temperature corrections. When assuming a constant emissivity for a cathode operating at temperatures above  $T_{c,m} = 1900$  K, the true temperature will be overestimated.

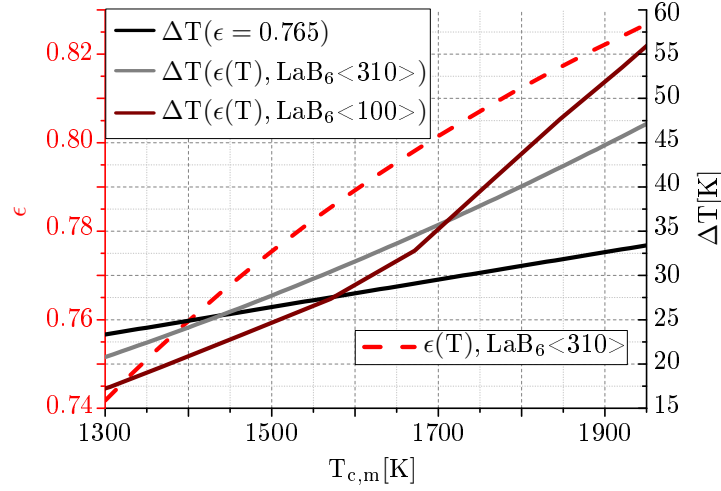


Figure 5.2.4: Temperature dependent emissivity indicated by the dashed line. The black line is the temperature correction assuming a constant emissivity of  $\epsilon = 0.765$ . The gray and dark red lines are the temperature corrections according to the temperature dependency of the library source and [Kuznetsov 1994].

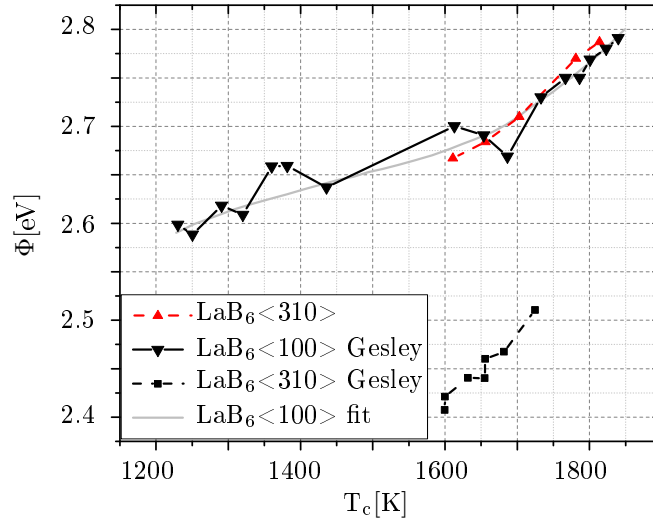


Figure 5.2.5: The measured temperature dependent work function of  $\text{LaB}_6$  in comparison with results from [Gesley and Swanson 1984].

The results from the Schottky-plot shown in Fig. 5.2.3(b), the measured cathode temperature and the calculated work function, are shown in Fig. 5.2.5 as red up triangles. Evaluating the temperature dependency of the work function shows a distribution of  $\Phi = 1.66 \text{ eV} + 6.20 \cdot 10^{-4} \text{ eV/K} \cdot T_c [\text{K}]$ . Comparing the measured results with the temperature-dependent work functions for  $\text{LaB}_6$  of  $1.23 \cdot 10^{-4} \text{ eV/K} \cdot T_c [\text{K}]$  reported by [Goebel and Watkins 2010] disagrees with the measured work function and its temperature dependence. The measured work function and its temperature dependency of the  $\text{LaB}_6$  <310> installed in TwinEBIS equals the work function

and temperature dependency of a  $\text{LaB}_6\langle 100 \rangle$  crystal measured by [Goebel and Watkins 2010]. The fit of the work function, shown as a gray line, indicates that the temperature dependency of the work function increases at temperatures higher than  $T_c = 1600$  K. A smaller temperature dependency of  $10^{-4} \text{ eV/K} \cdot T_c[\text{K}]$  was reported by Kuznetsov [Kuznetsov 1994], although this was at a lower temperature range of 1100 to 1500 K where the dependency of the work function on the cathode temperature is expected to be smaller.

The performed measurements show that the work function of a  $\text{LaB}_6\langle 310 \rangle$  crystal is equal to a  $\text{LaB}_6\langle 100 \rangle$  crystal under our working conditions. Extrapolating the work function to higher temperatures, one operates at temperatures of  $T_c = 2355$  K in order to meet at the REXEBIS design value of current emission  $I_e = 0.5$  A. Such high temperatures shorten the cathode lifetime significantly. The shortened cathode lifetime shows that  $\text{LaB}_6$  as cathode material is not adequate to operate the REXEBIS charge breeder in a high current emission regime.

### 5.3 The IrCe cathode

As reported by [Kuznetsov 2004], an IrCe crystal provides a current density significantly higher than  $\text{LaB}_6$ . This promises a longer cathode lifetime when operating the electron gun in high emission regimes. The temperature dependent work function of the activated IrCe crystal was characterized. Activation is here the reduction of the work function by cathode heating at  $\approx 2000$  K for three days. The results for an activated IrCe crystal with a radius of 0.75 mm are shown in Fig. 5.3.1. The evaluated perveance is  $1.81 \mu\text{A}/\text{V}^{1.5}$ .

The calculated work function as a function of the measured cathode temperature is shown in Fig. 5.3.2. The evaluated temperature dependency of the IrCe cathode is measured over a range from 1650 K to 1850 K. A linear fit results in a temperature dependency of  $\Phi = 1.41 \text{ eV} + 7.3 \cdot 10^{-4} \text{ eV/K} \cdot T_c[\text{K}]$ . These measurements disagree with the measured temperature dependency reported by [Kuznetsov 1994], where a temperature dependency of less than  $5 \cdot 10^{-5} \text{ eV/K}$  was measured. In [Kuznetsov 2004] a dependency of  $\Phi = 2.46 \text{ eV} + 8.75 \cdot 10^{-5} \text{ eV/K} \cdot T_c[\text{K}]$  is reported, which can also not be confirmed. In [Rao and Kultashev 1997] a work function of  $\Phi = 2.69 \text{ eV}$  at a cathode temperature of  $T_c = 1800$  K was measured, which agrees with the measurements discussed in this thesis. Due to the fact that IrCe is not so widely used amongst operating EBIS/T, the process of activation is not well documented. To distinguish an activated cathode from a cathode prior activation, the work function for a non-activated cathode is also shown as up triangles. The work function before the activation is measured to be 0.2 eV higher than for an

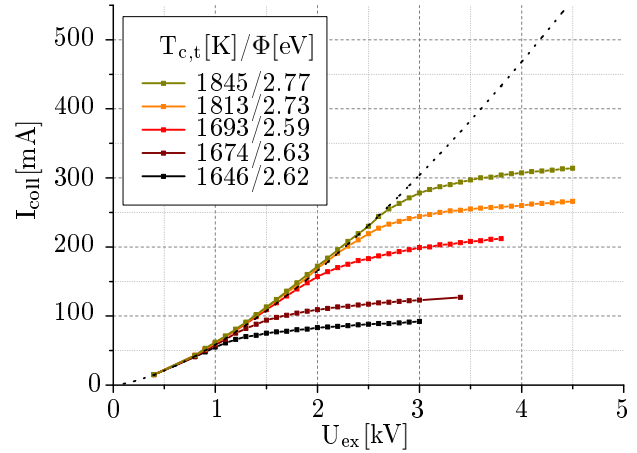


Figure 5.3.1: Measured emission properties and calculated work function of the activated IrCe crystal. The dashed line shows the measured perveance limit of the electron gun equipped with this crystal.



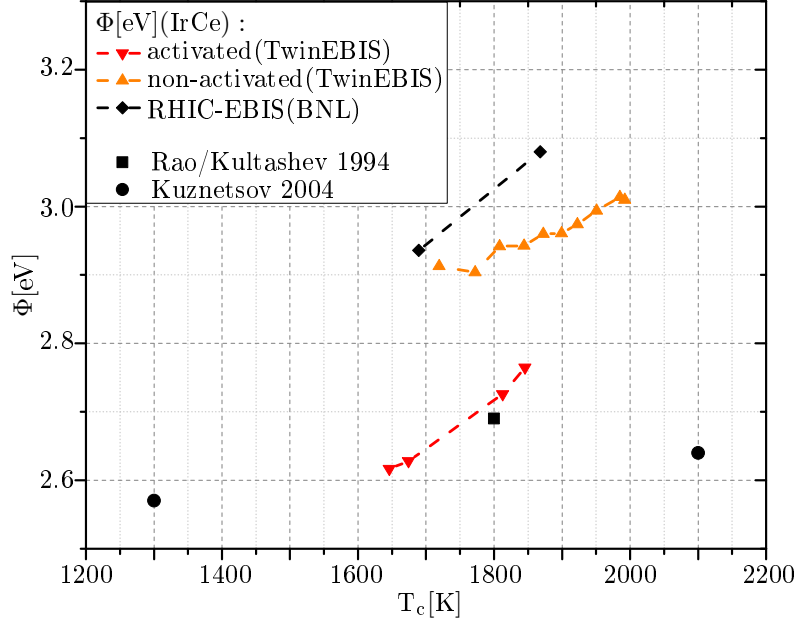


Figure 5.3.2: Temperature dependent work function of the activated IrCe crystal measured by Rao (square) and Kuznetsov (dots) and in this thesis (down triangles) compared a non-activated crystal calculated from the emission data of the RHIC-EBIS (rhombus) and in this thesis (up triangles).

activated crystal. In order to compare the state of the activated and non-activated cathode installed in TwinEBIS, the work function calculated from the emission properties recorded from an IrCe crystal installed in the **R**elativistic **H**eavy **I**on **C**ollider (RHIC)-EBIS (BNL) is shown. Comparing the emission density of a LaB<sub>6</sub> crystal to an IrCe, as shown in Fig. 5.3.3, indicates the higher emitted current thanks to the lower work function of IrCe.

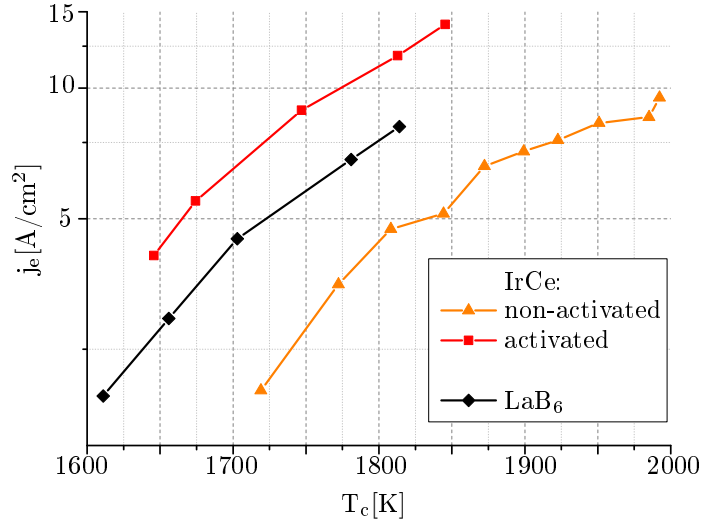
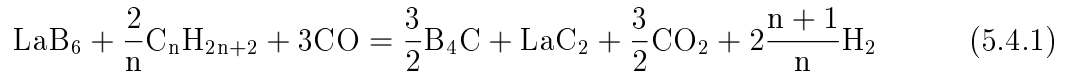


Figure 5.3.3: Measured current densities of the IrCe compared to LaB<sub>6</sub>.

## 5.4 Poisoning effects on LaB<sub>6</sub>

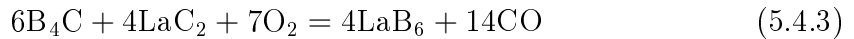
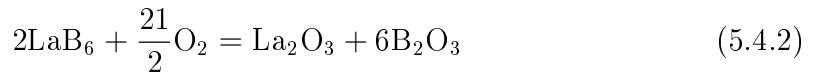
Operating the LaB<sub>6</sub> cathode at a pressure of  $3 \cdot 10^{-11}$  mbar leads to a reduced electron emission, which is also observed when leaving the cathode in the heated state without applied extraction potential for approximately six hours at this pressure. [Avdienko and Malev 1977] reports on the influence of the partial pressure of various residual gases, for instance O<sub>2</sub>, N<sub>2</sub>, CO, CO<sub>2</sub>, H<sub>2</sub>O, H<sub>2</sub> and hydrocarbons of different lengths, on the cathode emission. The equilibrium pressure of the reaction of hydrocarbons with the LaB<sub>6</sub> crystal depends exponentially on the hydrocarbon's molecular length. While the equilibrium pressure for a reaction with hydrocarbons, shown in Eq. 5.4.1, is  $1 \cdot 10^{-6}$  mbar for methane, the equilibrium pressure is  $1 \cdot 10^{-10}$  mbar for ethane.



Since a scan with a residual gas analyzer revealed that none of those previously mentioned hydrocarbons are present in the observed gun volume with a higher partial pressure than  $10^{-14}$  mbar, long-chained alkane-molecules evaporating from the pumps are suspected to be causing the cathode-poisoning. The carbon pads of the cathode holder, which evaporate at the heated state of the cathode, can be considered as another source. The following investigations focus on the cathode-reviving process rather than on the mechanisms avoiding cathode poisoning.

### 5.4.1 Cathode revival using oxygen

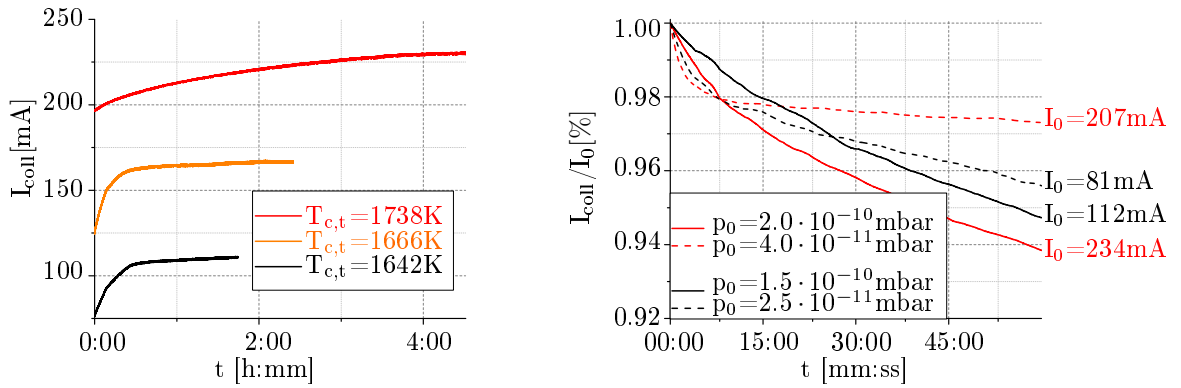
Oxygen has proven to be the most effective element for cleaning a LaB<sub>6</sub> cathode surface from carbon compounds. Because the poisoning is a permanently ongoing and cathode-temperature dependent process, the partial pressure of oxygen has to be adjusted carefully to keep the cathode at a state of maximum emission. The optimal pressure is usually 2-3 times higher than the base pressure of the cathode at a certain temperature T<sub>c</sub>. In [Goldstein and D.J.Szostak 1978] it is reported that an oxygen partial pressure above the optimal pressure reduces the emission because the O<sub>2</sub>-LaB<sub>6</sub> reaction dominates according to Eq. 5.4.2. Below and at the optimal pressure Eq. 5.4.3, describing the reviving process from a carbon poisoned cathode, dominates and balances the oxygen poisoning.



In Fig. 5.4.1(a) a reviving process of a LaB<sub>6</sub> cathode is shown for different temperatures. The distributions are aligned to the event of opening the leak valve into the gun volume and thus increasing partial O<sub>2</sub> pressure. The reaction speed of the reviving process depends on the state of initial poisoning of the cathode and of the cathode temperature. Higher cathode temperatures require higher oxygen flux

due to the temperature dependency of the chemical reaction. A slightly poisoned cathode with a reduced emission reacts immediately to the oxygen flux.

Here the emission increases by more than 30 % within 10 minutes. If oxygen is introduced to an partially revived cathode, the emission increases marginally as shown in Fig. 5.4.1(a) by the red distribution. When the oxygen flux is stopped, the cathode emission decreases according to the cathode temperature and the residual partial pressure of the remaining oxygen inside the gun volume as shown in Fig. 5.4.1(b). In the case of the full lines, the leak valve was closed and the oxygen supply stopped. The emission reduction increases with the cathode temperature as expected from the temperature dependency of the chemical poisoning process. The dashed lines show the poisoning process of a cathode after varying the temperature by changing the heating power when the leak valve is closed. The current was acquired after the cathode reaches its new emission level. Here the black dashed line is the measured current after decreasing the cathode temperature by 24 K, the red dashed line shows the measured current after increasing the cathode temperature by 96 K.



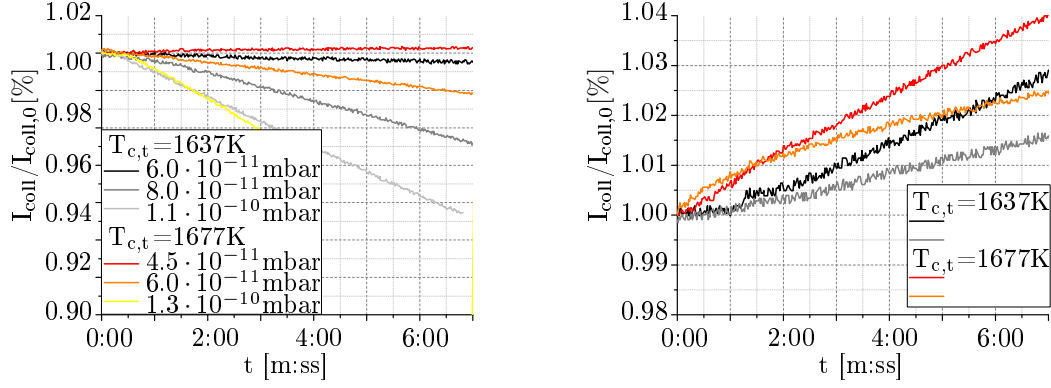
(a) Slopes of current increase for a revived LaB<sub>6</sub> crystal. The partial oxygen pressure is  $6.5 \cdot 10^{-11}$  mbar for the red and black distribution and  $8 \cdot 10^{-11}$  mbar for the orange distribution. (b) Temperature dependent poisoning process measured after closing the leak valve (solid lines) and varying the cathode temperature (dashed lines).  $I_0$  is here the emission current when the recording starts.

Figure 5.4.1: Reviving and poisoning process of the LaB<sub>6</sub> cathode installed at REXEBIS. The color code is shown in the left figure. The slope depends on the degree of poisoning and cathode temperature. The pressures in the right figure indicate the pressures before the measurement starts.

## 5.4.2 Effects of hydrocarbons on the cathode

As previously discussed, long-chained hydrocarbons are considered as a source of the poisoning reaction. In order to evaluate the effects of those molecules, methane was injected into the gun volume at different partial pressures. Fig. 5.4.2(a) shows the development of the emitted current after the leak valve has been opened for different partial pressures and cathode temperatures. As with the reviving process

using oxygen, the poisoning depends on pressure and cathode temperature. Higher pressure accelerates the poisoning mechanism for equal temperatures. Increasing the cathode temperatures at constant pressure also increases the poisoning due to a shift of the equilibrium pressure of the chemical reaction towards the educts. When interrupting the methane-flux to the cathode, the cathode immediately recovers, as shown in Fig. 5.4.2(b). All shown distributions were acquired with a cathode operating near the background pressure and are normalized to the emitted current before closing the leak valve.



(a) Poisoning process after injecting methane at different partial pressures and cathode temperatures. (b) Self-reviving process of the cathode after closing the methane-flux into the gun volume.

Figure 5.4.2: Effects of methane on the emission performance of the  $\text{LaB}_6$  cathode installed at REXEBIS.

### 5.4.3 Effects of neon on $\text{LaB}_6$

In order to verify that the poisoning is caused by chemical reactions on the cathode surface and not by sputtering, neon, an inert reactant with similar mass to methane, was injected into the gun volume. Neon ionizes in the electron beam between cathode and anode, accelerates towards the cathode and sputters the surface. Fig. 5.4.3 shows the emission current distribution at different neon partial pressures. The sputtering process induced by neon projectiles has no degrading effect on the cathode emission as shown in the plot. Therefore sputtering of light residual noble gases on the cathode surface can be excluded as a source for cathode poisoning.

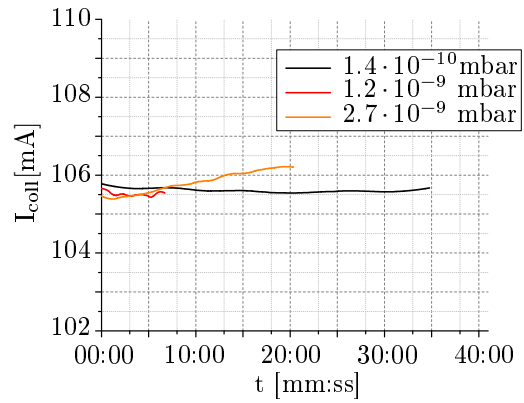


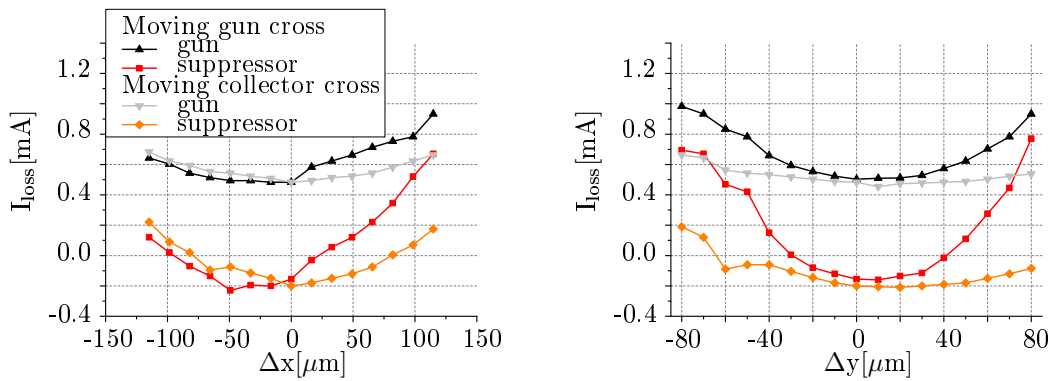
Figure 5.4.3: Current distribution of the  $\text{LaB}_6$  cathode during the injection of neon at different pressures in the gun volume.

## 5.5 Alignment dependent current losses

Electron losses limit REXEBIS and TwinEBIS from emitting a higher electron current. This section focus on the sources of loss current and techniques for minimizing the loss current.

The beam quality of the TwinEBIS with an immersed electron gun depends on the alignment of the cathode and the electrodes to the B-field axis. Eq. 2.3.1 describes the electron beam envelope in the case of a perfectly aligned source. Any radial misalignment of the electron gun relative to the magnetic field introduces an additional emission angle to the emitted electrons, which widens the electron beam. Furthermore, if the cathode is misaligned relative to the anode, an electrostatic beam distortion has to be considered. Radial misalignment and tilt of the cathode relative to the anode has to be considered due to the manual assembly of the electron gun. To compensate a misalignment, the electron gun is artificially misaligned with respect to the magnetic field axis. This procedure re-aligns the electron beam back on the center of the electron gun with the price of a wider beam radius. The electron gun with an arbitrarily misaligned cathode is considered centered, when no loss current can be observed on the anode and the general loss current measured on all power supplies is minimized.

To evaluate the alignment of the electron gun and the electrode assembly and also its sensitivity to radial misalignments, the gun and the collector cross were artificially misaligned in horizontal and vertical direction. Fig. 5.5.1(a) shows the misalignment dependent loss current when moving the gun and collector cross in the horizontal plane. Fig. 5.5.1(b) shows the loss current dependencies when moving the crosses in the vertical plane. Loss current can only be detected at the gun power supply and the separate suppressor power supply. Therefore the loss current is separated into loss current occurring on the gun power-supply, which indicates losses at the anode and the drift tubes, and the loss current occurring at the suppressor power-supply. The loss current is measured at both power supplies when moving one cross while the other remains in the centered position. In the figures the black and the gray curves represent the loss current measured at the gun power-supply. The red and the orange curves represent the loss current measured at the suppressor power-supply.



(a) Loss-current dependency on the horizontal misplacement of the gun and collector cross. (b) Loss-current dependency on the vertical misplacement of the gun and collector cross.

Figure 5.5.1: Loss-current dependency on the radial alignment of the electrostatic structure relative to the B-field axis.

The effect of misalignments of the gun and collector cross on a  $\mu\text{m}$ -scale illustrates the high sensitivity of TwinEBIS alignment. Moving the gun cross results in higher

loss current at both power supplies than moving the collector cross. This is caused by the misplacement of the cathode respectively by the misplacement of the electron gun with respect to the magnetic field of the solenoid, which leads to a wider electron beam and additional distortion of the electron beam propagation. According to Eq. 2.3.1 the immersed electron beam propagates with alternating electron beam radius with a certain radius and wave length. When misplacing the electron gun relative to the B-field axis the amplitude increases due to an initial angle of the B-field lines at the cathode surface. A cathode misplaced relative to the anode generates an electron beam with beam spread towards the direction of misplacement. Both displacements result in a wider, radially misplaced propagating electron beam. Separation of the last drift tube from the gun power-supply shows that  $> 99\%$  of the loss current is deposited on this electrode.

The last drift tube and the suppressor positioned at a location close to the rear iron shield with lower B-field strength compared to the magnetic field at the cathode. Because the electron beam radius scales with the magnetic field, the last drift tube and the suppressor have to conduct an electron beam at a larger size compared to that emitted at the cathode. Beam distortions caused by movements of the gun cross have therefore a larger effect on the loss current than moving the collector cross by  $\mu\text{m}$  at an optimally compressed electron beam.

The loss current caused by the widened or distorted electron beam at the last drift tube can be reduced by taking advantage of the lens effect. By applying a higher potential at the last drift tube as shown in Fig. 5.5.2 the electron beam accelerates and widens less. This indicates that the beam widening is governed by the ration between radial space-charge repulsion and axial de-/acceleration. To reduce the loss current a high potential has to be applied on this drift tube, which is the outer barrier of the axial ion trap. This prevents TwinEBIS from operating as a charge breeder.

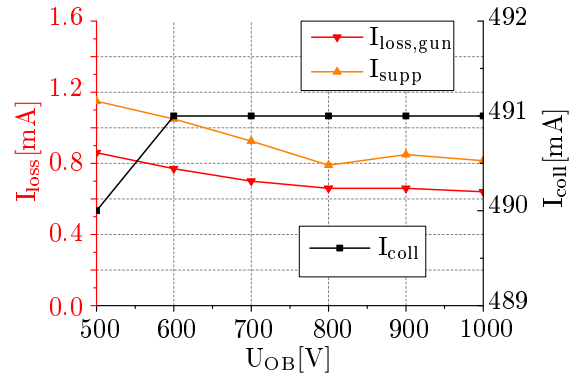


Figure 5.5.2: Loss current and emitted current measured at the collector, as function of the applied potential at the last drift tube.

To evaluate the influence of the Wehnelt on the loss current different Wehnelt potentials were applied at a constant extraction potential as shown in Fig. 5.5.3. When applying and increasing the Wehnelt potential, the varied electric field results in a negative potential at the lateral cathode surface. This suppresses SEE and decreases the electron beam radius and emitted current. A direct effect is the reduced pressure in the electron gun volume after applying a negative potential at the Wehnelt electrode. This indicates that side-emitted stray electrons, which impinge on the anode electrode and provoke out-gassing and therefore cause the higher pressure, are suppressed at the cost of less emitted total current.

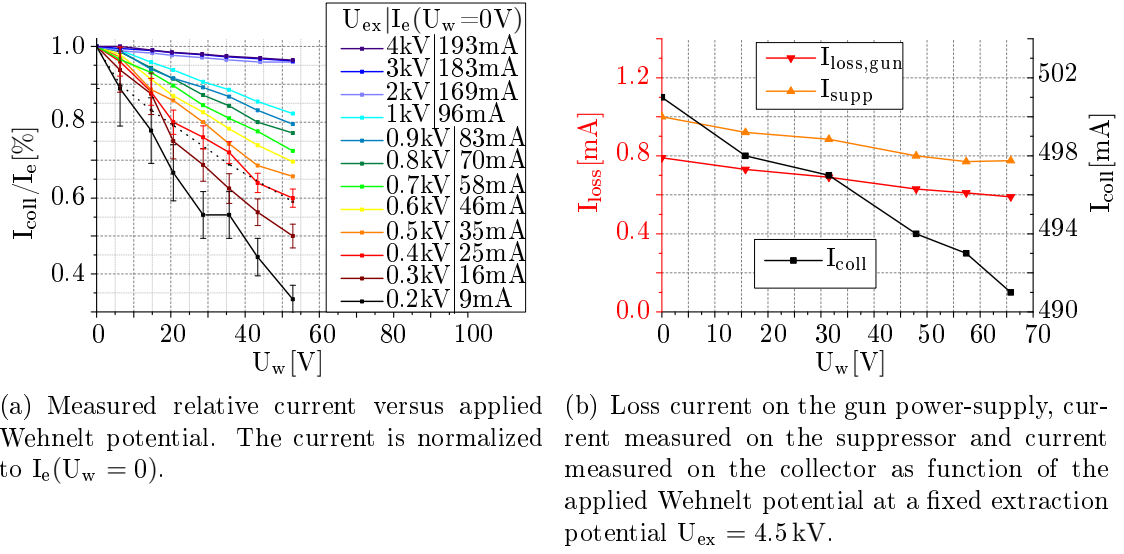


Figure 5.5.3: Emission of a LaB<sub>6</sub> cathode as a function of applied Wehnelt potential in the TwinEBIS gun.

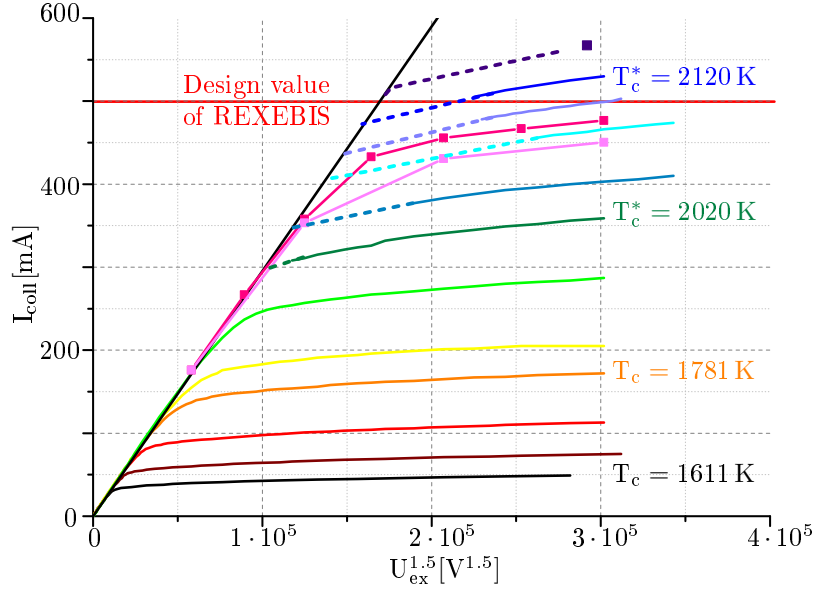
## 5.6 Approaching the design value of REXEBIS

REXEBIS should operate with a nominal emission current of  $I_e = 500$  mA, which was not achieved during previous operation. The first limiting factor is the necessary LaB<sub>6</sub>-cathode temperature to provide this current, which has to be above  $T_c = 2100$  K. Such temperatures shorten the cathode lifetime significantly from some kilo-hours down to a few hours [A.S. Gilmour 2011, p.56]. The second factor is the need for a significantly higher oxygen pressure, usually  $p > 10^{-9}$  mbar to prevent the heated cathode from getting poisoned. The third limiting factor is the high sensitivity of the loss current to misalignments of the electrode assembly. For the high current emission tests the alignment of TwinEBIS was set to minimize the loss current. By increasing the cathode temperature the cathode was able to operate in high current regime as shown in Fig 5.6.1(a).

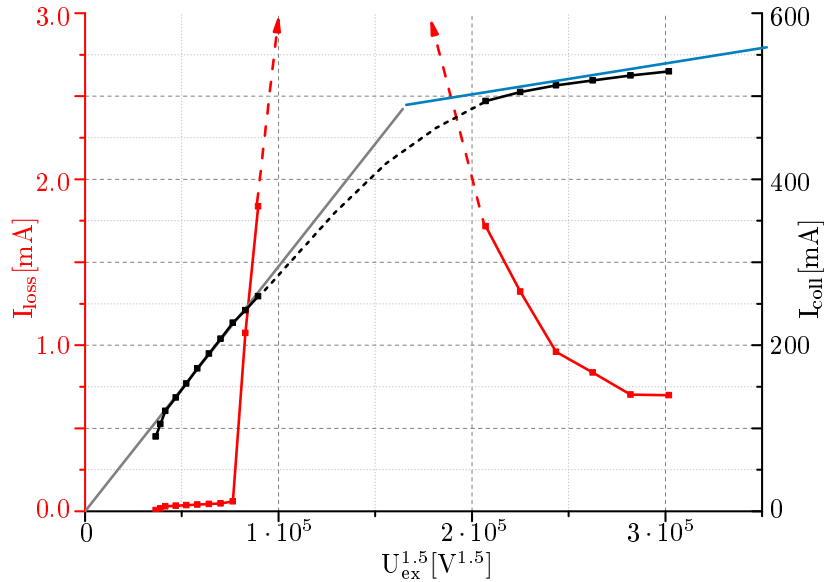
The five lowest measured I-U distributions are discussed in Section 5.2. The temperature measurement for the higher current distributions could not be performed, because the non-shielded observation window was getting doped due to the constant ion deposition during the measurements. The temperatures are extrapolated from the cathode heating-power dependency of the cathode temperature and marked as  $T_c^*$ . The measured distributions have a gap at the transition between space-charge limited emission and thermionic emission, indicated by the dotted lines between the solid measurement distributions. These dashed lines represent the extrapolated current distribution in order to connect the acquired space charge limited and thermionic current distributions. The higher the cathode temperature and therefore the thermionic plateau is, the wider the dashed gap extends. One explanation is the ratio between space charge repulsion and kinetic energy of the electron beam as stated in the previous section. The dotted distributions show complementary simulations according to the previously discussed approach, see Fig 5.2.3(b). Measurements at the high-current transition regime could not be performed due to the increasing loss current at the last drift tube, see Fig. 5.6.1(b). The source for the loss current is the misalignment of the cathode with respect to the anode, which has to be re-aligned by artificially misaligning the electron gun with respect to be

magnetic field axis. This wider beam expands before passing the last drift tube and causes loss current. This beam widening could be reduced by applying higher potentials at the last drift tube.

To surpass the region with extraordinarily high loss current a very high Wehnelt potential  $U_w = -400$  V has to be applied to reduce the electron beam radius. With the reduced electron beam the extraction potential can be increased until the thermionic plateau is reached. While operating TwinEBIS in the thermionic emission regime a Wehnelt potential of maximal  $U_w = -40$  V at an extraction potential of  $U_{ex} = 3.5$  kV is sufficient to keep the pressure in the gun volume and the loss current at the lowest level while providing an electron beam of 500 mA.



(a) Summarized cathode emission measurements with supporting simulations (dots&lines). The dashed lines indicate the theoretical emission.



(b) Loss current distribution dependent on the applied gun potential and resulting emission current.

Figure 5.6.1: Summarized electron-beam current performance of TwinEBIS.



The demonstrated high current operation verifies the technical design values of REXEBIS and TwinEBIS. The lifetime of the used cathode is shortened significantly as a consequence of the higher temperature. Also the need for higher electric potentials on the last drift tube for reducing loss current defeats the ability of operating a charge breeder, where the outer drift tube has to be switched to different potentials. These consequences are disadvantageous for an EBIS/T operating as a charge breeder in a user-facility as ISOLDE, where high reliability and stability for long term experiments are required.

## 6 Simulations of the HEC<sup>2</sup> gun

TestEBIS is an offline test bench for research and development at BNL. In cooperation between CERN and BNL the HEC<sup>2</sup> gun was developed [Pikin et al. 2014]. A Brillouin gun aiming to provide a high-current electron beam, which will be highly compressed in the 5 T field of the TestEBIS solenoid. At the maximum operation conditions the HEC<sup>2</sup> gun should provide a 10 A electron beam at an extraction voltage of  $U_{\text{ex}} = 49.2$  kV. According to calculations the Herrmann radius of the electron beam is expected to be  $r_e = 100 \mu\text{m}$  in the high-compression region at 5 T, which corresponds to a current density of  $j_e = 25.5 \text{ kA/cm}^2$ .

### 6.1 TestEBIS - machine description

The TestEBIS beam line is shown in Fig. 6.1.1. Here the HEC<sup>2</sup> gun is separated from the beam line by ceramic insulators to set the gun on higher potentials. Due to the extended beam line length and high electron current, two additional coils are implemented to generate a guiding magnetic field at electron gun and collector. The gun coil generates the matching magnetic field at the Brillouin electron gun. For instance, an electron beam of 10 A requires a magnetic field of 230 mT. The HEC<sup>2</sup> gun design is discussed in detail in [Pikin et al. 2014]. To guide the electron beam into the collector the electron collector coil (EC coil) generates the matching field. The magnetic field distribution from electron gun to collector reaches its minimum values of 35 mT between gun coil and solenoid and below 100 mT between solenoid and EC coil. Additional drift tubes guide the electron beam in the area of low magnetic field.

Table 6.1.1 shows the key parameter of REXEBIS and TestEBIS with the HEC<sup>2</sup> gun for comparison. Because the HEC<sup>2</sup> gun is assembled onto the non-modified TestEBIS, it is necessary to evaluate if the default beam line of TestEBIS is suitable for this electron gun. First, the acceptance conditions of the solenoid for the electron beam have to be evaluated. Second, since the electron beam power is increased by replacing the electron gun, it is necessary to investigate the capability of the collector to absorb the increased power of the HEC<sup>2</sup> electron beam.

Table 6.1.1: REXEBIS equipped with an immersed gun compared to the TestEBIS+HEC<sup>2</sup>-upgrade. The values for TestEBIS are design values, while the numbers for REXEBIS are operational values.

| Parameter                                   | HEC <sup>2</sup> + TestEBIS | REXEBIS |
|---|-----------------------------|---------|
| Electron current [A]                        | 10.2                        | 0.25    |
| Electron beam energy [keV]                  | 49.2                        | 4       |
| Maximum B-field [T]                         | 5                           | 2       |
| B-field on the cathode [mT]                 | 0.3                         | 200     |
| Cathode radius [mm]                         | 10.0                        | 0.8     |
| Fully compressed $r_e$ 80%[ $\mu\text{m}$ ] | 100.4                       | 257.5   |
| Full beam transport length [m]              | 3.1                         | 1.7     |

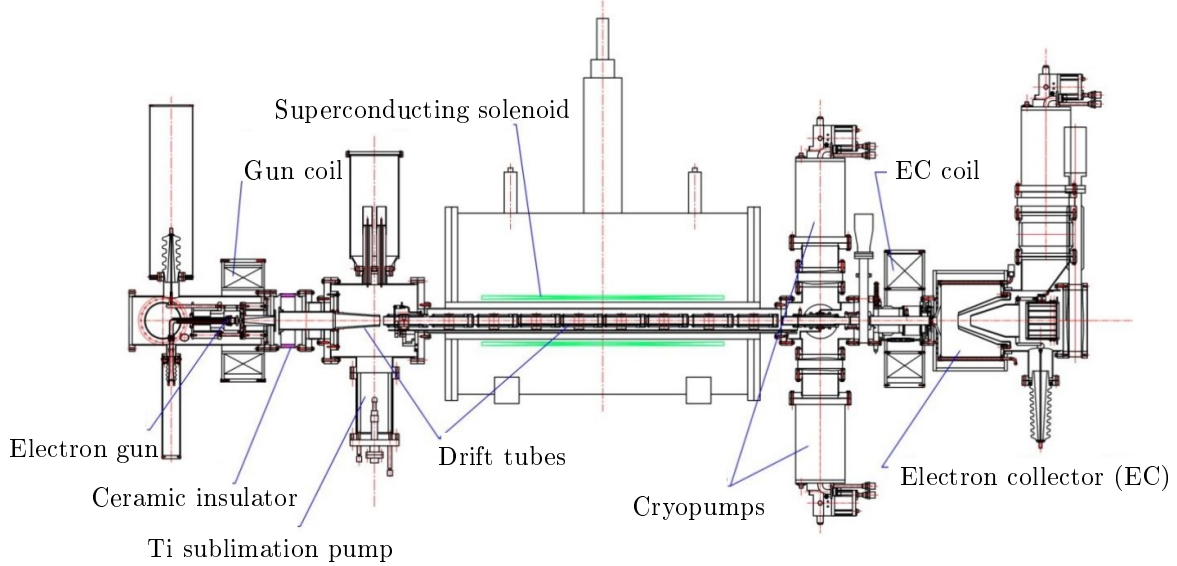


Figure 6.1.1: TestEBIS beam line with assembled HEC<sup>2</sup> gun [Pikin et al. 2014].

## 6.2 Evaluation of the loss current occurring at the anode

The increase of the emission current of the HEC<sup>2</sup> gun was limited during the commissioning phase. Excessive loss current occurred at the power supply of the anode. At an electron beam current of  $I_e = 1.8 \text{ A}$  and an applied extraction potential  $U_{\text{ex}} = 15.5 \text{ kV}$  a loss current of  $I_{\text{loss}} = 20 \text{ mA}$  was measured. One possible source of this loss current are SEE from the cathode as described in Section 4.3.1. Due to their high transverse momentum the electrons fail to meet the requirements for a Brillouin beam and have a high reflection probability when propagating into the magnetic field gradient of the solenoid. The reflected electrons may return to the electron gun and hit the anode electrode. Because single-volume simulations of the complete TestEBIS is not applicable, the volume division discussed in Section 4.2 is used. Fig. 6.2.1 shows the division of the beam line from the electron gun to the solenoid into smaller, locally optimized sub-volumes. TestEBIS was simulated with the same potentials as applied during the commissioning tests. In addition two possible electron gun modifications were evaluated: a sleeved cathode, which has a

non-emitting ring covering the lateral cathode surface, and an additional potential applied to the Wehnelt electrode.

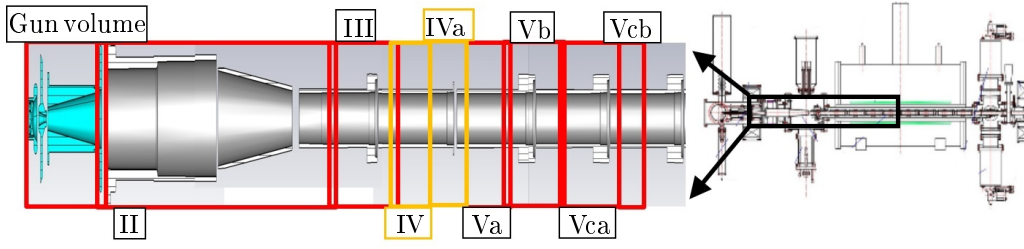
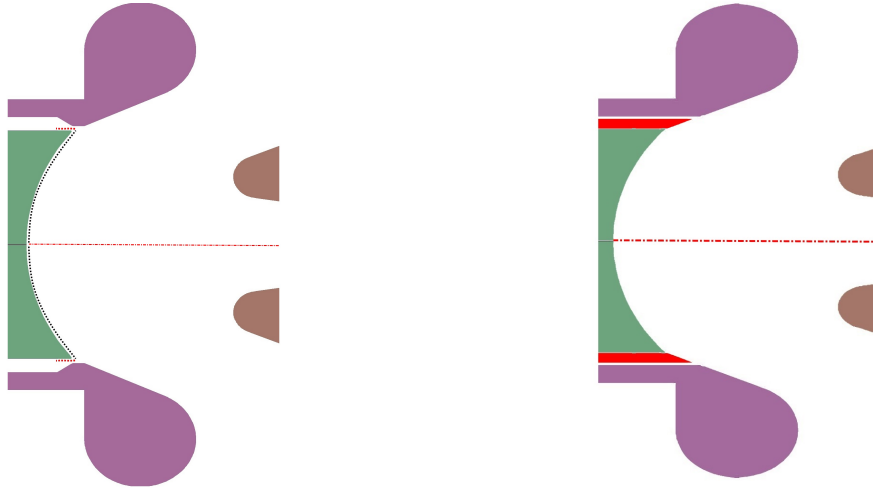


Figure 6.2.1: Division of the total volume into nine sub-volumes. In order to decrease the calculation time, sub-volumes IV and V were divided into two and four sub-volumes, respectively.

### 6.2.1 Side-emission of the cathode

When performing electron beam tracing, usually only the front surface of the cathode is set as electron emitting. To evaluate side-emission, the emission surface was extended to the lateral surface. Fig. 6.2.2(a) shows the emission surface for the default geometry. A suggested solution considering a sleeved cathode is shown in Fig. 6.2.2(b).



(a) Default geometry with the cathode in green, Wehnelt electrode in pink and anode in brown. The emission surface is indicated by a dotted line in front of the cathode. The emission area for SEE are indicated by a red dotted line.

(b) Modified geometry with the cathode in green, surrounded by a non-emitting sleeve in red.

Figure 6.2.2: Modification of the default geometry after introduction of a sleeved cathode. The Wehnelt hole was extended in order to provide space for the cathode sleeve. The front surface of the sleeve is the geometric extension of the Wehnelt electrode.

For more accurate results, the sharp cathode edge connecting the front and lateral surfaces was smoothed out by an arc with a radius of 0.1 mm. The gun volume at the cathode is meshed with a radial and axial precision of  $\Delta_{mr} = \Delta_{mz} = 30 \mu\text{m}$ , which is higher than the suggested values stated in Tab. 4.2.1 of  $\Delta_{mr} = 70 \mu\text{m}$  and  $\Delta_{mz} = 150 \mu\text{m}$ . This results in 375 emission nodes on the front and lateral surfaces of the cathode. Due to the round edge at the cathode tip a clear division into front and side-emitted current at the cathode tip was difficult to establish and therefore imprecise. To evaluate the side-emitted current all current from emission nodes with number  $> 342$ , positioned at the end of the round edge connecting to the lateral surface, was counted as side-emitted. The magnetic field generated by the gun coil was calculated according to operational values with 85 A at 420 turns in the solenoid, which equals a field strength of 0.215 T in front of the gun. The current of the main solenoid was adjusted to 3.5 T inside the solenoid. The electron gun was operated at an extraction potential of  $U_{\text{ex}} = 15.5 \text{ kV}$ . These settings were kept during all simulations in this section unless explicitly stated otherwise.

#### 6.2.1.1 The default geometry

Calculations of the default geometry, see Fig. 6.2.3, show that from the total emitted current of  $I_e = 1.8 \text{ A}$ , the side-emitted current is  $I_{\text{SEE}} = 44.1 \text{ mA}$ , corresponding to 2.6% of the total current. This fraction of the total emitted current is located in the beam halo orbiting around the main electron beam. These trajectories are not matched by the matching magnetic field, which increases the  $\Delta r_e$ -value of the beam envelope of the front-emitted electron beam. To evaluate if the Brillouin-like beam will be accepted by the solenoid, the trajectories were simulated until they reached a region with a magnetic field of 3.5 T. The propagation into the main solenoid will be investigated in detail in Section 6.2.2 with different particle tracing resolutions.

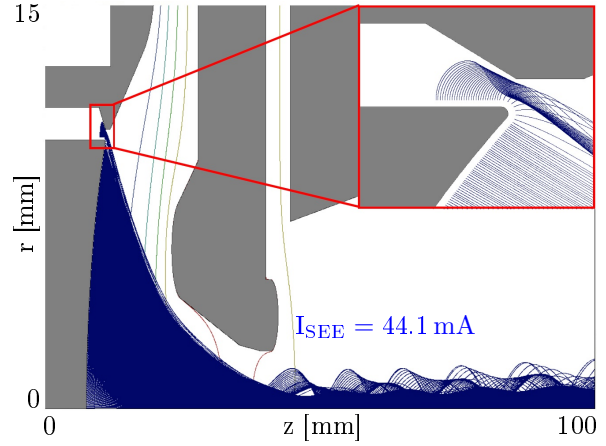


Figure 6.2.3: Calculated trajectories of the electron beam during the gun commissioning test (default geometry).

#### 6.2.1.2 The sleeved cathode

The first suggested modification for reducing the side-emitted current is a sleeved cathode, shown in Fig. 6.2.4. The gap between the sleeve and cathode is 0.1 mm. The sleeve itself has a thickness of 0.8 mm and the gap between the sleeve and the Wehnelt is 0.3 mm. The sleeve is at the cathode potential. Simulations with the sleeved geometry result in a total emission current of

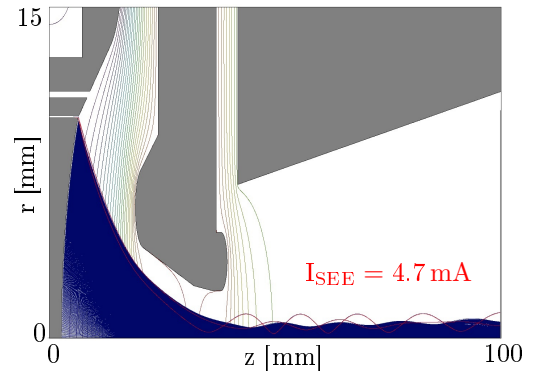


Figure 6.2.4: Electron beam with side-emitted electrons in red (sleeved cathode).

$I_e = 1.8 \text{ A}$ , where the side-emitted current is  $I_{\text{SEE}} = 4.7 \text{ mA}$  corresponding to a reduction of 90% compared to the default geometry. The simulation shows that the inserted sleeve sufficiently suppresses the side-emitted current. No trajectories with exceptionally high transverse momentum could be observed in any simulations using a sleeved geometry.

### 6.2.1.3 The default geometry with applied Wehnelt potential

Applying a potential on the Wehnelt electrode, lower than the cathode potential, is the second suggested method to suppress side-emitted electrons. A correct ratio between the potentials of the Wehnelt electrode, cathode and anode is important for suppressing SEE as well as improving the beam injection into the magnetic field. The gun geometry is designed so that the applied electric field between cathode and anode is perpendicular with respect to the front surface of the cathode and creates a focus in the anode hole. The correct Wehnelt potential suppresses the electron emission only on the lateral surface with minimal distortion of electrons emitted from the front surface close to the cathode edge. The emission of the HEC<sup>2</sup> gun operating with optimal Wehnelt potential is shown in Fig. 6.2.5. Here  $U_w = -20 \text{ V}$  results in an optimal ratio between SEE suppression and non-distorted front emission. 5.4 mA are carried by the remaining SEE trajectories in the halo. This corresponds to a reduction of 92% compared to the default geometry. Beam tracing calculations with varied extraction potentials of the HEC<sup>2</sup> gun, see Table 6.2.1, show that the optimum Wehnelt potential suppressing SEE with minimum distortion of the main beam should be scaled as  $U_w[\text{V}] = 2.78 - 1.46U_{\text{ex}}[\text{kV}]$ .

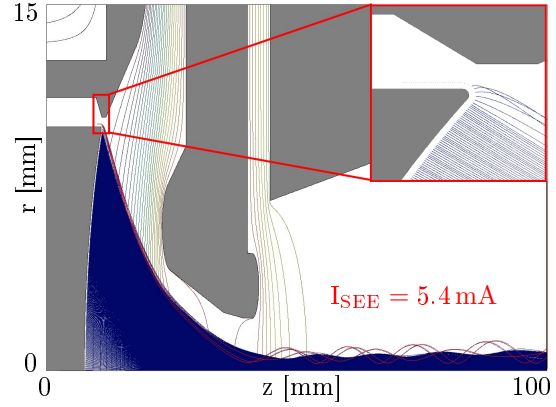


Figure 6.2.5: Generated electron beam with  $U_w = -20 \text{ V}$  (default geometry). The SEE are shown as red trajectories orbiting the front-emitted electron beam.

Table 6.2.1: Side-emitted current as function of the extraction potential.

| $U_{\text{ex}}[\text{kV}]$ | $U_w[\text{V}]$ | $I_e[\text{A}]$ | $I_{\text{SEE}}[\text{mA}]$ |
|----------------------------|-----------------|-----------------|-----------------------------|
| 15.5                       | -20             | 1.8             | 5.4                         |
| 20                         | -26             | 2.6             | 7.8                         |
| 25                         | -33             | 3.6             | 10.5                        |
| 30                         | -40             | 4.8             | 13.5                        |
| 35                         | -48             | 6.0             | 16.0                        |
| 40                         | -55             | 7.3             | 19.5                        |

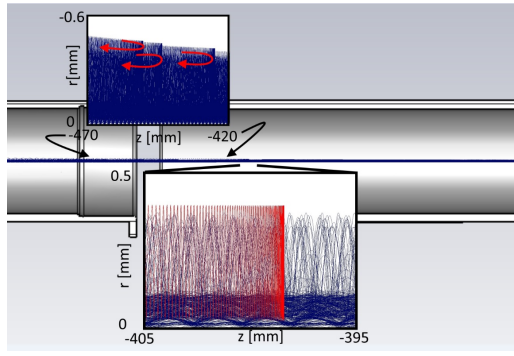
#### 6.2.1.4 Summary of the SEE-reduction methods

Both methods of reducing the loss current resulted in a similar degree of SEE suppression. In each case a significant reduction of side-emitted current from 44 mA down to 5 mA was achieved for an extraction voltage of 15.5 kV. In addition both approaches result in lower transverse momentum of the electrons orbiting the front-emitted electron beam compared to the default geometry. The usage of a sleeved cathode is more difficult to realize compared to a biased Wehnelt. A risk is the possibility of chemical interaction between the sleeve and cathode material, which might counteract the purpose of the sleeve. When considering the standardized usage of a Wehnelt potential to suppress SEE during the operation it is recommended to reduce the gap between Wehnelt electrode and cathode even more than in the investigated geometry in order to further improve the ratio between suppression and distortion.

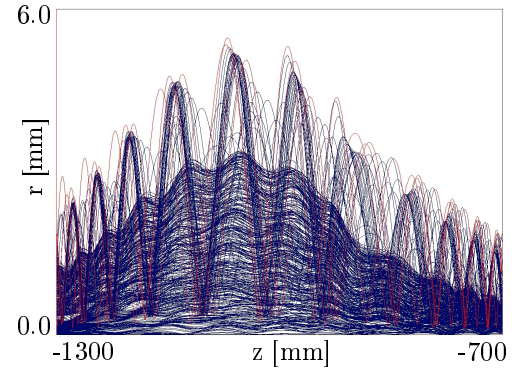
#### 6.2.2 Reflection of the side-emitted current

The electron beams of the three setups previously discussed were traced into the main solenoid in order to investigate the occurrence of reflected current. Tracing simulations with electron beams emitted from the sleeved cathode and the default cathode with applied optimal Wehnelt potential showed a full acceptance by the solenoid. Therefore this section focuses on the electron beam emitted from the default HEC<sup>2</sup> gun with the potentials used during the commissioning. To investigate SEE, the particle microscope, introduced in Section 4.3.3, was applied to multiply the outermost 36 emitted particles with a factor of 100. The time steps were decreased by a factor of 10 to  $5 \cdot 10^{-15}$  sec, reducing the energy discrepancy of the traced reflected current to a level of  $\Delta E/E < 0.02\%$ . The simulation results in a reflected current of  $I_{\text{refl}} = 2.7$  mA, which is carried by 296 trajectories. Fig. 6.2.6(a) shows a zoom into the drift tubes where particular trajectories are reflected. These reflected trajectories were back-traced to their point of termination at the electron gun. Fig. 6.2.6(b) shows the back-traced reflected electrons overlaid on the electron beam propagating towards the solenoid. These reflected electrons have the same amplitude and a similar phase as the side-emitted electrons orbiting the primary electron beam in the main solenoid. The axial positions of reflection and the corresponding local magnetic field were read out. The evaluation of the trajectories in the different sub-volumes results in a distribution of accepted and reflected particles and their points of reflection, see Fig. 6.2.7. Here the magnetic field is overlaid to the sketch of the TestEBIS. The **red** dots indicate the magnetic field at the axial position of reflection. According to the simulations, SEE are reflected starting from  $\approx 10$  cm inside the solenoid where the magnetic field is  $B = 1.8$  T until they pass the maximal field strength of  $B = 3.5$  T as shown in detail in Fig. 6.2.8(a). The total reflected current as a function of the axial position is shown in Fig. 6.2.8(b).

To determine if only SEE contribute to the reflected current, the phase space of the electron beam acquired in front of the HEC<sup>2</sup> gun was resolved to SEE, front-emitted and reflected electrons. The resultant phase space is shown in Fig. 6.2.9(a). The front-emitted particle ensemble is represented by black squares. The dashed circles guide the eye to distinguish between the core electron beam and the beam halo. The particles that were introduced by the particle microscope are shown as **red** squares. They connect the phase space between the primary particles. The reflected particles are shown in **blue**. The reflected electrons are traced back from their point of reflection to the electron gun volume as shown in Fig. 6.2.9(b). The reflected



(a) Position of the reflected trajectories, which are indicated by **red** arrows (upper subfigure) or by a red trajectory (lower subfigure).



(b) Back-traced electrons drawn in **red** overlaid on the electron beam in the low magnetic field area between electron gun and main solenoid.

Figure 6.2.6: Reflection of SEE at the magnetic field gradient. The position of reflection is 10cm inside the main solenoid. The reflected electrons have the same orbit as the incoming orbiting electrons. The axial coordinates are here the distances to the center of the solenoid.

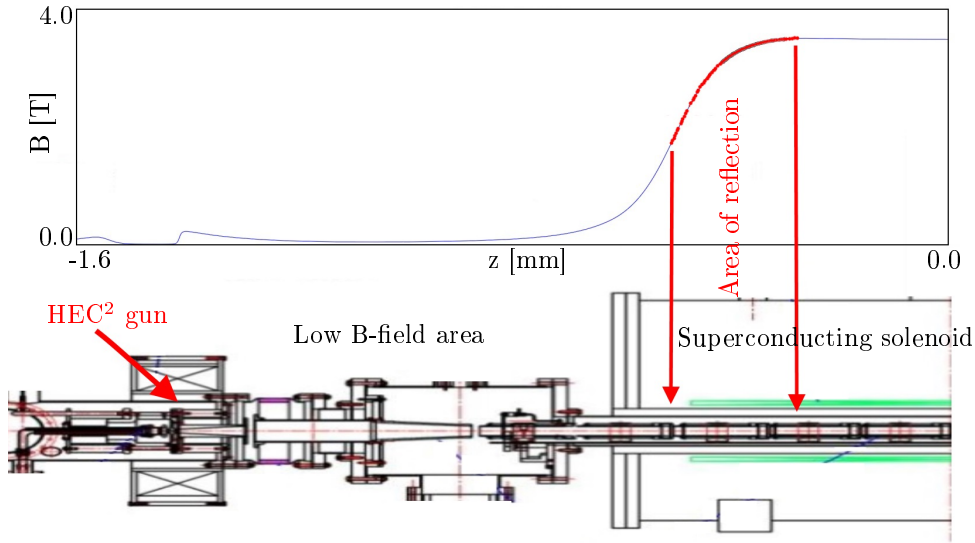


Figure 6.2.7: Magnetic field strength at the point of reflection, lower figure shows the location of reflection at the TestEBIS assembly.

electron beam has a wider radius than the primary beam. 1.5 mA out of the total reflected current of 5 mA is directly deposited on the anode. Trajectories able to pass the anode hole are reflected in front of the cathode and Wehnelt electrode. In the simulation a current deposition on the cathode of 0.05 mA and on the Wehnelt of 0.1  $\mu$ A is observed. This deposited current is non-physical and occurs due to numerical energy discrepancy, which can be reduced by smaller tracing time-steps. Therefore the current observed on Wehnelt and cathode is considered to be deposited on the anode. The particles reflected from the cathode or Wehnelt either terminate on the anode electrode or pass the anode again and propagate towards the solenoid. The fraction of current reflected from the electron gun is  $\approx 10\% = 0.2$  mA of the current initially reflected at the magnetic field gradient. The remaining 90 % of the



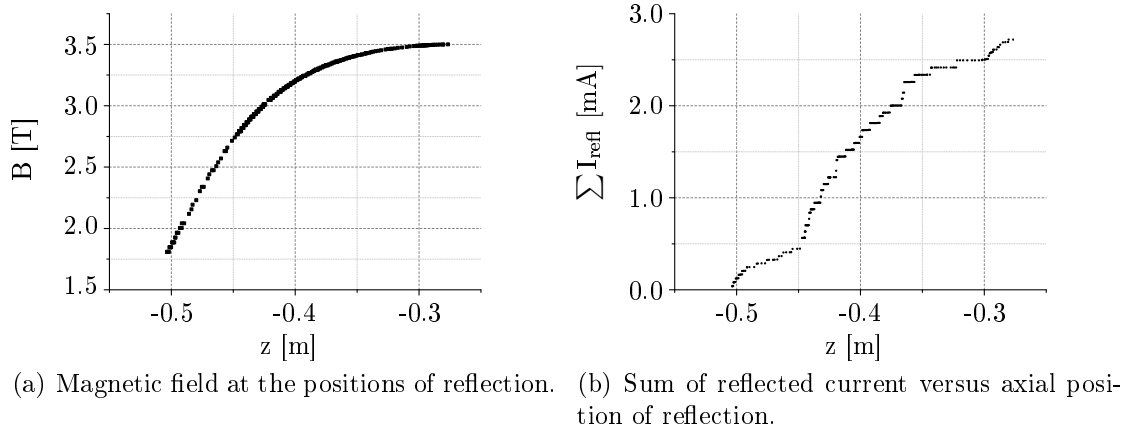


Figure 6.2.8: Simulated particle reflection during the TestEBIS-commissioning experiment of the default HEC<sup>2</sup> gun.

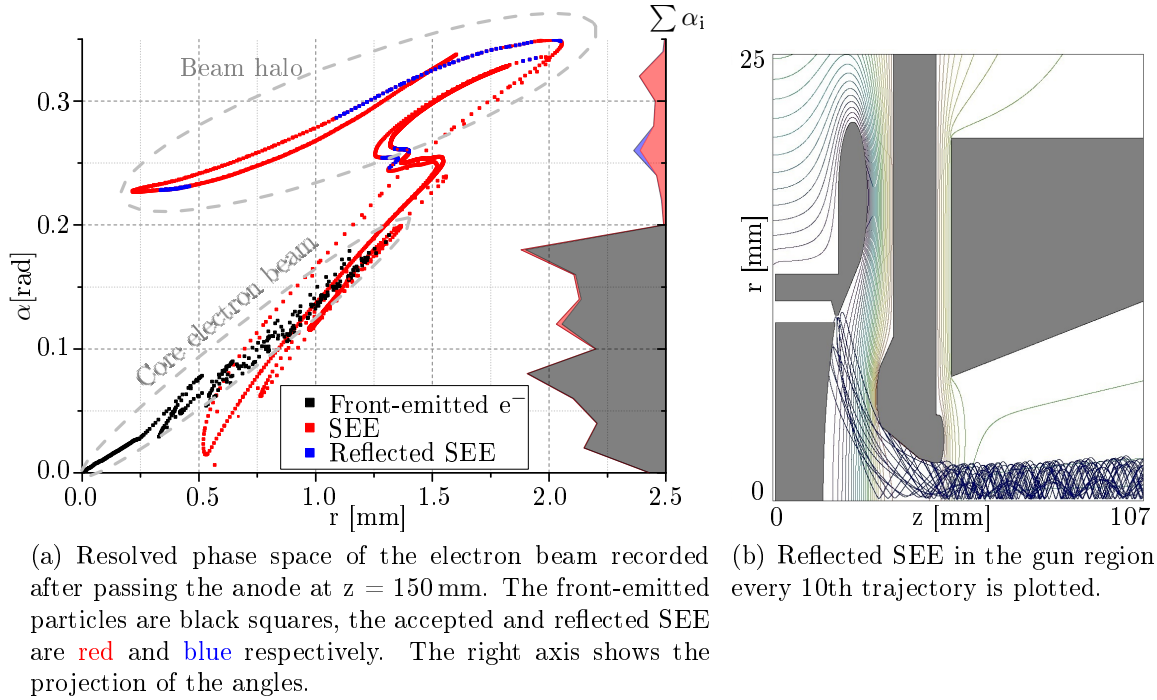


Figure 6.2.9: Reflected SEE shown in the resolved phase space of the electron beam propagating towards the solenoid and as reflected particles at the electron gun.

reflected current is deposited on the anode. Of the 0.2 mA of re-emitted electrons, 0.1 mA are finally accepted by the solenoid. The reflected electrons propagate again towards the electron gun, equally distributed as in the first iteration. It can be assumed that 90 % of the total current reflected at the magnetic field gradient is deposited at the anode.

### 6.2.3 Results

Simulations of a perfectly aligned HEC<sup>2</sup> gun operating with the voltages applied during the commissioning tests show that the cathode emits from the lateral surface as well as from the front surface. These SEE form a halo around the front-emitted electron beam and are injected into the matching magnetic field under sub-optimal conditions. When propagating into the solenoid a fraction of the SEE are reflected back towards the electron gun and cause loss current at the anode electrode, which was confirmed by measurements during the commissioning phase. A gun assembly which is not perfectly aligned radially leads to a decreased beam quality at the injection point into the magnetic field. The electron beam with the reduced beam quality has a higher probability of reflection at the magnetic field gradient. Further simulations show that the beam halo in the HEC<sup>2</sup> gun can be reduced by applying an additional potential to the Wehnelt electrode. The electron beam from this simulation shows full acceptance by the solenoid which is also the case for simulations with the sleeved cathode.

## 6.3 Optimization of the TestEBIS collector

The electron beam from the HEC<sup>2</sup> gun terminates in the collector, shown in Fig. 6.3.1. In this rendered model the horizontal water-cooled collector surface is shown in **red** and the non-cooled front plate is shown in **green**. Simulating the electron beam from the HEC<sup>2</sup> gun over a distance of 3 m to the collector accumulates the numerical error. To reduce the numerical error for the investigating beam propagation inside the collector, the electron beam is translated. First the electron beam is simulated from the cathode to an axial position with a magnetic field similar to the magnetic field in front of the collector. There, the properties of the electron beam are recorded. The electron beam is translated and continues propagating with the recorded properties as starting conditions at a position in front of the collector. A translated electron beam entering the TestEBIS collector is shown in Fig. 6.3.2. The beam has to pass the suppressor electrode before entering the collector. The ion extractor and ion lens guide the ion pulses when being injected and ejected. The electron beam starts widening due to the space charge repulsion at the absence of a magnetic field.

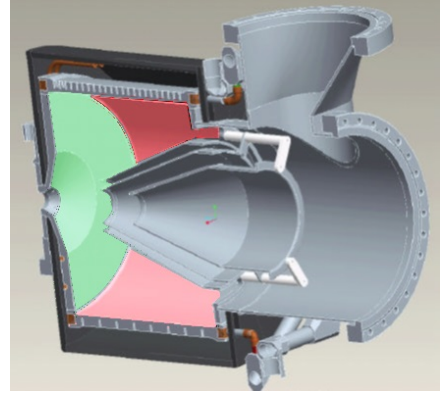


Figure 6.3.1: Rendered geometry of the collector alignment [Pikin et al. 2006], **red** area indicates the horizontal water-cooled area; the **green** area indicates the non-cooled vertical area (front plate).

This collector is designed to operate at a peak power of 300 kW for a 20 A beam. The distribution of power according to the collector design is shown in Fig. 6.3.3(a) for the horizontal collector area and in Fig. 6.3.3(b) for the vertical front area. This power distribution will be the benchmark distribution against which the simulation results of a 10 A DC electron beam will be compared and evaluated.

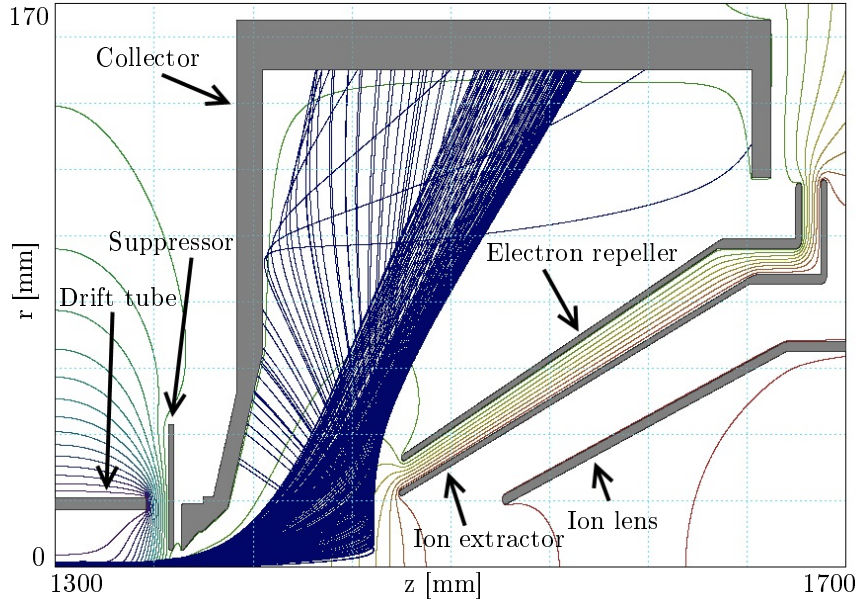
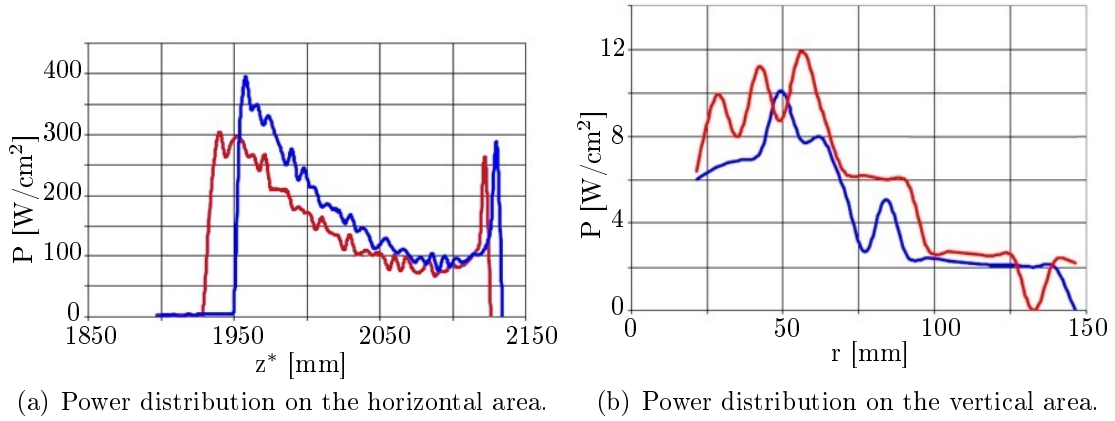


Figure 6.3.2: Beam propagation in the collector geometry.



(a) Power distribution on the horizontal area. (b) Power distribution on the vertical area.

Figure 6.3.3: Power distribution on the horizontal and vertical plate of the collector design for an incident electron beam  $I_e = 20.6$  A. The applied potentials are  $U_{\text{coll}} = 15$  kV and  $U_{\text{rep}} = 17$  kV. Here the red distribution results from an electron beam with a radius  $r_e = 6.2$  mm when entering the collector, blue results from an electron beam with a radius of  $r_e = 4.7$  mm, taken from [Pikin et al. 2006].

The electron beam, shown in Fig. 6.3.2, is calculated without considering any processes other than direct deposition. In order to model a more realistic electron distribution the particle microscope and the BSE model is applied. An increase of the particle resolution of the PE near the beam axis reveals particle reflection due to the electric field from the repeller. Those elastically reflected PE, called ERPE, can escape the collector, reach the anode and cause loss current. BSE can redistribute power from the water-cooled collector surface to non-cooled parts, such as the electron repeller, or escape the collector and deposit the power onto the anode. The reduction of these effects is a multidimensional optimization task. Only the most promising potential configurations are shown and discussed in the next sections.

### 6.3.1 Investigations of ERPE inside the collector

To investigate the ERPE current, electron beams were traced at different configurations of the potentials as shown for selected potential configurations in Table 6.3.1. Within the simulation series 1 - 4 the potential of the electron repeller is varied, which influences the deflection of the widening electron beam. Within series f -h the ion extractor potential is varied, which influences the electric field distribution on axis inside the collector. This changes the degree of deflection of the incident electron beam. Trajectories which leave the collector volume and end at the starting point of tracing at the left volume boundary are considered to be escaped current,  $I_{\text{ERPE}}$ . The innermost electrons in the electron beam are most likely to experience elastic reflection. The particle microscope increases the number of particles with a starting position closer to the axis ( $r \leq 0.1 \text{ mm}$ ) by a factor of 50-100.

Table 6.3.1: Applied voltages on the collector, the repeller, the extractor and the ion lens relative to the anode voltage ( $U_{\text{applied}} = 49.2 \text{ kV} - U_{\text{tabled}}$ ) for different simulation series.

| Conf. | $U_{\text{coll}}[\text{kV}]$ | $U_{\text{rep}}[\text{kV}]$ | $U_{\text{Ext}}[\text{kV}]$ | $U_{\text{Lens}}[\text{kV}]$ | $I_{\text{ERPE}}[\text{mA}]$ |
|-------|------------------------------|-----------------------------|-----------------------------|------------------------------|------------------------------|
| 1     | 11.8                         | 9.7                         | -4                          | -10.8                        | 3.14                         |
| 2     | 11.8                         | 7.7                         | -4                          | -10.8                        | 2.71                         |
| 3     | 11.8                         | 6.7                         | -4                          | -10.8                        | 2.51                         |
| 4     | 11.8                         | 5.7                         | -4                          | -10.8                        | 2.51                         |
| f     | 11.8                         | 9.7                         | -9.8                        | -10.8                        | 0.83                         |
| g     | 11.8                         | 9.7                         | -10.8                       | -15.8                        | 0.97                         |
| h     | 11.8                         | 9.7                         | -11.8                       | -15.8                        | 0.83                         |

Investigating the particular potential distributions inside the collector results in a current on the left boundary of at least  $I_{\text{ERPE}} = 0.83 \text{ mA}$ , which cannot be suppressed in any of the investigated potential configurations. Fig. 6.3.4(a) and (c) show the propagation of the reflected particles in potential distribution 1 resulting in the highest escaping current. The particles escaping the collector are shown in **red**. As indicated, the particles closest to the electron beam axis escape the collector orbiting the incident PE beam. The lowest  $I_{\text{ERPE}}$  is achieved in distribution f, shown in Fig. 6.3.4(b) and (d). However, this might not be the global optimum since the power distribution and BSE also need to be considered. The current deposited on the suppressor is not considered for optimization.

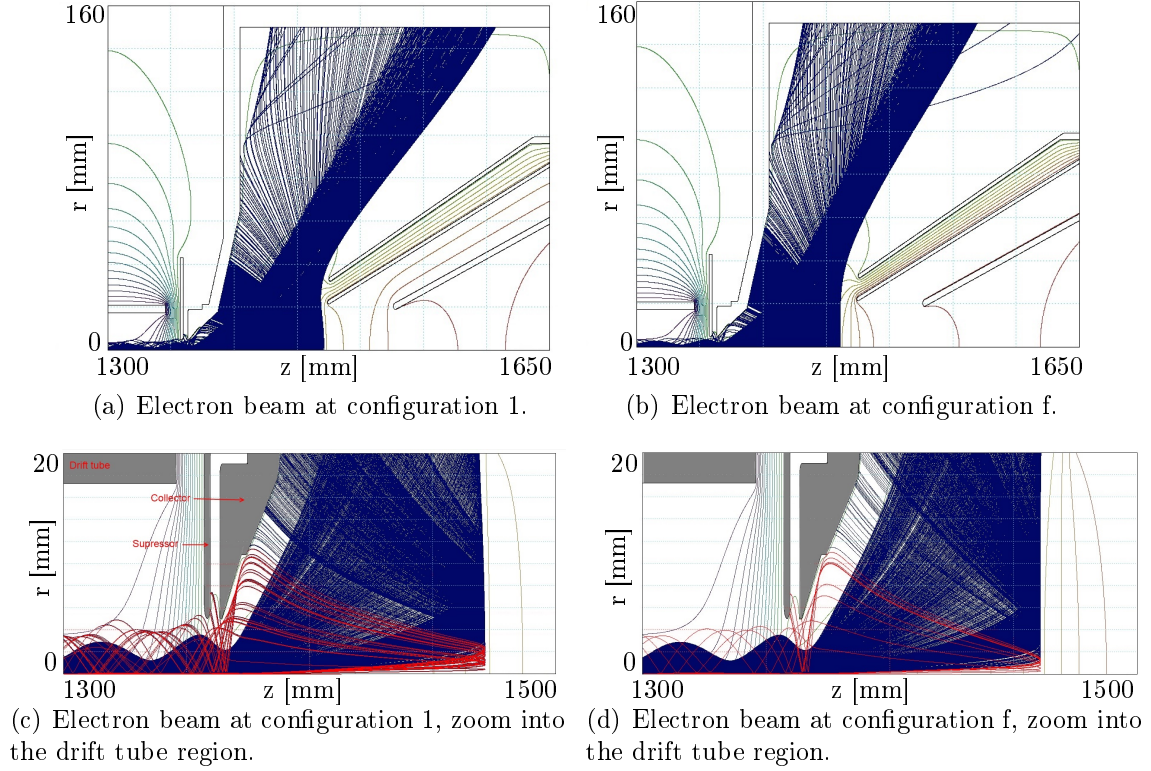


Figure 6.3.4: Electron beam trajectories in the collector region for different settings of the potentials. The particle microscope was applied to the innermost electrons.

The electrons with high transverse momentum leave the optimized collector (configuration f) and propagate towards the solenoid as a halo around the PE beam as shown in Fig. 6.3.5. The ERPE are shown as **red** trajectories overlaid on PE propagating towards the collector. The plot on the upper part of the figure shows the magnetic field strength. Similarly to the SEE reflection discussed in the previous section, the ERPE reflect at the magnetic field gradient of the solenoid at the collector side. The reflected particles propagate back into the collector. These electrons are absorbed on the collector surface as they are orbiting far off the beam axis. It is shown that a solenoid generating a sufficient magnetic field protects the electron gun from ERPE escaping the collector. If the magnetic field in the trapping region is too low for reflecting the ERPE, an artificial misalignment of the collector increases the transverse momentum of the escaping electrons re-entering the beam line.

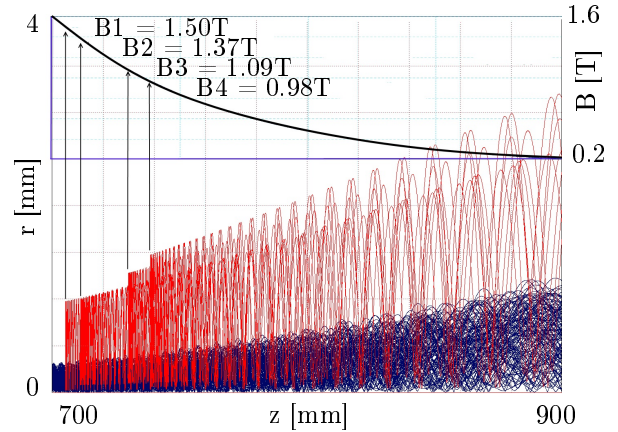
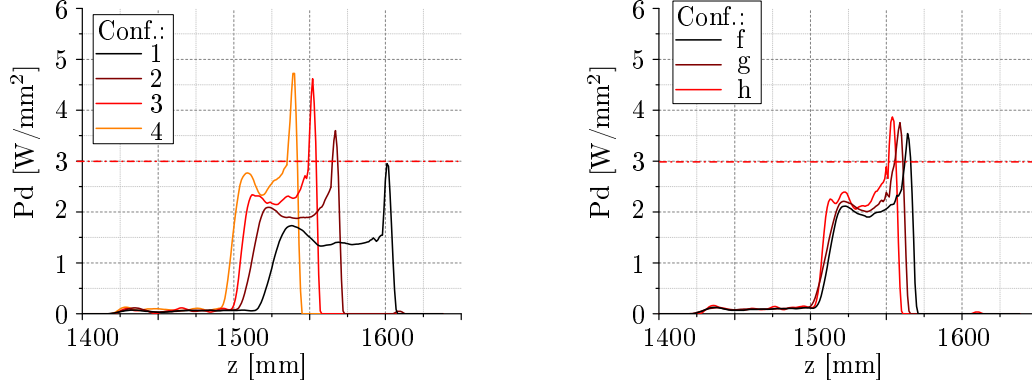


Figure 6.3.5: Trajectories of the ERPE in **red** overlaid with the PE beam in **blue**. The line at the top shows the magnetic field and the point of reflection.

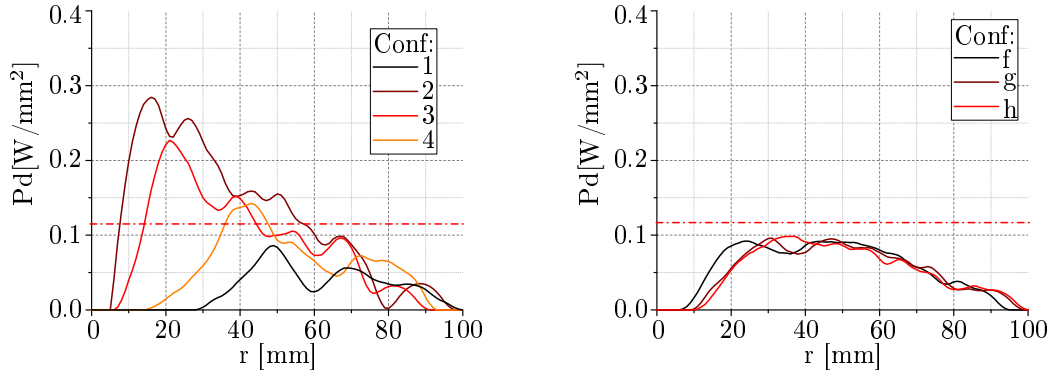
### 6.3.2 Investigations of the power deposition inside the collector

The power directly deposited on the water-cooled surface is investigated by acquiring the impact coordinates of the simulated trajectories. As a result one can extract the power density  $Pd[W/mm^2]$ , which is shown for both series in Fig. 6.3.6(a) and (b). The peaks in Fig. 6.3.6(a) are a result of beam folding due to electron beam deflections by the electron repeller. A reduction of power deposition on the front plate of the collector at potential distribution f in the collector could be achieved, which becomes apparent when comparing the power density on the front plate of the collector shown in Fig. 6.3.3(b) with 6.3.7. In [Pikin et al. 2006] it is indicated that the design value of deposited power at the vertical front plate is many orders of magnitude higher than the resulting amount in the simulations. Therefore the deposited power from the primary beam at the front plate is omitted as a limiting factor.



(a) Deposited power at the horizontal collector surface while varying the electron repeller potential. (b) Deposited power at the horizontal collector surface while varying the potential at the ion extractor.

Figure 6.3.6: Distribution of the deposited power on the horizontal collector area. The dashed red line indicates the peak height in 6.3.3(a).



(a) Deposited power at the horizontal collector surface while varying the electron repeller potential. (b) Deposited power at the horizontal collector surface while varying the ion extractor potential.

Figure 6.3.7: Distribution of the deposited power on the vertical collector area. The red line indicates the peak height in Fig. 6.3.3(b).

A small potential difference between electron repeller and collector delocalize the electron beam on the water cooled surface while a higher potential difference between repeller and ion extractor minimizes  $I_{ERPE}$ . Voltage configuration f provided the most homogeneous power deposition distribution achieved in the simulations.



### 6.3.3 Investigations of the redistribution of deposited power by BSE

Including BSE changes the final distribution of the power deposition inside the collector. A simulation of an electron beam in a collector with the potential configuration f and the resulting BSE propagation is shown in Fig. 6.3.8. The PE is shown as **blue** and the resulting BSE distribution as **red** trajectories. The lower figures show the respective power depositions at the horizontal and vertical plates. As discussed in Section 4.3.4.2, the distribution of kinetic energy of BSE taking off from a copper target has its maximum at  $\approx 80\%$  of the initial energy. The potential difference between the collector and electron repeller in this example is  $\Delta U = 2\text{ kV}$ , which is less than the kinetic energy of the incident PE beam of  $E_0 \approx 11\text{ keV}$ . BSE are therefore capable of reaching the front plate of the collector and the electron repeller.

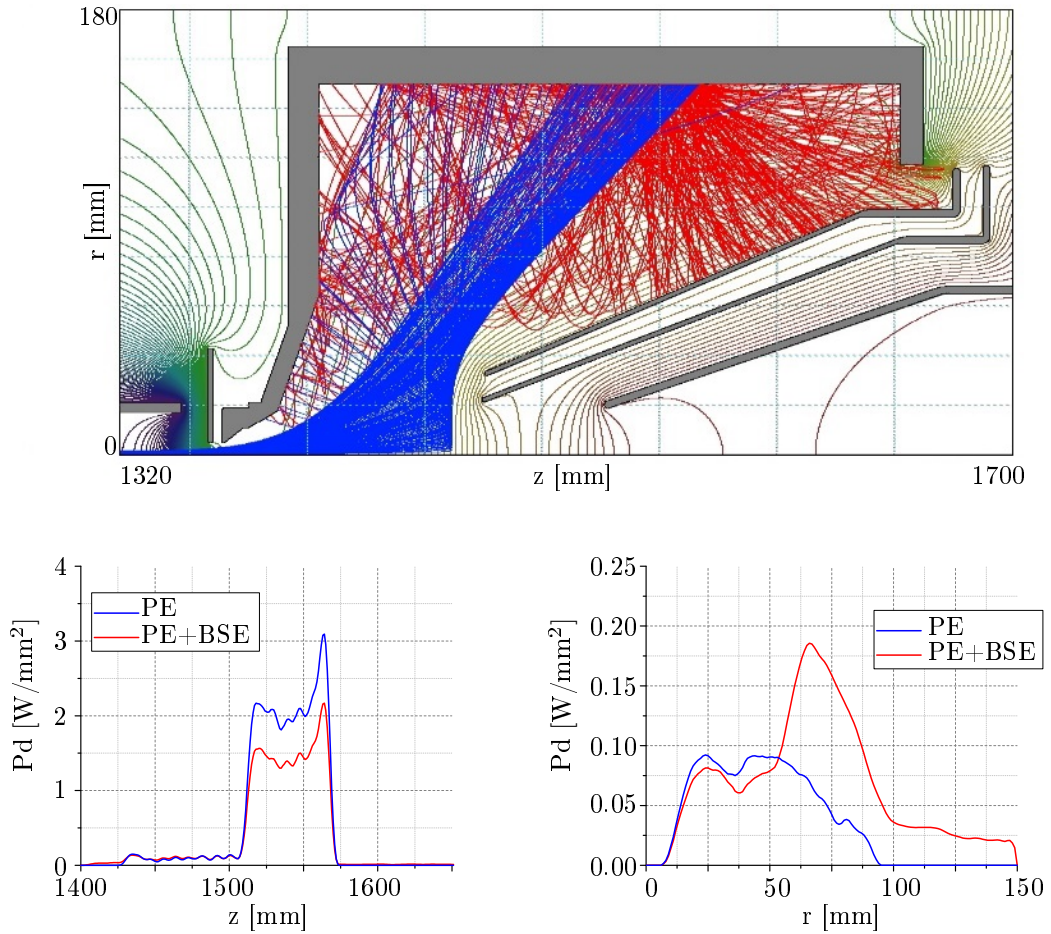


Figure 6.3.8: PE and BSE distribution in potential configuration f. The deposited power density on the horizontal, water cooled plate (bottom left) and the vertical front plate (bottom right).

During simulations BSE redistribute the deposited power from the water-cooled surface to other non-cooled collector parts. In case they terminate on the same surface from which they are emitted, they average out the power distribution. The local power density on the horizontal surface decreases significantly from  $2.0\text{ W/mm}^2$  to  $1.3\text{ W/mm}^2$  when including BSE in the simulation. To quantify the redistribution

Table 6.3.2: Total deposited power on the horizontal and frontal plate for a 10 A x 11 keV electron beam.

| Conf. | Total deposited power [kW] |        |                |        |
|-------|----------------------------|--------|----------------|--------|
|       | horizontal plate           |        | vertical plate |        |
|       | PE                         | PE+BSE | PE             | PE+BSE |
| 1     | 124.7                      | 91.4   | 1.3            | 4.3    |
| 2     | 122.3                      | 92.5   | 3.4            | 6.1    |
| 3     | 123.5                      | 93.8   | 2.6            | 5.7    |
| 4     | 123.9                      | 95.5   | 2.2            | 5.3    |
| f     | 123.9                      | 92.0   | 2.0            | 5.4    |
| g     | 124.0                      | 92.4   | 2.0            | 5.0    |
| h     | 124.0                      | 92.8   | 2.0            | 5.2    |

effect, Table 6.3.2 shows the total deposited power neglecting and considering the power redistribution by BSE on both plates. Because the front plate is at the same potential as the horizontal plate, the power redistribution between those two areas remains constant during the potential variations. In contrast, the repeller is at a different potential than the collector. Therefore the power redistributed from the collector to the electron repeller depends on their potential difference. Table 6.3.3 shows the power deposition as a function of the potential difference between collector and electron repeller. By increasing the potential difference, the amount of BSE able to reach the repeller is reduced. Electrons with insufficient kinetic energy reflect back onto the collector surface and average out the power density.

As discussed in Section 4.3.4.3, the peak of the take-off angle of BSE obeys the reflection law, see Eq. 4.3.7. This leads to the situation in which the majority of the current carried by BSE is transferred to a local area on the repeller electrode. In this example 15 kW will constantly be deposited on this electrode on an axial length of 15 cm. Since the repeller is not cooled one can estimate the temperature gain with Boltzmann's law:

$$T[K] = \sqrt[4]{\frac{P}{5.67 \cdot 10^{-8} \epsilon A}}$$

Here A is the surface area in [m<sup>2</sup>] and P the deposited power in [W]. For  $\epsilon$ , the tabulated constant for steel,  $\epsilon = 0.54$ , is used. This results in a temperature gain of 1800 K as shown in Fig. 6.3.9. To avoid melting the electron repeller, a potential close to the kinetic energy of the PE has to be applied. This leads to a stronger deflection of the electron beam and a higher focusing of the electron beam onto the collector surface resulting in a higher local power density. Furthermore it was ensured by iterative calculations that BSE do not influence the beam propagation of PE. An iteration consists of generating the BSE from the initial PE distribution inside the collector and tracing them. With the resulting space charge field the PE are traced again into the collector.

Table 6.3.3: Deposited power and current at the electron repeller with the temperature gain as function of the potential difference between repeller and collector.

| $\Delta U$ | P[kW] | I[A] | T[K] |
|------------|-------|------|------|
| 2.1        | 14.3  | 2.0  | 1800 |
| 4.1        | 7.2   | 1.3  | 1500 |
| 5.1        | 4.8   | 1.0  | 1400 |
| 6.1        | 2.5   | 0.6  | 1200 |



BSE with a certain take-off angle and energy at the front plate of the collector near the entrance aperture make up a possible additional source for back-traveling electrons. Therefore the BSE were investigated for their ability to escape the collector. In those calculations the output electric and magnetic fields of the geometry, which contain the space charge field of the previously calculated primary electron beams, were used as initial fields. In all simulations BSE were deflected back onto the collector owing to the space charge field of the incident PE beam. PE terminating on the entrance aperture of the collector generate BSE with a take-off angle allowing them to re-enter the trapping region or reach the suppressor. Due to the incident angle of reflected primary electrons with respect to the surface only a small area, namely the entrance aperture of the collector, is considered to create BSE which might be able to enter the source region or terminate on the suppressor. However, during simulations using the particle microscope no PE could be observed terminating at the entrance aperture. BSE propagating towards the electron gun will be reflected back into the collector by the magnetic field of the solenoid.

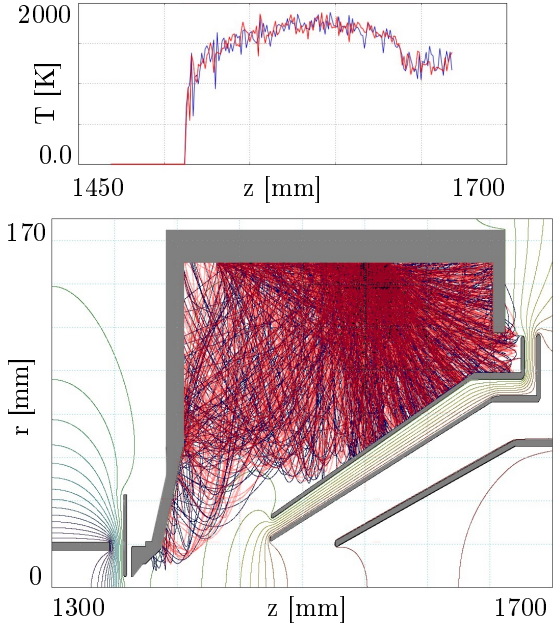


Figure 6.3.9: Resulting BSE trajectories and temperature at the repeller electrode as a result of two simulations with equal settings.

### 6.3.4 Suggested collector geometry

Several operation limiting issues were identified during the beam calculations of a 10 A DC electron beam. Due to the collector geometry a non-negligible amount of BSE generated by the primary electron beam reaches the non-cooled repeller electrode and overheats the repeller electrode. Applying a sufficient potential difference between electron collector and electron repeller reduces the deposited power but leads to a higher focusing of the electron beam deposition on the collector surface. The locally increased power density may lead to overheating. To delocalize the power deposition an improved geometry is suggested, shown in Fig. 6.3.11(b). Shortened electrodes with a steeper angle provide more space to the electron beam for unfolding. Furthermore, higher potentials can be applied to the electron repeller. This prevents BSE from overheating the repeller. Shortening the electrodes results in a wider spacial distribution of the beam on the horizontal surface and therefore in lower power density. The average power density of roughly  $P_d \approx 1.5 \text{ W/mm}^2$  can be reduced to  $\approx 0.8 \text{ W/mm}^2$

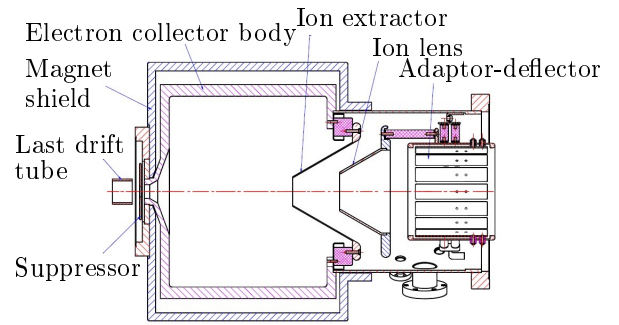


Figure 6.3.10: Collector of the RHIC-EBIS, taken from [Pikin et al. 2012].

in the proposed geometric configuration, see Fig. 6.3.12(a) and (b). The simulation of the collector geometry is a proof of principle that can be further optimized. The beam folding and over-bending due to insufficient deflection remains. A collector of a geometry similar to the suggested one is installed at the RHIC-EBIS, as shown in Fig. 6.3.10. When operating the HEC<sup>2</sup> with a 10 A electron beam, it is necessary to exchange the TestEBIS collector with the RHIC-EBIS collector.

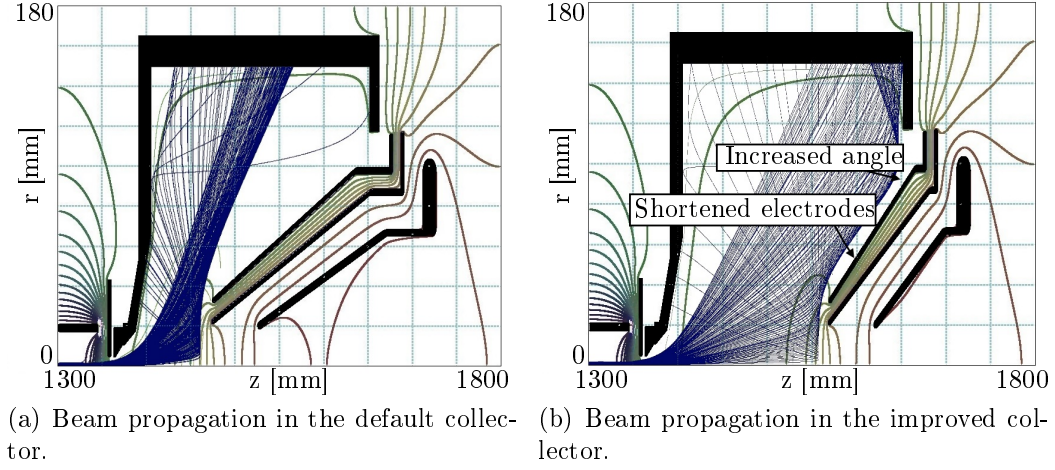


Figure 6.3.11: Electron beam propagation in the default geometry and the suggested geometry.

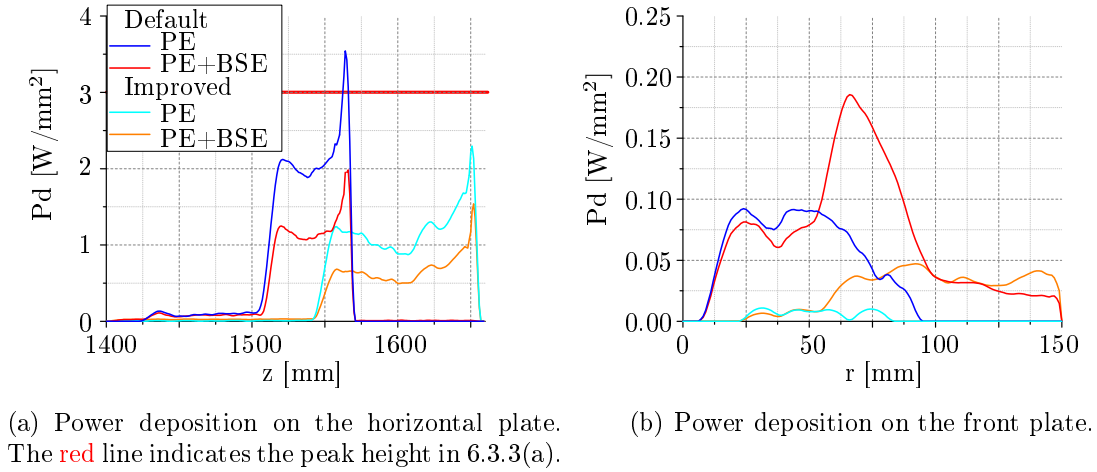


Figure 6.3.12: Power deposition considering and neglecting BSE in the default collector geometry of TestEBIS and the improved geometry of this collector.

## 6.4 Summary of the HEC<sup>2</sup>-simulation results

The origin of the loss current at the anode of the HEC<sup>2</sup> gun and the feasibility of using the TestEBIS collector with HEC<sup>2</sup> at 10 A and 49 kV were investigated. Beam tracing simulations confirm that SEE are reflected at the magnetic field gradient being the source of the loss current. If they do not terminate at the anode electrode, they enter the gun volume and are reflected by the Wehnelt electrode or cathode. After reflection, they either terminate on the anode or propagate towards the solenoid and the process repeats. It could be shown that a current orbiting around the primary electron beam oscillates between solenoid and electron gun. In addition it was shown that by the use of an optimal Wehnelt potential or a sleeved cathode the SEE could be reduced so that the total electron beam was accepted by a magnetic field of 3.5 T.

It was investigated if the TestEBIS collector is capable of absorbing the electron beam in the case that the current from the HEC<sup>2</sup> gun reaches its design value. ERPE will escape from the collector region for any potential combination of the collector electrodes. These ERPE are reflected by the magnetic field and finally terminate inside the collector. The default collector of TestEBIS is not suitable for absorbing an electron beam of 10 A because the power distribution on the collector surface is not sufficiently well distributed. Investigating the power deposition while considering BSE shows that  $\approx 25\%$  of the current of the incident electron beam is deposited on the electron repeller. This current depends on the potential difference between collector and electron repeller. If the potential difference is adjusted so that the kinetic energy of the BSE is not sufficient to reach the electrode, the PE beam is deflected more strongly backwards resulting in a more focused beam deposition on the horizontal surface of the collector. The resulting locally higher power density due to the focused beam can introduce thermal damage. The proposed collector design with shortened and tilted electrodes, resemble the RHIC collector geometry that withstand operation of HEC<sup>2</sup> at 10 A.

## 7 Design of MEDeGUN

With the knowledge acquired in the design and commissioning of the HEC<sup>2</sup> gun, described in Chapter 6, a smaller Brillouin electron gun is designed to feed an EBIS for medical purposes optimized for breeding 6+ carbon ions. The electron gun described in this chapter is named MEDeGUN. For short breeding times, a current density of  $5 \text{ kA/cm}^2$  is needed in the trapping region ( $B = 5 \text{ T}$ ) with a gun perveance of  $1.0 \mu\text{A/V}^{1.5}$ . MEDeGUN, operating with a 2 T solenoid in the test phase, should be able to generate  $10^9 \text{ C}^{6+}$  per pulse at a frequency of 180 Hz. After successful commissioning of the MEDeGUN the 2 T solenoid will be substituted with a 5 T solenoid, where the MEDeGUN should be able to operate at a breeding rate of 400 Hz in order to be compatible with a special type of medical accelerators, the all-linac type.

### 7.1 Design

The MEDeGUN design is based on the geometry from [Baryshev et al. 1994], shown in Fig. 7.1.1. The so-called Magnicon electron gun promises an electron beam with an area compression of 1500:1 between cathode and focus point at a perveance of  $0.83 \mu\text{A/V}^{1.5}$ .

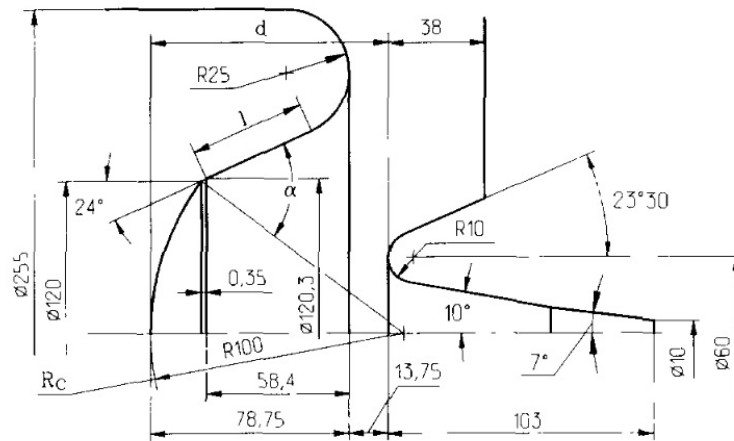


Figure 7.1.1: Geometry and dimensions in [mm] of the Magnicon electron gun [Baryshev et al. 1994].

The MEDeGUN geometry is modified, see Fig. 7.1.2, in order to improve the beam quality of the Magnicon design. Due to the focusing shape of the electric field between cathode and anode, the cathode emits with a radially inhomogeneous current

density, see emission distribution for 1.5 kV in Fig. 4.3.2(a). When the beam is compressed the current-density inhomogeneity will magnify as reported and measured in [Brewer 1959]. MEDeGUN is optimized for providing the lowest current-density variation without a significant reduction of the compression ratio. In order to have lower electrostatic compression the angle of the Wehnelt is increased, the radius of the anode hole is reduced and the anode-cathode distance is shortened. These minor modifications significantly increase the perveance.

According to Herrmann's formula, Eq. 2.5.6, the final electron beam radius inside a solenoid can be adjusted by the cathode radius at constant magnetic field at the cathode. A smaller cathode radius results in a smaller electron beam radius in the trapping region. To reach the design current-density of  $5 \text{ kA/cm}^2$  at 5 T one has to operate the cathode at higher temperatures to provide a sufficient electron current. A larger cathode can operate with lower temperatures but provides a wider electron beam inside the trapping region. The chosen compromise between cathode radius and operation temperature considering a desired current density of  $5 \text{ kA/cm}^2$  is a cathode radius of 6 mm. The maximal emission density of the cathode material is assumed as  $j_{e,0} = 3 \text{ A/cm}^2$  at  $T_c = 1273 \text{ K}$ . To provide an electron current of 1 A the cathode operates with an emission current density of  $\approx 1 \text{ A/cm}^2$ , which is three times lower than the maximal emission current density. This corresponds to operation in the space-charge limited regime and avoids non-uniform emission due to local temperature differences and a non-uniform work function across the cathode surface. Another advantage of operating the cathode lower than the maximum emission current density is to overcome the effects of cathode roughness according to Eq. 2.4.3. If the cathode is emitting with this current density, the distance of the potential minimum to the cathode surface is  $\Delta z = 6.25 \mu\text{m}$ . The maximal cathode roughness due to manufacturing error is assumed to be  $\Delta z_c = 1 \mu\text{m}$  [Jensen 2003], which results in an additional electron temperature of  $T_{e,n} = \Delta z_c / \Delta z \cdot (U - U_M) < 0.02 \text{ eV} = 230 \text{ K}$ .

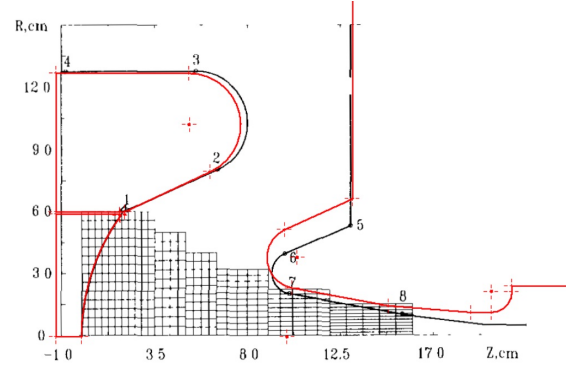


Figure 7.1.2: The geometry of the Magnicon electron gun [Baryshev et al. 1994] overlaid with the MEDeGUN geometry (red). The MEDeGUN cathode is scaled to match the Magnicon cathode radius.

The final geometry with its dimensions is shown in Fig. 7.1.3. The gap between the Wehnelt electrode and cathode is  $d = 0.1 \text{ mm}$ , close to the minimal technically feasible distance. A negative Wehnelt potential applied by default should sufficiently suppresses SEE from the lateral cathode surface without significantly disturbing the electric field distribution on the cathode surface, as concluded as an advantage in Section 6.2. The anode hole length is shortened to position the focus point of the electron beam outside the iron shield, 2 – 3 mm in front of the gun, to prevent injecting a diverging electron beam into the magnetic field. The aperture of the iron shield of MEDeGUN is indicated by the red geometry labeled with ARMCO. The aperture shapes the magnetic field distribution around the focal point and is designed to shield the region of electrostatic focusing from the magnetic field. Another purpose is providing the base to mount and fix the anode part inside the gun assembly. The iron is chosen to not saturate at field strengths of normal MEDeGUN

operations with a handover-field strength of  $B_0 \approx 0.1$  T. ARMCO iron saturating at a magnetic field of  $\approx 0.9$  T is selected as shield material, see Fig. A.2.1.

The combined assembly is shown in Fig. 7.1.3 with the iron shield in **red**. The zoom-in shows the edge of the cathode. In order to get realistic electron-beam tracing-results an edge radius of  $50\text{ }\mu\text{m}$  was assumed in accordance to the specifications to the cathode manufacturer. In all simulations with MEDeGUN the front and lateral cathode surface is considered emitting.

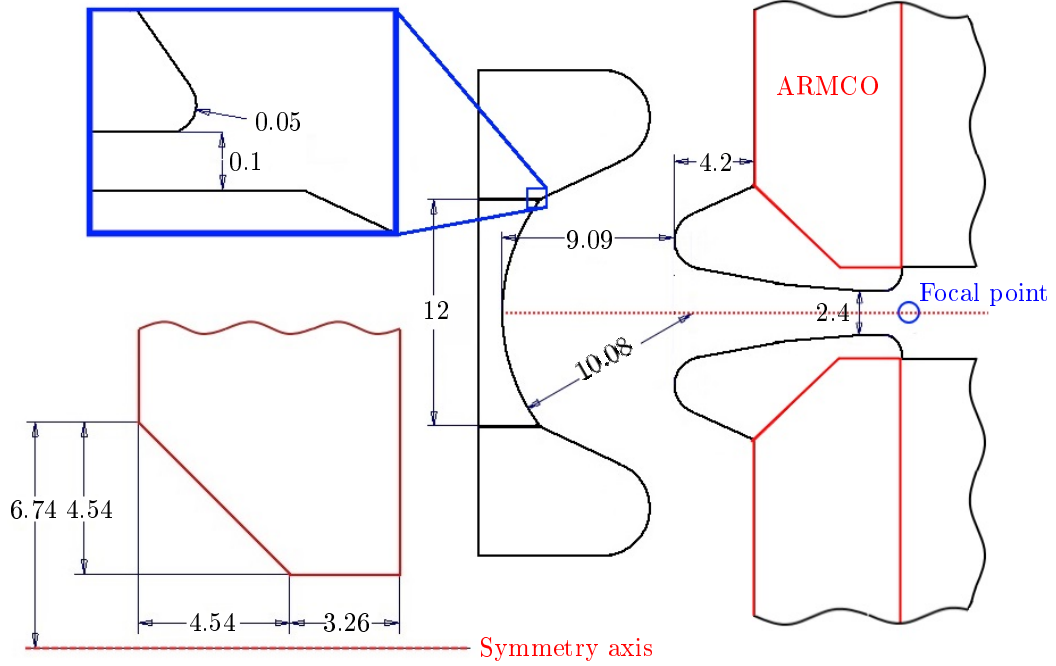


Figure 7.1.3: Overlaid electrostatic (black) and magnetic (**red**) geometries with a zoom at the edge of the cathode. The edge radius of the cathode is assumed as  $50\text{ }\mu\text{m}$ .

## 7.2 1<sup>st</sup> order characteristics

To show the basic proof of principle for this gun design, the MEDeGUN assembly was simulated without electron temperature,  $T_e = 0\text{ eV}$ . The concept of beam envelope and laminarity as quality parameters is collapsing for  $T_e \neq 0\text{ eV}$ . For operation it is essential to apply the correct matching B-field to the current density. A calculation of MEDeGUN extracting a current of  $I_e = 1$  A at an applied potential of  $U_e = 10\text{ kV}$  without considering electron temperature is shown in Fig. 7.2.1 with the electron beam shown in **blue**. The quality parameter for variation of the electron beam envelope,  $\Delta r_e$ , is zero, which indicates perfect Brillouin flow of the electron beam. Certain particle trajectories are shown in **red** to highlight the laminarity of the extracted beam. As shown in the previous chapter, trajectories with a high transverse momentum have a higher probability of being reflected by the magnetic field gradient when entering the solenoid. To estimate the reflection probability, one has to compare the angle between transverse and axial momentum with the maximal acceptance angle according to Eq. 2.5.3 or with precise calculations according to Eq. 2.5.2. The acceptance of an electron beam without temperature is shown in

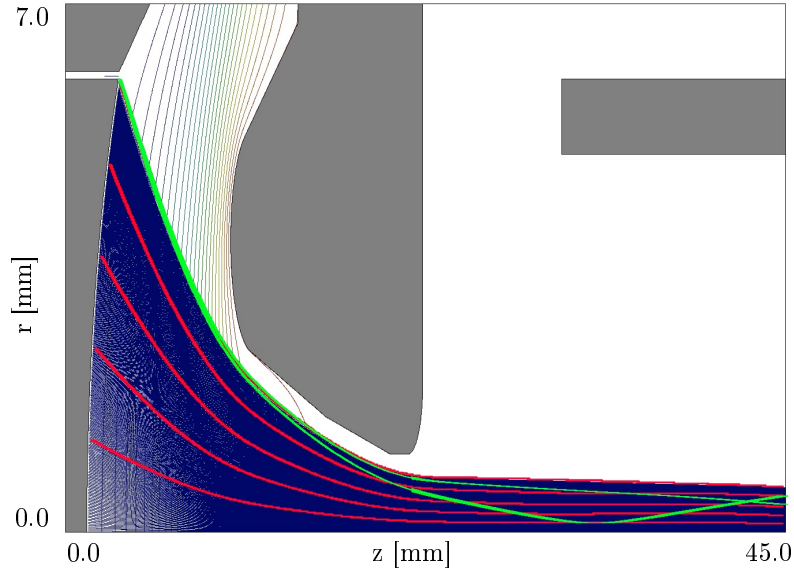


Figure 7.2.1: Trajectories of a MEDeGUN simulation (blue) overlaid with filtered trajectories (each 70<sup>th</sup> trajectory plotted, red) and the two most outer trajectories (green) with the highest transverse momentum. This simulation neglects electron temperature.

Table 7.2.1. The maximal angle of the trajectories relative to the magnetic field lines is smaller than the acceptance of a 2 T and a 5 T solenoid, which indicates a full acceptance of the electron beam. These trajectories with the highest transversal momentum are represented as green trajectories in Fig. 7.2.1. Brewer describes these translaminar electrons with high transverse momentum, which usually are emitted from the outer rim of the cathode close to the Wehnelt electrode, orbiting the core electron beam [Brewer 1959]. Simulations neglecting electron temperature show that MEDeGUN design provides an electron beam close to the Brillouin regime, which is accepted by a 5 T solenoid.

Table 7.2.1: The angle  $\alpha_{(\text{beam})}$  in [rad] of the trajectory with the highest transverse momentum in MEDeGUN-simulations with different extraction potential and the corresponding matching B-field in comparison with the acceptance angle of a 2 T/5 T-solenoid. The simulations were performed without including electron temperature.

|                            | $U_e=5 \text{ kV}$<br>$B_0=85 \text{ mT}$ | $U_e=7.5 \text{ kV}$<br>$B_0=110 \text{ mT}$ | $U_e=10 \text{ kV}$<br>$B_0=125 \text{ mT}$ |
|----------------------------|---|--|---|
| $\alpha_{(\text{beam})}$   | 0.05                                      | 0.08   | 0.06  |
| $\alpha_{(B_2=2\text{T})}$ | 0.21                                      | 0.24   | 0.25  |
| $\alpha_{(B_2=5\text{T})}$ | 0.13                                      | 0.15   | 0.16  |

### 7.3 Influence of electron temperature

A cathode temperature  $T_e > 0$  eV lowers the electron beam compression in the focal point of MEDeGUN due to thermal spread induced transverse momentum. Since the electrostatic compression and the correlated electron beam radius in the focal point remains constant, the current density increases for a higher applied extraction potential owing to the increase in extracted current. To operate the electron gun at a certain current density, one has to adjust the gun to a matching magnetic field  $B_0$ . The matching magnetic field can be approximated with Eq. 2.3.5. The solution of this equation is shown in Fig. 7.3.1, where the matching magnetic field is plotted as a function of the current density for different electron beam energies.

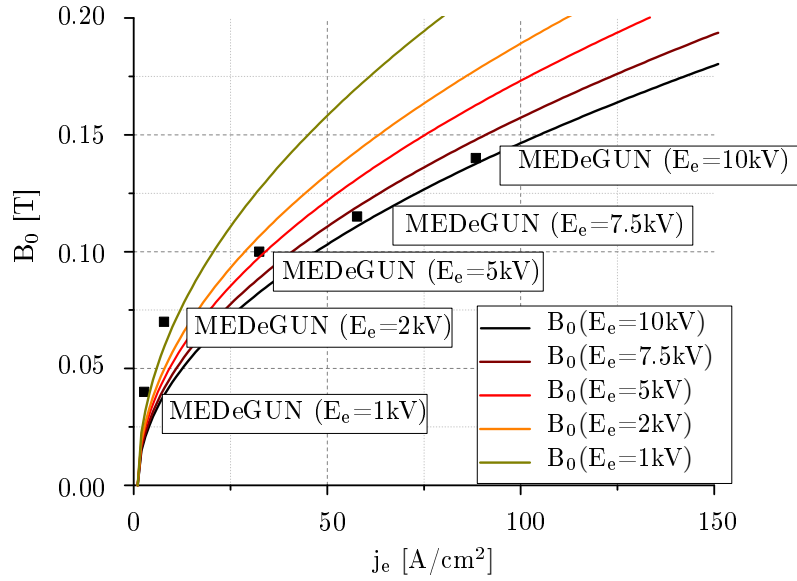


Figure 7.3.1: Matching magnetic field as a function of the current density at the focal point for a perveance of  $1.0 \mu\text{A}/\text{V}^{1.5}$ . The squares indicate simulation results.

While increasing the extraction potential in order to ramp up the electron gun to the regime of operation, one has to make sure that the correct magnetic field is applied at the front of MEDeGUN. Since the gun is axially moveable, one can translate the matching field into the axial gun position in front of the used solenoid. Because the position of the simulated MEDeGUN and the resulting matching magnetic field is based on a numerical calculations with a model solenoid, it is necessary to perform a magnetic field measurement. For this the iron shield of MEDeGUN has to be axially positioned and the magnetic field has to be measured. As shown in Fig. 7.3.2 the electron beam expands as the cathode temperature increases. While the Herrmann radius,  $r_H$ , expands linearly, the expansion of the absolute radius is governed by the increase of the radial momentum, shown with the gray and black distributions in Fig. 7.3.2.

Calculating the thermal electron beam shows that the optimal axial gun position remained the same as the electron beam calculations neglecting electron temperature. The beam profiles calculated with and without temperature at the optimal gun position are shown in Fig. 7.3.3. Comparing the total electron beam radius and



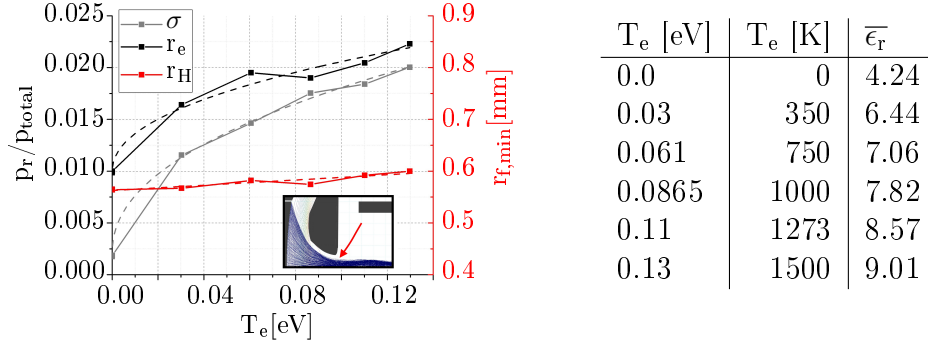


Figure 7.3.2: Total electron radius,  $r_e$ , and the Herrmann radius,  $r_H$ , of the electron beam (both right y-axis) in the focal point (indicated with the red arrow in the sub-plot) and the temperature dependent widening of the radial momenta  $\sigma$  on the left y-axis. The emittance  $\bar{\epsilon}_r$  in [mm mrad] of the electron beams evaluated in the focal point.

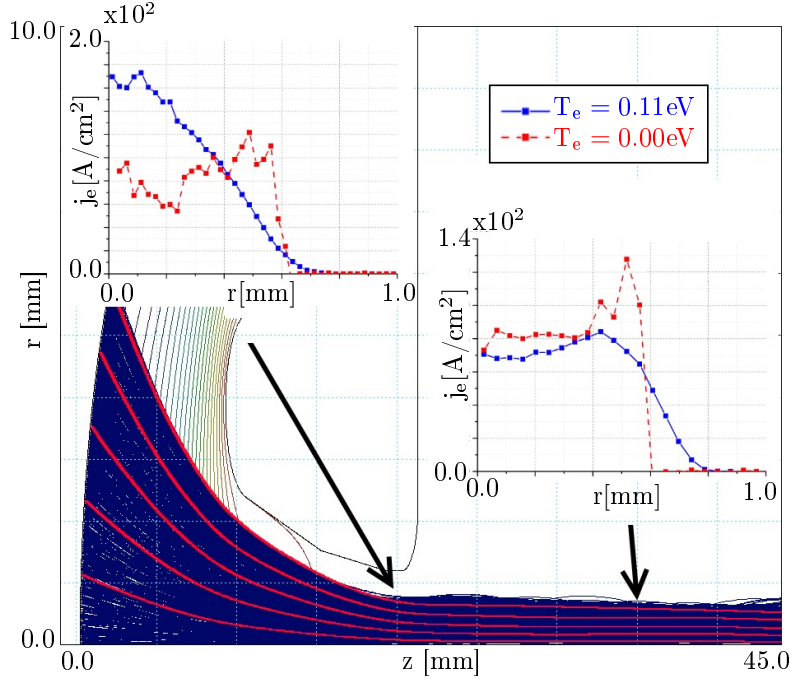


Figure 7.3.3: Optimized thermal electron beam in blue overlaid with the optimal electron beam not considering electron temperature in red. The sub-figures show the radial current-density distribution evaluated in the focal point and in the free space beyond the gun. The thermal beam is represented by blue squares connected with the straight line. The current density of the cold electron beam is represented by red squares connected with a dashed line.

the radial current density shows that the thermal electron beam is less compressed, which agrees with Herrmann's theory. The current density of a non-thermal electron beam should be box-shaped in low magnetic fields before entering the magnetic field, which the MEDeGUN-generated beam fulfills. When the non-thermal electron beam enters the solenoid, the space-charge field of the electron beam forces the radial current density into a Gaussian distribution. When taking electron temperature into account the beam compression is lowered due to the additional transverse momenta of the electrons resulting in a Wood-Saxon current-density distribution. For

investigating second order characteristics of the MEDeGUN design under realistic conditions, the electron beam is simulated in the following sections with a cathode/electron temperature of  $T_e = 0.11 \text{ eV} = 1273 \text{ K}$ .

## 7.4 Influence of the Wehnelt potential

As discussed in Section 6.2, SEE can lead to limiting loss current when being reflected by the B-field gradients. Therefore MEDeGUN is designed to operate with applied Wehnelt potential by default. The gap between cathode and Wehnelt is 0.1 mm, therefore only a small Wehnelt potential is necessary for sufficiently suppressing SEE. At an applied extraction potential of  $U_{\text{ex}} = 10 \text{ kV}$  a Wehnelt potential of  $U_w = 7 \text{ V}$  is sufficient to suppress the penetrating electric field inside the gap. A solution without applied Wehnelt potential is shown in Fig. 7.4.1(a) compared to a solution with a Wehnelt potential of  $U_w = 20 \text{ V}$  shown in Fig. 7.4.1(c). As shown in these figures translaminar trajectories occurs at non-optimal Wehnelt potential. With a Wehnelt potential chosen  $U_w < 5 \text{ V}$ , SEE are not sufficiently suppressed and overfocus in the stage of electrostatic compression. If a Wehnelt potential  $U_w > 10 \text{ V}$  is applied, the distortion of the electric field at the outer rim of the cathode causes translaminar trajectories. The optimal Wehnelt potential provides SEE-suppression and minimized distortion of the electric field. The optimized Wehnelt potential for  $U_{\text{ex}} = 10 \text{ kV}$  is  $U_w = 7 \text{ V}$ , see Fig. 7.4.1(b). For  $U_{\text{ex}} = 7.5 \text{ kV}$  and  $5 \text{ kV}$  one has to apply  $U_w = 4 \text{ V}$  and  $1.5 \text{ V}$  respectively.

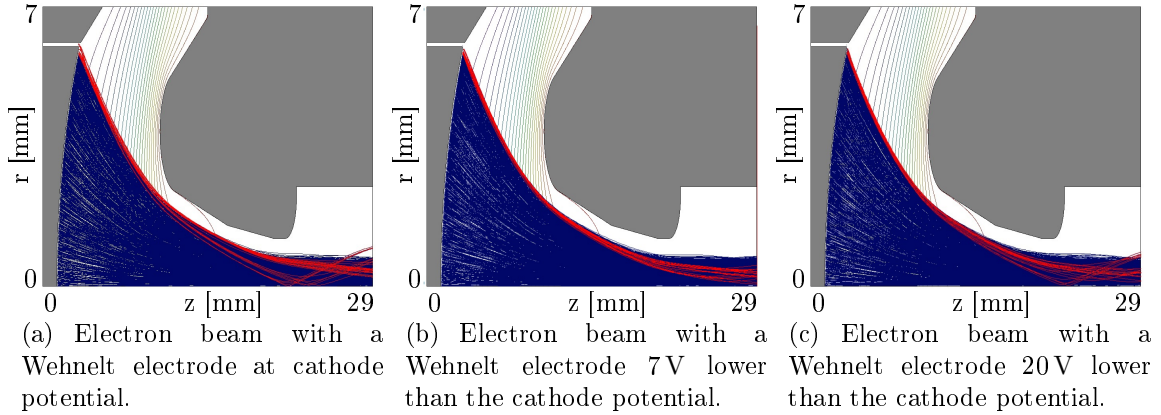


Figure 7.4.1: Electron distribution at different applied Wehnelt potentials. The outermost trajectories are shown in red.

## 7.5 Setting of the electron gun compensation coils

The heating coil inside the cathode and the resultant magnetic field is shown in Fig. 7.5.1. 4 A flowing through the heating coil current generates a magnetic field at the cathode of  $B_c = 0.4 \text{ mT}$ . The axial component of the magnetic field is evaluated on the cathode surface and is inhomogeneous due to filament ports. To compensate the magnetic field generated by the cathode heating, a small coil consisting of 16

windings is positioned at a distance of 7.5 mm to the iron shield inside MEDeGUN, see Fig. 7.5.2(a). An outer gun coil of 100 windings is positioned 1 mm in front of the iron shield of MEDeGUN. The inner and outer gun coils are capable of conducting a current of 10 A. The magnetic field generated by the outer (front) gun coil increases the matching magnetic field  $B_0$  from 120 mT to 225 mT at a outer coil current of 10 A as shown at the right y-axis. Fig. 7.5.2(b) shows the magnetic field at the cathode surface generated by the inner gun coil as a result of the assigned coil current. Below a magnetic field of  $B_c = 0.3$  mT at the cathode no distortion of the electrostatic compression could be observed. At higher assigned coil current the magnetic field reduces the electrostatic compression until the electron beam radius is equal to the anode-hole radius, which is at  $B_c = 1.6$  mT.

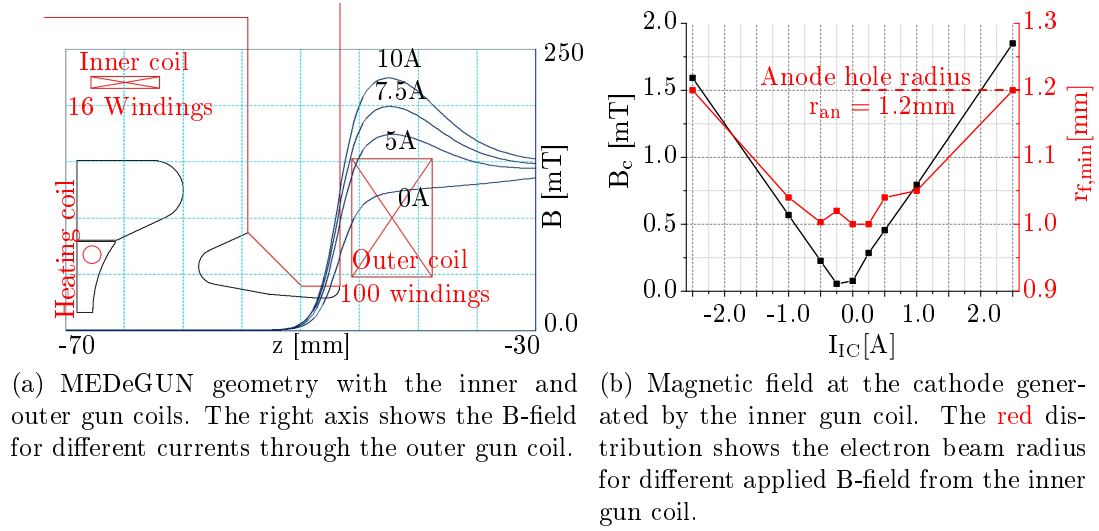


Figure 7.5.2: Generated B-fields of the inner and outer gun coils. The residual magnetic field from the fringe field of the 5 T solenoid at the cathode is 0.1 mT.

The investigations show that the gun coils are not necessary for generating a high-quality electron beam in a perfectly assembled MEDeGUN. The magnetic field on the cathode surface is generated by the heating filament, which generates a non-uniform magnetic field with its maximum at the cathode center. Because the axial magnetic field generated by the inner gun coil is homogenous at the cathode position, the inner gun coil is not capable to compensate on the cathode front surface. The magnetic fields generated by the inner coil and the heating coil at the cathode surface are superimposing each other. The inner coil shifts the distribution shown in Fig. 7.5.1 in the vertical direction. Therefore the magnetic field is not compensable at the entire cathode surface. The inner coil should therefore only be used to prevent the electron beam from over-focusing due to assembly errors or an imprecisely adjusted Wehnelt potential. The front coil should be used to fine-tune the matching magnetic field and its gradient, but not as a substitute for the process of correcting the axial gun positioning.

## 7.6 Sensitivity of the design to mechanical tolerances

To evaluate the error induced by production tolerances on the geometry of assembled gun, different types of misalignments and machining uncertainties were simulated and the beam properties recorded.

Axial misalignments were investigated by 2D simulations and accomplished with investigations for radial misalignments by 3D simulations. Manufacturing imprecisions with major influence on the beam propagation are located at the anode tip, the Wehnelt electrode, the axial cathode position relative to the Wehnelt electrode and the radial misalignment of the cathode and Wehnelt electrode relative to the anode. The angle of the anode tip was varied in steps of 1deg in both directions as shown in Fig. 7.6.1(a). Due to the angle variation the radius of the anode tip and the axial distance to the cathode change as well. The anode radius variation due to different angles is  $\approx 50 \mu\text{m}/\text{deg}$ , which is larger by a factor of 2 than modern machining precisions of  $25 \mu\text{m}$ . Here the angle of the electrode is varied at the anode tip in steps of 1deg. At three points as indicated in Fig. 7.6.1(b) the distance of the outermost trajectory to the anode electrode was read out.

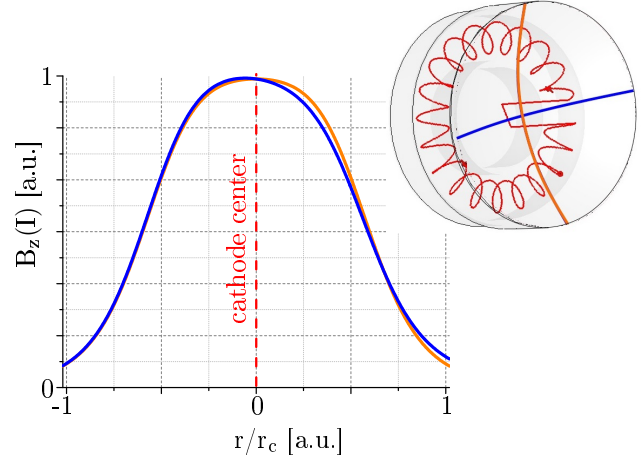


Figure 7.5.1: Axial magnetic field on the cathode surface. The magnetic field is evaluated in the radial plane covering the power ports of the heating coil filament and shown as the blue curve. The perpendicular evaluation plane is shown in orange.

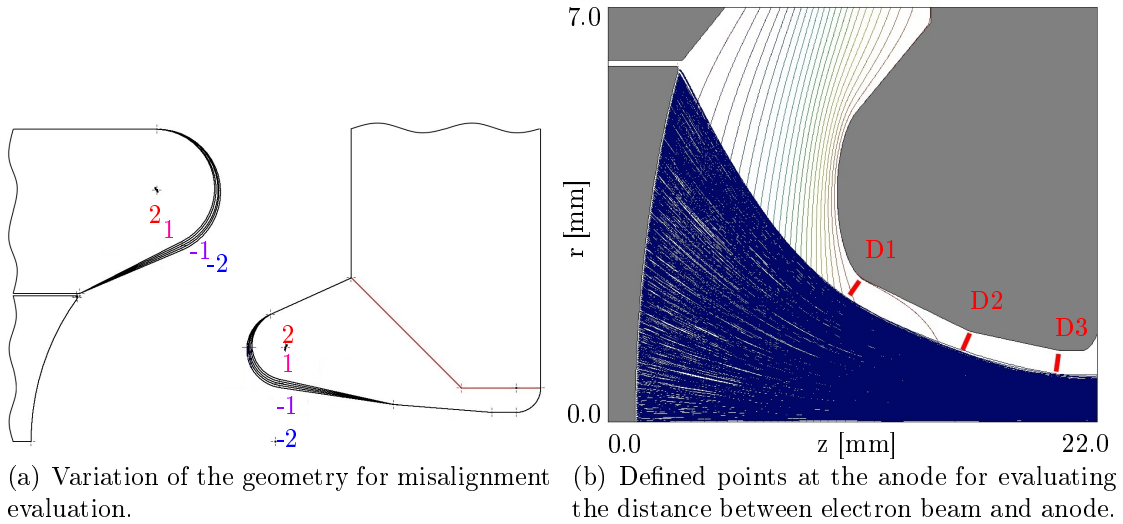


Figure 7.6.1: Investigated modifications of the anode and Wehnelt edge shape overlaid on the left figure. The right figure shows an example beam with the sampling points from the outermost electron trajectory to the anode.

The distances are shown in Table 7.6.1. The column "mod" indicates the angle relative to the z-axis. "mod 0" represents the initial design. Deviations of the Wehnelt

angle have the most significant results on the distance between electron beam and anode, which varies the distances with a factor of 3, see D3 in Table 7.6.1. Therefore the gun becomes more sensitive to the temperature related loss current at the anode. In addition the emittance is calculated at a defined axial position, which is 30 mm in front of the cathode. Due to varying beam compression the axial position of the electron-beam focal point varies. An increased emittance as a result of the the reduced beam quality leads to an increased probability for loss current occurring during the injection of the beam into the high magnetic field. Therefore an increased emittance should be avoided. Symmetric manufacturing errors of the anode hole ra-

Table 7.6.1: Evaluated distances between the electron beam and anode in [mm] for different geometry modifications according to Fig. 7.6.1(a). "mod" indicates which shape was varied. The distances were evaluated at three defined points, D1 - D3, at the anode. The emittance in [mm mrad] was evaluated at a defined axial position.

| mod<br>[deg] | Anode      |            |            |                    | Wehnelt    |            |            |                    |
|--------------|------------|------------|------------|--------------------|------------|------------|------------|--------------------|
|              | D1<br>[mm] | D2<br>[mm] | D3<br>[mm] | $\bar{\epsilon}_r$ | D1<br>[mm] | D2<br>[mm] | D3<br>[mm] | $\bar{\epsilon}_r$ |
| -2           | 0.38       | 0.22       | 0.23       | 5.62               | 0.43       | 0.40       | 0.39       | 5.77               |
| -1           | 0.40       | 0.21       | 0.23       | 5.71               | 0.35       | 0.28       | 0.33       | 5.61               |
| 0            | 0.36       | 0.22       | 0.25       | 5.43               | 0.36       | 0.22       | 0.25       | 5.41               |
| 1            | 0.38       | 0.22       | 0.23       | 5.65               | 0.25       | 0.18       | 0.23       | 5.65               |
| 2            | 0.38       | 0.20       | 0.21       | 5.58               | 0.21       | 0.10       | 0.13       | 5.57               |

dius lead to less compression but not to a reduction of beam quality. Although the beam radius does not scale linearly with the anode hole radius, smaller anode holes result in a smaller distance between electron beam and hole surface. Therefore the manufacturing tolerance of the anode hole should be less than  $\Delta d_a = 50 \mu\text{m}$ .

In Brillouin electron guns the electron beam propagation in the electrostatic compression region is sensitive to the axial cathode position relative to the Wehnelt electrode due to field distortion at the cathode edge and the varied perveance. To evaluate the robustness of MEDeGUN with respect to assembly uncertainties the cathode is moved from the axial position  $\Delta z = 0.0 \text{ mm}$ , where the cathode edge following the cathode bending circle is axially aligned to the Wehnelt hole, backwards into the Wehnelt electrode. The quality of the electron beams in the varied geometries are compared to the default position  $\Delta z = -0.1 \text{ mm}$ . The calculated distances of the electron beam are tabulated in Fig. 7.6.2. The electron beam compression in the focal point and therefore the distances to the anode electrode increases significantly when shifting the cathode back at the cost of decreased perveance. If the cathode is aligned with the Wehnelt electrode, as shown in Fig. 7.6.3(a), the focusing of the electron beam is not sufficient to ensure a adequate distance between anode aperture and electron beam. Fig. 7.6.3(b) shows the evaluated optimum of electrostatic beam compression and the distortion of the outer trajectories at a cathode position of  $\Delta z = -0.1 \text{ mm}$ . Here the outer trajectories are injected into the matching magnetic field with a transverse momentum similar to the front-emitted electrons. A solution with higher electron beam compression due to a cathode shift of  $\Delta z = -0.3 \text{ mm}$  is shown in Fig. 7.6.3(c). The outer electrons form a beam halo, which defeats the advantages of the more compressed electron beam. Shifting the cathode into the Wehnelt leads to higher electron beam compression at the cost of translaminar trajectories. Higher current density at the focal point increases

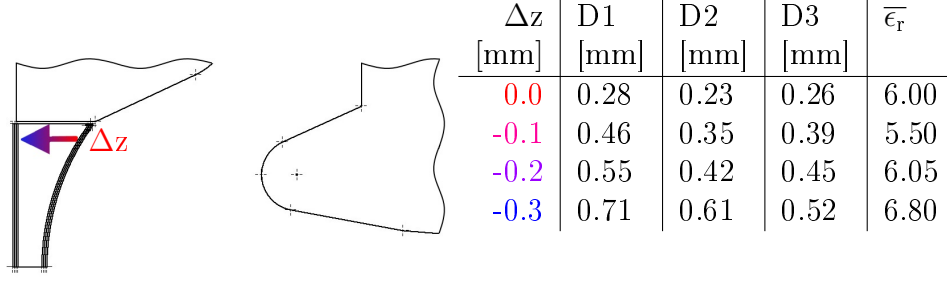


Figure 7.6.2: Evaluated distances between the electron beam and anode in [mm] at different cathode positions relative to the Wehnelt electrode as shown in the left figure. The distances were evaluated at three defined points, D1 - D3, at the anode. The emittance in [mm mrad] was evaluated in the beam focal point.

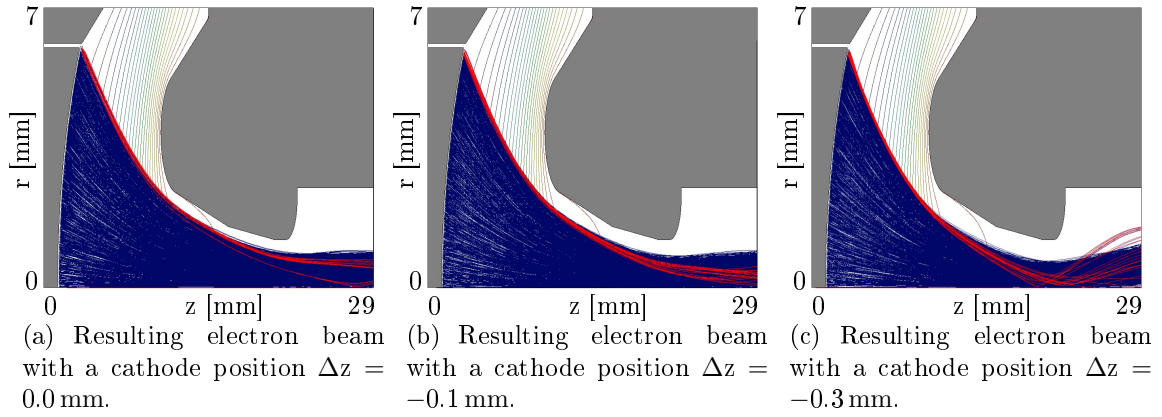


Figure 7.6.3: Resultant beam properties for different cathode positions. The outermost trajectories are plotted red.

the necessary matching magnetic field strength, where the translaminar trajectories form a wide beam halo with a high reflection probability.

To investigate radial misalignments the MEDeGUN geometry was simulated in 3D, where at each step the cathode and Wehnelt electrode is radially misaligned relative to the anode and iron shield in steps of 0.1 mm. Fig. 7.6.4 shows the phase space of the electron beam considering this radial misalignment. While misplacing the cathode in  $y$ -direction, the beam is deflected in the  $x$ -direction and expands in the  $y$ -direction as shown in Fig. 7.6.4(a) and 7.6.4(b). An alignment precision of less than 50  $\mu\text{m}$  is recommended to ensure a sufficiently centered electron beam. At a radial misalignment of 0.3 mm the electron beam hits the anode and loss current occurs. Along with the loss current, the electron beam gains additional transverse momentum and is radially displaced, which lowers the probability of acceptance by the solenoid. In Fig. 7.6.5(a) the electron beam propagation from a cathode and Wehnelt with a radial misalignment of 0.1 mm is shown. For comparison Fig. 7.6.5(b) shows the propagation at a misalignment of 0.3 mm. Because the direction of misalignment is chosen to be the  $y$ -direction, the electron beam is mainly distorted in the same direction.

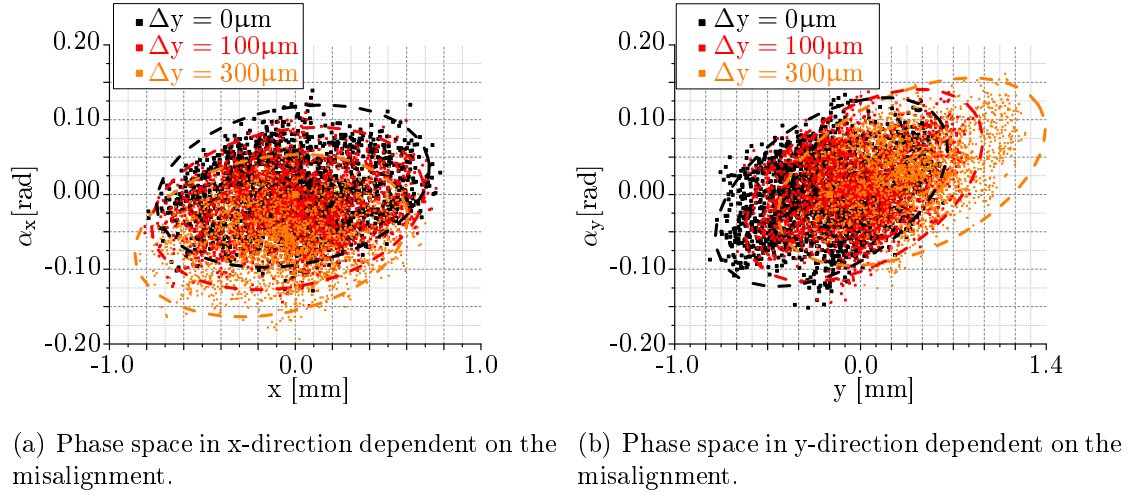


Figure 7.6.4: Phase space of an electron beam emitted from an aligned cathode (black), a cathode shifted 0.1 mm (red) and 0.3 mm (orange) in the y-direction recorded at the focal point. The dashed lines are for guiding the eyes and indicate the particle distributions.

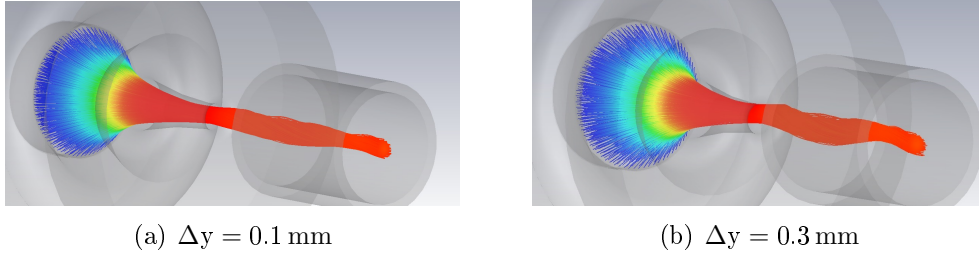
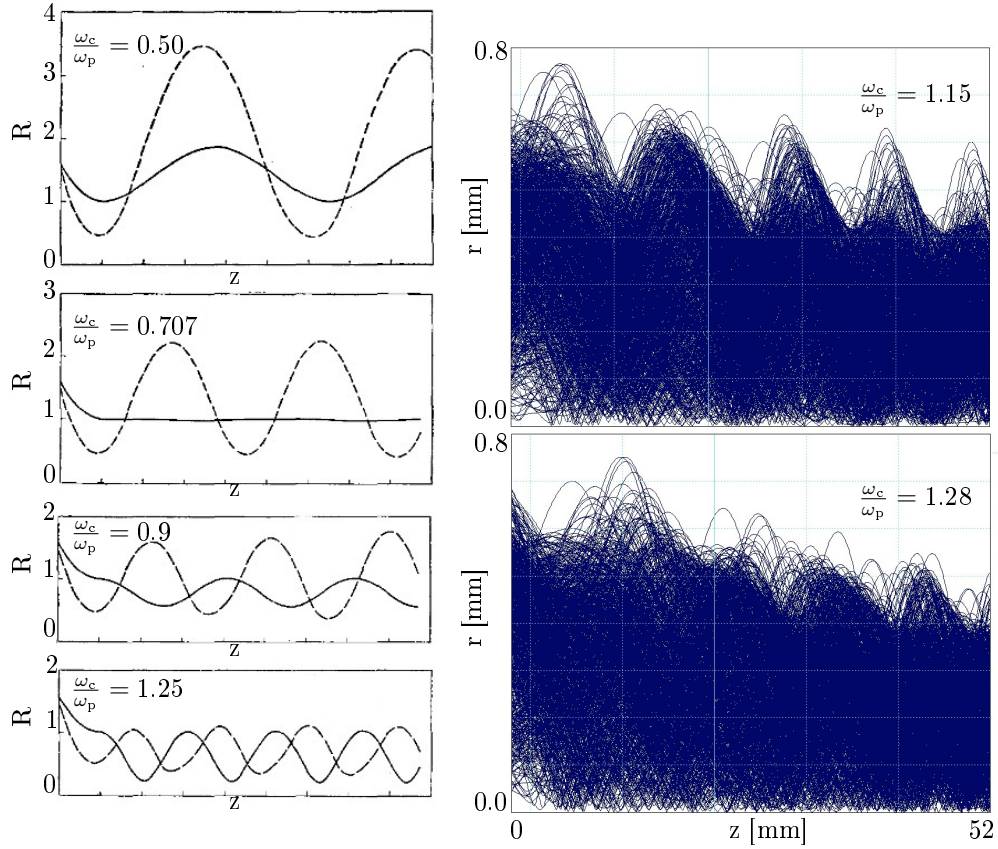


Figure 7.6.5: 3D simulation of an electron beam emitted from a cathode, which together with the Wehnelt are radially misaligned relative to the anode hole and iron shield.

### 7.6.1 Influence of the axial position of the gun assembly

To ensure a correct matching magnetic field for the electron beam, the gun has to be positioned at the correct axial position. When injecting the electrostatically compressed electron beam into the magnetic field, the strength of the magnetic field relative to the optimal matching magnetic field determines the beam quality, especially in higher magnetic fields. Fig. 7.6.6(a) shows the electron beam for different matching magnetic fields. This is expressed by the ratio of the two frequencies  $\omega_c/\omega_p$  corresponding to the Brillouin condition described by Eq. 2.3.4. According to this equation the optimal magnetic field is at  $\omega_c/\omega_p = 0.707$  for non-thermal electron beams. For thermal electron beams the radial momentum and the resulting gyro-wave lengths spread. Therefore thermal electron beams have to inject into higher matching magnetic fields. An electron beam calculated with temperature is shown in Fig. 7.6.6(b). The axial gun position is axially varied by 1 mm, which corresponds to a shift of the matching magnetic field from  $B_0 = 152$  mT shown in the upper figure to  $B_0 = 146$  mT shown in the lower figure. This variation of beam quality indicates a precision of the axial gun position of  $< 0.5$  mm when positioning the electron gun according to measured magnetic field values.





(a) Electron beam propagation (solid line) with the orbiting translaminar halo (dashed line) at different matching B-fields, taken from [Brewer 1959]. (b) Thermal electron beam propagation at different matching B-fields as a solution of FP.

Figure 7.6.6: Electron beam propagating towards the solenoid for different matching magnetic field strengths.

## 7.6.2 Summarized error discussion

Since the investigations were performed without combining manufacturing errors and errors due to misplacement, the maximal error tolerances are chosen conservatively. For the variation of the Wehnelt and anode angle a maximal error of less than  $\Delta\alpha = 0.5^\circ$ , which results in an angularly dependent variation of the anode- or Wehnelt-tip radius of  $10\text{ }\mu\text{m}$ , is recommended. The axial position of the cathode relative to the Wehnelt can vary  $\Delta z_{(+)} \leq 20\text{ }\mu\text{m}$  towards the anode and  $\Delta z_{(-)} \leq 50\text{ }\mu\text{m}$  into the Wehnelt hole. The variation dependent beam properties summarized in Tab. 7.6.1 and 7.6.2 are visualized in Fig. 7.6.7. For the anode hole diameter a variation of less than  $\Delta d \leq 50\text{ }\mu\text{m}$  is recommended. For the radial misalignment of the cathode and Wehnelt relative to the anode and iron shield a  $\Delta r \leq 30\text{ }\mu\text{m}$  is recommended.



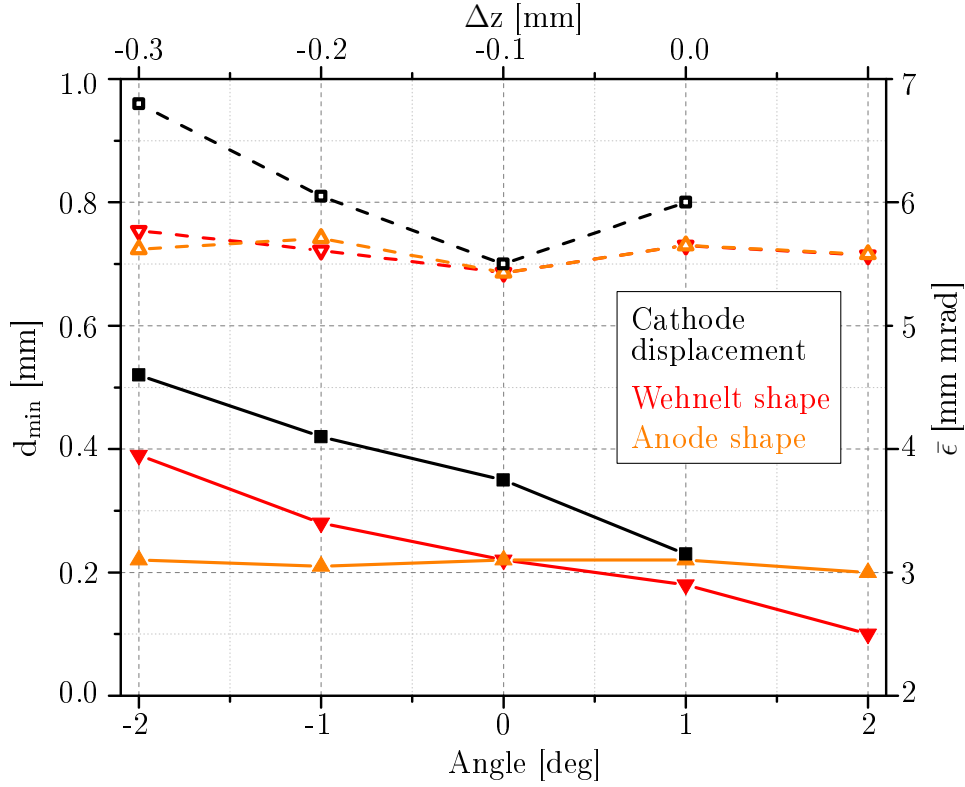
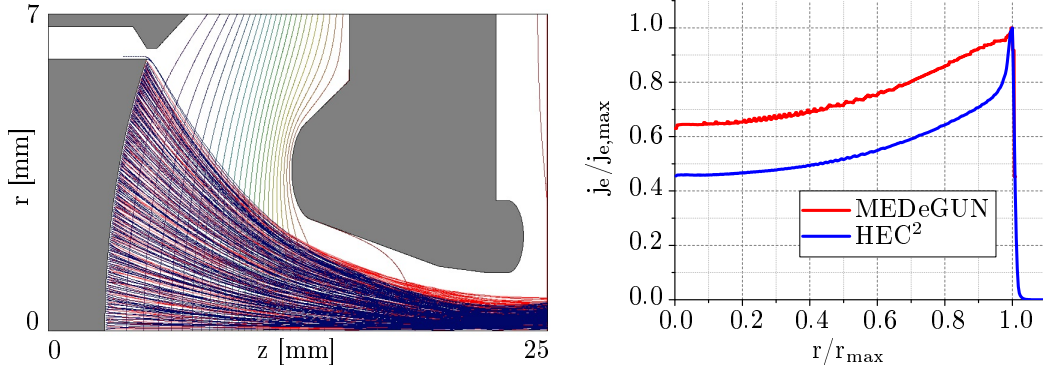


Figure 7.6.7: Summary of the error-tolerance evaluation shown in Tab. 7.6.1 and 7.6.2. The inclination of the Wehnelt and anode shapes is expressed in degrees (lower x-axis), while the cathode shift is in [mm] (upper x-axis). The minimal distance between the resulting electron beam and the anode is plotted by solid lines (left y-axis) and the resulting emittance is represented by open symbols and dashed lines (right y-axis).

## 7.7 MEDeGUN versus HEC<sup>2</sup>

To compare the MEDeGUN design with the HEC<sup>2</sup> gun the HEC<sup>2</sup> geometry was down-scaled to a cathode size equal to MEDeGUN. The resultant electron beams are shown in Fig. 7.7.1(a). HEC<sup>2</sup> reaches a higher electrostatic compression than MEDeGUN, which results in larger distances to the electrodes, for instance the anode. The higher compressed electron beam in the HEC<sup>2</sup> geometry requires a higher matching magnetic field. Utilizing the fringe field of the solenoid for injection the gun has to be positioned closer to the solenoid, where the magnetic field strength and gradient is higher. This steeper magnetic field gradient directly increases the sensitivity of the axial gun position on the beam quality. A disadvantage of the electron beam compressing electric field inside the HEC<sup>2</sup> gun is higher current density at the outer rim of the cathode, shown in Fig. 7.7.1(b) in comparison to the emission density of MEDeGUN. Both electron guns are traced considering electron temperature and optimal Wehnelt potentials. This difference in current density magnify during the compression process and leads to a hollow-beam like properties. The ratio of the emission current density between cathode center and cathode edge of HEC<sup>2</sup> and MEDeGUN could be improved from 1:2.22 to 1:1.54.

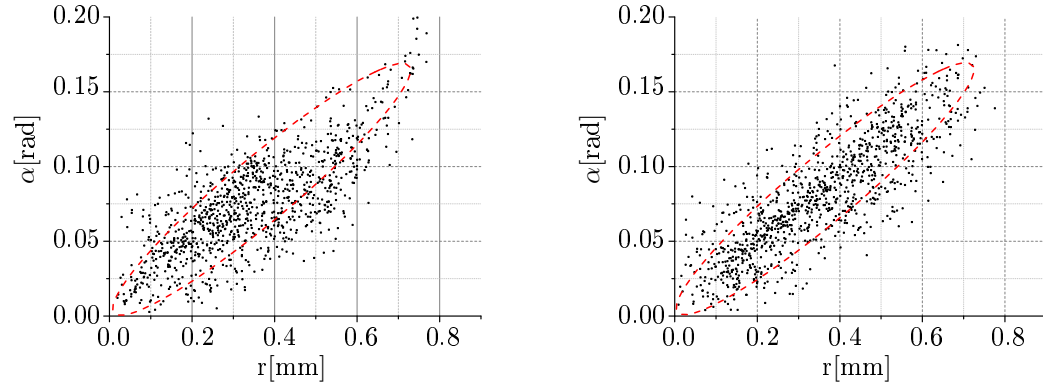
Another advantage of the MEDeGUN design is the reduced gap between Wehnelt electrode and cathode at the cost of higher assembling precision. The required applied Wehnelt potential is higher in the HEC<sup>2</sup> design in order to properly suppress the penetration of the electric field into the gap. This leads to translaminar trajectories emitted from the cathode edge orbiting the highly focused electron beam.



(a) Electron beam simulated in the geometry of MEDeGUN (red) and HEC<sup>2</sup> (blue). Both geometries are adjusted to the HEC<sup>2</sup> cathode position. Shown is the HEC<sup>2</sup> geometry. (b) Normalized current density on the normalized cathode surface of MEDeGUN (red) and HEC<sup>2</sup> (blue), see also [Pikin et al. 2013].

Figure 7.7.1: Electron emission and propagation properties of the HEC<sup>2</sup> and the MEDeGUN geometries in direct comparison.

The reduced electron beam compression and smaller cathode-Wehnelt gap result in a better beam quality. The phase space of the resulting electron beam of HEC<sup>2</sup> and MEDeGUN are shown in Fig. 7.7.2(a) and (b). A phase space of an electron beam without temperature is considered to be a line with a magnetic-field dependent angle as the slope, see Fig. 6.2.9(a). The widening of the phase space due to the electron temperature is indicated by the red dashed circle. Every trajectory outside this circle is considered as translaminar trajectory, which has a higher probability of reflection.

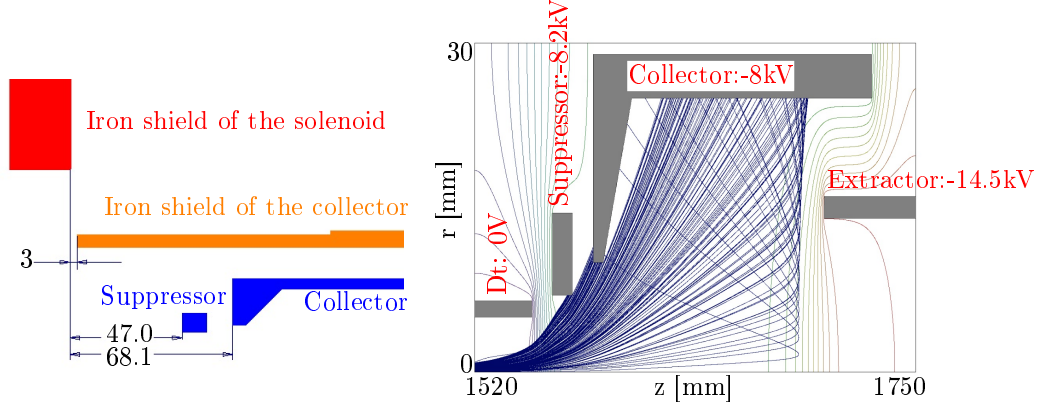


(a) Phase space of the HEC<sup>2</sup> gun in the focal point. (b) Phase space of MEDeGUN in the focal point.

Figure 7.7.2: Phase spaces of the HEC<sup>2</sup> gun and the MEDeGUN design at equal magnetic fields. The red circles indicate the phase space distribution. Translaminar trajectories are close to the z-axis but have a very high radial momentum.

## 7.8 Modification of the TwinEBIS collector

It has to be insured by simulations that the collector currently used in TwinEBIS is capable of recovering the MEDeGUN-generated electron beam. The important distances of the collector geometry are shown in Fig. 7.8.1(a).



(a) Distances in mm relative to the outer surface of the iron shield of the main solenoid (red). The iron shield of the collector is orange, the suppressor and collector are displayed in blue. (b) Propagation of the electron beam generated with MEDeGUN ( $I_e = 1$  A,  $E_e = 10$  keV,  $T_e = 0.11$  eV) in the TwinEBIS collector.

Figure 7.8.1: Default geometry of the collector assembly and the resulting propagation of an electron beam emitted by MEDeGUN.

A first calculation of the beam propagation in the collector is shown in Fig. 7.8.1(b). The electron beam is generated with MEDeGUN and carries 1 A at an energy of 10 keV. The collector potential is  $U_{\text{coll}} = -8$  kV and the suppressor potential is chosen to be close to but below the collector potential. The potential of the extractor can be chosen freely according to the electron energy. In this case it is set to  $U_{\text{ext}} = -14.5$  kV. As seen in Fig. 7.8.1(b) the electron beam does not reach completely the collector although the potentials have been adjusted. On the suppressor 246 mA out of 1 A is deposited. The front and the lateral surface of the collector impinges  $I_{\text{loss, coll}} = 420$  mA. Considering investigations of the BSE at the TestEBIS collector indicates that 30 % (= 120 mA) of that current will re-emit into the drift tube volume.

In order to modify the collector assembly while avoiding re-machining of the collector electrodes, different steps have to be taken:

1. Move the collector cross 2.5 cm closer to the main solenoid in order to keep the electron beam more compressed when entering the collector.
2. Move the collector closer to the suppressor in order to decrease the retardation distance of the electron beam which results in a later widening of the beam.
3. Move suppressor, collector and extractor 2 mm closer to the drift tube, which reduces the drift distance of the electron beam inside the collector iron shield. That decreases the decompression of the beam and reduces the spread angle of the beam.

A comparison of the optimized and the original geometry is shown in Fig. 7.8.2. Space restrictions in the design prevents further displacements. Simulations with the optimized geometry show perfect acceptance of the collector and are given in Fig. 7.8.3(a). The optimized collector accepts the beam, which is indicated by the absence of deposited current at the suppressor and on the outer and lateral surfaces of the collector. In order to determine the deposited power density in the collector the impact position and energy of the trajectories were recorded and the power calculated. The power density was evaluated in  $\text{W}/\text{mm}^2$ , see Fig. 7.8.3(b). The design power deposition limit is 1 kW - 2 kW, which should be accepted by the cooling system.

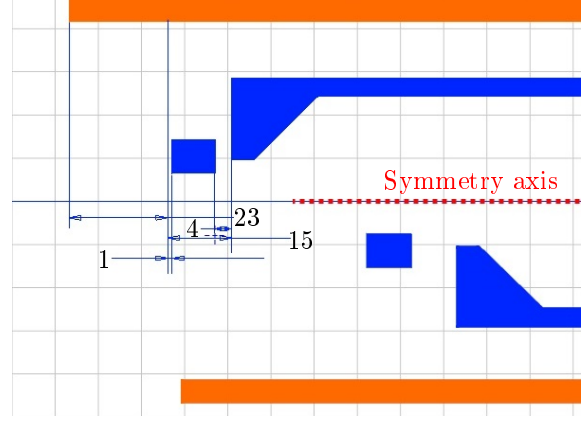
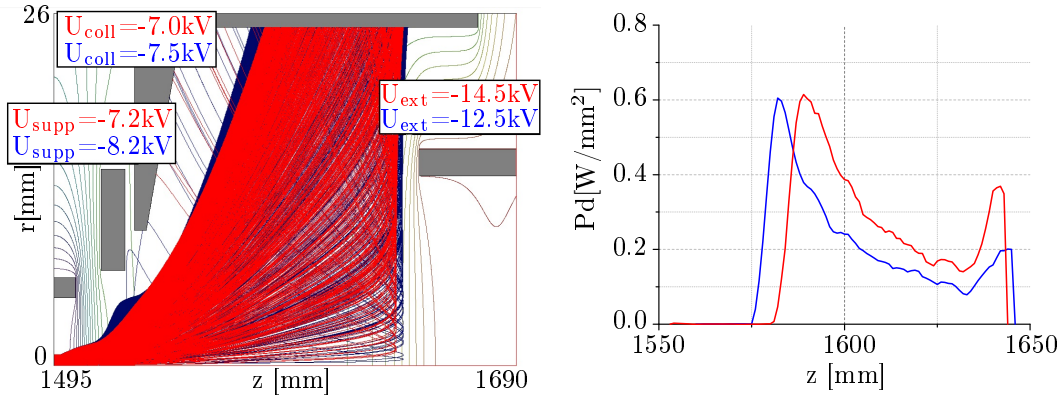


Figure 7.8.2: Optimized geometry and the original geometry shown above and below the symmetry axis. The color coding and the reference point for positioning is taken from Fig. 7.8.1(a). All distances are in [mm].



(a) Electron beam propagation ( $I_e = 1\text{ A}$ ,  $E_e = 10\text{ keV}$ ,  $T_e = 0.11\text{ eV}$ ) in the optimized collector. The potentials of the corresponding calculation are shown in the same colors as the trajectories. The drift tube on left boundary is set to ground potential.

(b) Calculated power deposition of the simulations shown in the left figure. The colors are associated with the corresponding simulations.

Figure 7.8.3: MEDeGUN-generated electron beam deposited in the optimized collector. The red and blue colored trajectories and power density are simulated considering a 3 kV and a 2.5 kV power supply for the collector, respectively.

## 7.9 Beam transport into high B-field

To evaluate the expected ionization rate it is necessary to know the current density inside the solenoid. For this reason the electron beam is traced from the cathode inside MEDeGUN into the 5 T solenoid. The traced electron beam is  $I_e = 1\text{ A}$  at  $U_{\text{ex}} = 10\text{ keV}$ , which results in a kinetic energy of  $\approx 8.5\text{ keV}$  in the trapping region.

To find more easily the correct matching magnetic field the gun is simulated in the fringe field of a 2 T-solenoid, where the magnetic field strength in front of MEDeGUN is less sensitive to the axial position. This beam was translated into the matching magnetic field of a 5 T-solenoid for further investigations.

The beam is traced from the electron gun into a B-field of 4.91 T in 14 stages, which are limited by the magnetic field gradient of  $\Delta B < 0.4$  T per stage with a total tracing precision of  $\Delta E/E < 0.15\%$  over a distance of  $dz = 37$  cm. Fig. 7.9.1 shows the assembled solution of the complete simulation series. The beam was evaluated every 5 mm traveling distance. For a better overview the slices indicating the passage of the beam at an integer value of the magnetic field are plotted in **red**. The shown electron beam is limited at  $r = 0.4$  mm, which cuts most of the electrostatic compressing inside MEDeGUN. The dotted lines show the calculated Herrmann radius and the resulting current density.

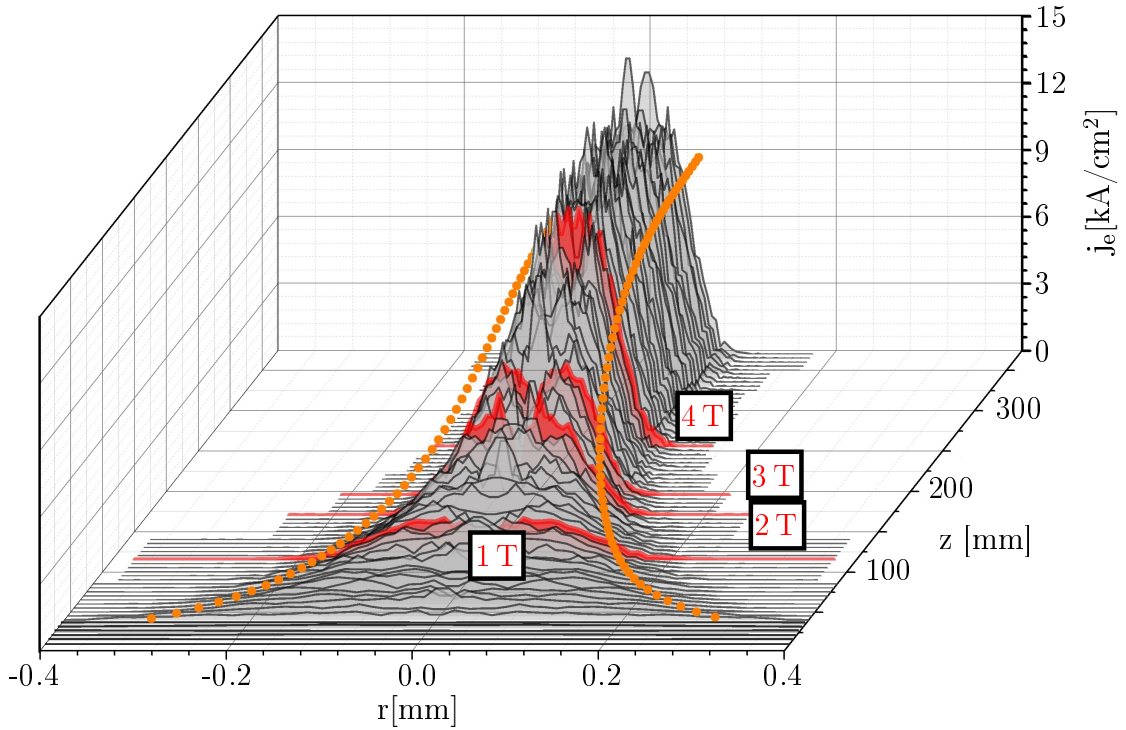


Figure 7.9.1: Electron beam propagation into the 5 T-solenoid evaluated at every 5 mm travel distance. The distribution shows the radial dependent current density. The **red** slices show the beam when passing an integer of the B-field strength. The lines of **orange** dots show the calculated Herrmann radius and the resulting current density.

The result of the simulation in a 4.91 T field is shown in Fig. 7.9.2. In this figure the lower line shows the theoretical Herrmann radius according to Eq. 2.5.6, compared to the upper line, which is the Herrmann radius as a result of the numerical evaluation of the trajectories. The lower figure shows the calculated current density from the numerically evaluated Herrmann radius. It is shown that changes in the radius varies the current density by approximately 10 % and create microscopic traps inside the trap region of the EBIS/T, which have a depth of  $U = 5$  V. The minor current-density ripples in the range  $\Delta j_e < 0.1$  A/cm<sup>2</sup> are due to the trajectory based method of tracing and will vanish at the real electron beam.

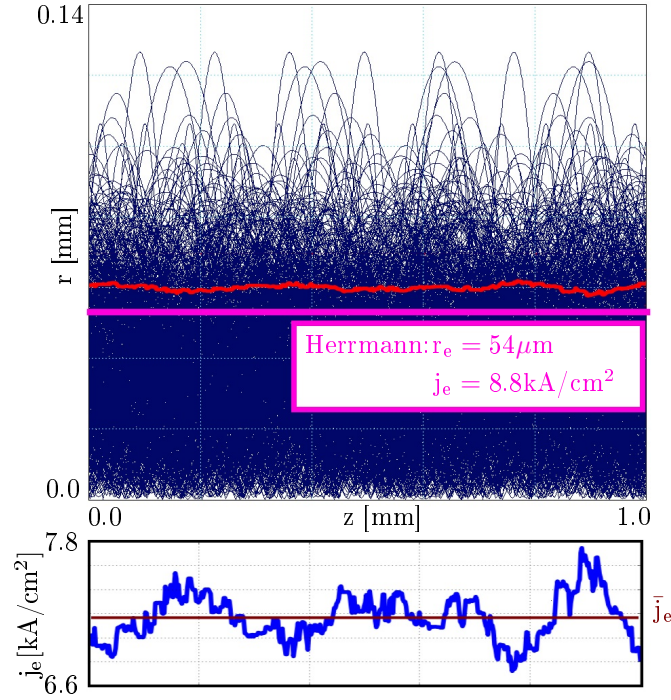


Figure 7.9.2: Upper figure shows the electron beam at  $B = 4.91$  T. The red distribution is the Herrmann radius evaluated from the calculated solution. The pink line shows the theoretical Herrmann radius of the gun conditions during the simulation. The lower figure shows the local and the average current densities from the simulations.

The starting emission node of the trajectories with the highest radial momentum at  $B = 4.91$  T were determined and the particle microscope was applied in order to investigate a potentially overlooked current reflection due to low particle resolution. For each emission node the initial five trajectories were substituted with 1000 new particles and traced in the space charge field of the initial electron beam into the 5 T-solenoid. No loss current could be observed. Evaluating the phase space of the simulated electron beam at  $B = 4.91$  T shows a maximal angle between radial and axial momentum of  $\tan(p_{\perp}/p_z) = 1.16$  rad, see Fig. 7.9.3. Calculating the maximal B-field strength where the first electrons reflect according to Eq. 2.5.3 results in a magnetic field of  $B_{\max} = 5.84$  T. Investigations of the reflected SEE at TestEBIS show that reflected electrons might pass the anode and be reflected at the cathode or Wehnelt electrode and propagate back into the solenoid with a certain probability of being accepted. Possible solutions to avoid the loss current at the anode due to reflections are post-acceleration of the electron beam, operation of the cathode at lower temperatures or insertion of a grounded aperture between gun and solenoid.

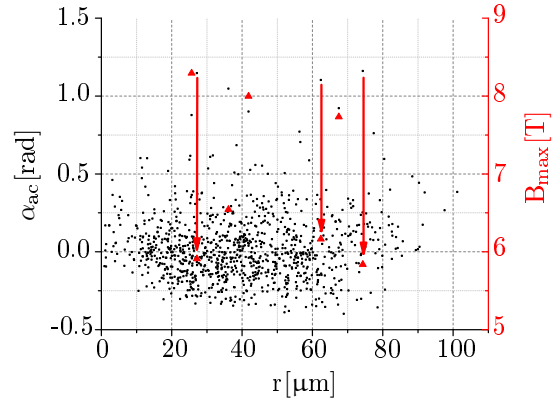


Figure 7.9.3: Phase space of the electron beam without ExB-drift at  $B = 4.91$  T (left axis). The particles with the highest transversal momentum have the lowest reflection magnetic field, shown as red triangles (right axis).

## 7.10 Charge-breeding efficiency

Investigations of the charge-breeding performance of a MEDeGUN-generated electron beam are shown in Fig. 7.10.1 for the selected elements in comparison to real REXEBIS. The calculations consider ionization and recombination processes described in Section 2.2.1 and 2.2.2. To approximate the charge-breeding time according to Eq. 2.2.6 the library of ion potentials [Onlinelib] established by the automatized calculation program, see Section 3, is used. Compared are the breeding times of REXEBIS and MEDeGUN with a 5 T magnet. A 5 T magnet equipped with MEDeGUN reduces the breeding time for  $C^{6+}$  from  $\tau = 29$  ms to  $\tau = 1.3$  ms. For lanthanum, as an example of medium-heavy elements, the electron energy of either of the electron guns is not sufficient for generating bare ions. The charge-breeding time for  $La^{47+}$  is reduced from  $\tau = 10.6$  s to  $\tau = 69$  ms. The charge-breeding time for heavy elements such as  $U^{60+}$  will be reduced from  $\tau = 5$  s to  $\tau = 38$  ms, for  $Mt^{63+}$  it will be reduced from  $\tau = 3.7$  s to  $\tau = 30$  ms. One has to note that the charge-breeding time in an experiment is higher than the presented calculated values by at least a factor of 2. This is because the electron density used for evaluating the charge-breeding time is derived from the Herrmann radius and is therefore higher than the true effective current density along the total electron beam.

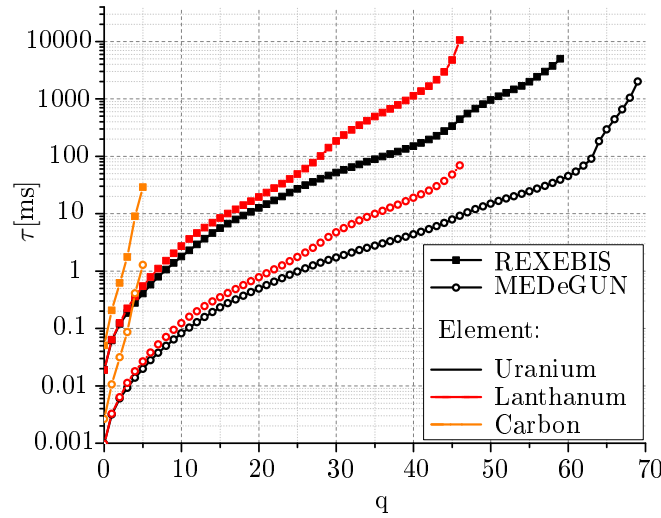


Figure 7.10.1: Total breeding time for carbon, lanthanum and uranium ions in REXEBIS ( $E_e = 4.5$  keV,  $j_e = 200$  A/cm<sup>2</sup> at  $B=2$  T) and MEDeGUN-EBIS/T ( $E_e = 10$  keV,  $j_e = 7.5$  kA/cm<sup>2</sup> at  $B=5$  T).

A breeding time of around 2.6 ms for  $C^{6+}$  is necessary for a charge breeder equipped with MEDeGUN and a magnetic field of 5 T in the trapping region providing a breeding rate of 400 Hz. Fig. 7.10.2(a) and 7.10.2(b) show the necessary current density and electron energy at which MEDeGUN has to operate. The energy dependency is linear to the first order, because the applied electron-beam energy is several times higher than the optimal energy of the charge-state dependent ionization energy of carbon, compare to the FAC-solution of carbon in Section 3. In this energy range of operation the cross section for electron-impact ionization is linearly decreasing.

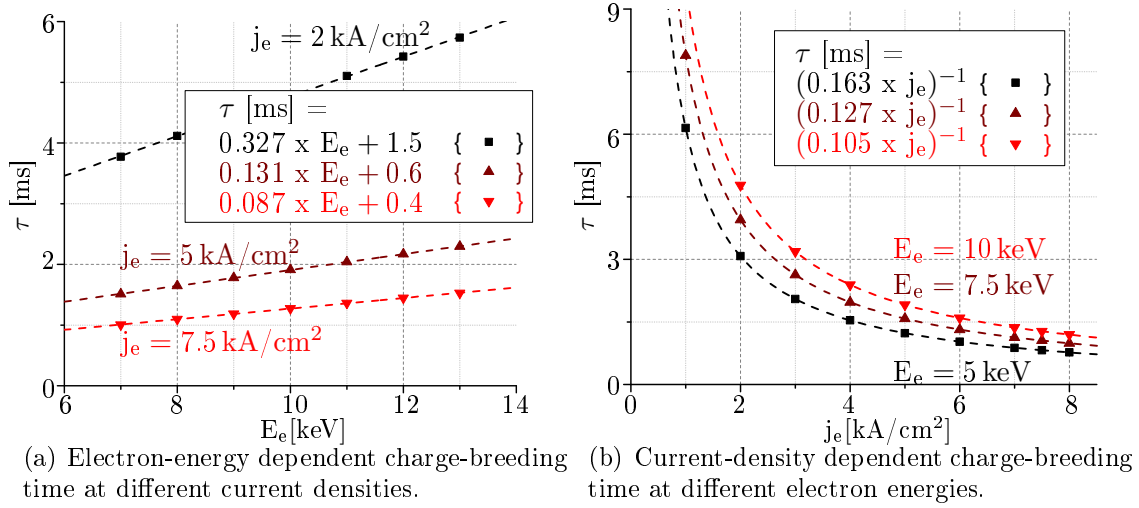


Figure 7.10.2: Calculation of the total breeding time for  $C^{6+}$  with varied electron energy and current density.

Regarding the electron beam stability during operation, the MEDeGUN fulfills the TSI-criterion according to Eq. 2.5.7, which requires a minimal current density of  $j_e = 173$  A/cm<sup>2</sup>. This indicates that only limited electron-impact heating of the ions should occur.



## 8 Conclusion and outlook

In this work different strategies for increasing the current density and the resulting decrease of the breeding time were investigated and developed. First the physical limits of the current REXEBIS design were estimated.

To increase the current density above the immerse electron gun limitation the HEC<sup>2</sup> gun is developed and currently being commissioned. The commission stalled due to loss current occurring at the anode. To overcome and understand this process, simulation methods were developed, which describe the reflection of electrons at the magnetic field gradient of the main solenoid. Furthermore it was proven that the collector should be modified in order to recover the electron beam of the HEC<sup>2</sup> gun. Finally a new electron gun, the MEDeGUN, is designed and discussed. This electron gun is optimized for current density ensuring a compatibility to high-frequency second generation therapy centers.

Numerical procedures, such as the simulation of thermionic current emission with intermixed space charge limited emission and cluster-supported 3D simulations of the electron gun, were established which precisely describe the emission properties of the REXEBIS electron gun. It was proven for the first time that the REXEBIS gun design is capable of providing an electron beam current above the design value. TwinEBIS, equipped with a LaB<sub>6</sub> crystal as cathode, was optimized to provide more than 500 mA at a cathode temperature of  $T_c > 2100$  K with a loss current below 2 mA. The highest achieved emission current was 113 % of the REXEBIS design value, which equals to 567 mA. This results in a doubled current density, or a breeding time shortened by a factor of 2, compared to the default operation regime of REXEBIS. The consequence of the high temperature operation is a significantly shortened lifetime of the installed cathode from  $\approx 10000$  h down to some 100 h. This does not fulfill the requirement of long-term stable operation for a charge breeder at ISOLDE. An investigated alternative for LaB<sub>6</sub> to minimize the necessary cathode temperature at equal emission current is the IrCe cathode. This crystal emits a current density  $\approx 50$  % higher than LaB<sub>6</sub> at equal operation temperatures, which is possible thanks to a work function 0.2 eV lower than LaB<sub>6</sub>. At higher cathode temperatures IrCe loses its advantages compared to the LaB<sub>6</sub> cathode due to the larger temperature dependency of the work function.

The progress of commission of the developed HEC<sup>2</sup> gun at BNL slowed down due to excessive loss current at the anode power supply. This prevents the electron gun from emitting higher current without further increasing the loss current at the anode. Numerical investigations of the HEC<sup>2</sup> gun show that the loss current is caused by side-emitted electrons being reflected in the gradient of the magnetic field. With the new stage-approach presented in this thesis, these reflection phenomena could be simulated and described for the first time. These simulations with this new approach are supported by an additionally developed numerical method, the particle microscope. This locally enhances the particle density in an electron beam for a better local resolution of the phase space. It is shown with these enhanced simulations that the current terminating on the anode can be reduced by 90% by an

optimally applied Wehnelt potential. To continue the commissioning of the HEC<sup>2</sup> gun at higher emission current either the cathode has to be exchanged to a sleeved cathode or the Wehnelt electrode has to be biased with a negative potential.

The particle microscope also allows investigation of the elastically reflected primary electrons (ERPE) inside collector with a sufficient high resolution. It was shown in combination with the stage-approach that these ERPE re-emit from the collector with an extraordinarily high transverse momentum, reflect at the magnetic field gradient and are finally recovered inside the collector. If the magnet does not generate a sufficient magnetic field for reflection ( $B \approx 1.5$  T in this investigated case), these ERPE are able to reach the electron gun and could cause loss current. It was also investigated if the electron beam provided by the HEC<sup>2</sup> gun can be recovered by the collector electrode. For these investigations second generation electrons, such as back-scattered electrons (BSE), must also be considered. Due to a lack of this feature in most tracing programs, a numerical tool was developed which generates a BSE start-off distribution from an incident electron beam. With this program BSE and the integrated power distribution inside the collector, especially onto the electron repeller, could be calculated in detail. During the investigations no potential configuration could be found that simultaneously minimizes ERPE, spreads out the electron beam spot on the collector electrode surface and prevents BSE from reaching non-cooled electrodes inside the collector. Therefore it is necessary to either modify the TestEBIS collector by shortening the electrodes or use a replica of the RHIC collector.

Based on the experiences from the first tests of the HEC<sup>2</sup> gun and with the developed numerical approaches and tools, a Brillouin electron gun, the MEDeGUN, was designed. In case of an assembly obeying or beating the suggested tolerances, the gun should emit an electron beam current of 1 A at a perveance of  $1 \mu\text{A}/\text{V}^{1.5}$ . The numerical proof of principle could be given, in which the MEDeGUN neglecting temperature should generate an electron beam very close to the Brillouin regime. The optimized gun geometry considering electron temperature establishes an electric field at the cathode, which does not favor current density peaks at the cathode edge and suppresses effectively side-emitted electrons. The ratio between minimum and maximum emission current density on the cathode surface is 1:1.5, which guaranties an electron beam with Wood-Saxon-shaped radial current density and prevents beam properties similar to hollow electron beam. This Brillouin-like electron beam was traced into a magnetic field of about 5 T over a distance of 37 cm. However, the numerical proof of acceptance and the investigation of the electron beam inside the solenoid was facilitated by the particle microscope and the stage-approach. The resulting current density is calculated as  $j_e = 7.5 \text{ kA}/\text{cm}^2$ . The current density to be measured, which is approximately half the value, will match the requested current density of  $j_e = 3.5 \text{ kA}/\text{cm}^2$ . This current density reduces the calculated breeding time for  $\text{C}^{6+}$  from 30 ms to 1.3 ms respectively to 2.6 ms compared to REXEBIS. MEDeGUN should be therefore capable for providing  $10^9$  ions of  $\text{C}^{6+}$  in pulsed mode with a frequency of 400 Hz.

The assembly phase of the MEDeGUN should end during autumn 2016, followed by the test and commissioning phase at the 2 T magnet of the TwinEBIS. In case of a successful commission, this gun could be operated with a 5 T magnet. Applied on REXEBIS a new family of short lived heavy RIBs becomes available.

# A Appendix

## A.1 Derivation of reflection conditions

General remarks:

- The equations/cases will be derived in cylindrical coordinates
- Motions in the radial directions are electrons increasing or decreasing their orbits relative to the z-axis, which corresponds to a diverging/de-focused or converging/focused electron beam.
- As motion in the  $\theta$ -direction both cycle-motions (gyro-motion and ExB-drift) are considered pointing into the same direction.
- The total velocity is marked with the (tot)-index.

For that derivation the electron beam properties have to be treated in two points. Point 1 is the point on the z-axis where the beam properties are known. Point 2 is the point of reflexion of the electron beam. Therefore point 1 is at a lower B-field than point 2.

The ansatz is the Hamiltonian:

$$H = \frac{p^2}{2m} + V = \frac{1}{2m} [p_r^2 + p_z^2 + p_\theta^2] + qU_{sc} + qU_{dt} \quad (A.1.1)$$

$U_{sc}$  is here the space charge potential of the electron beam and  $U_{dt}$  is the potential applied at the local drift tube.

$$\frac{1}{2m} [p_{r,1}^2 + p_{z,1}^2 + p_{\theta,1}^2] + q_1 U_{sc,1} + q_1 U_{dt,1} = \frac{1}{2m} [p_{r,2}^2 + p_{z,2}^2 + p_{\theta,2}^2] + q_2 U_{sc,2} + q_2 U_{dt,2} \quad (A.1.2)$$

$p_{z,2}^2 = 0$  is a consequence of the stopping condition at the point of reflection. Because the case of an electron propagation is considered  $q_1 = q_2 = e$ .

$$p_{r,1}^2 + p_{\theta,1}^2 + p_{z,1}^2 = p_{\theta,2}^2 + p_{r,2}^2 + e2m (U_{sc,2} - U_{sc,1} + U_{dt,2} - U_{dt,1}) \quad (A.1.3)$$

$$v_{r,1}^2 + v_{\theta,1}^2 + v_{z,1}^2 = v_{\theta,2}^2 + v_{r,2}^2 + \frac{2e}{m} (\Delta U_{sc} + \Delta U_{dt}) \quad (A.1.4)$$

$$\frac{v_{r,1}^2 + v_{\theta,1}^2}{v_{z,1}^2} = \frac{1}{v_{z,1}^2} \left[ v_{\theta,2}^2 + v_{r,2}^2 + \frac{2e}{m} (\Delta U_{sc} + \Delta U_{dt}) \right] - 1 \quad (\text{A.1.5})$$

$$\frac{\sqrt{v_{r,1}^2 + v_{\theta,1}^2}}{v_{z,1}} = \sqrt{\frac{1}{v_{z,1}^2} \left[ v_{\theta,2}^2 + v_{r,2}^2 + \frac{2e}{m} (\Delta U_{sc} + \Delta U_{dt}) \right] - 1} \quad (\text{A.1.6})$$

The acceptance angle  $\alpha$  can be defined as  $\arctan \left( \frac{\sqrt{v_r^2 + v_\theta^2}}{v_z} \right)$  or as  $\arcsin \left( \frac{\sqrt{v_r^2 + v_\theta^2}}{v_{tot}} \right)$ .

$$\alpha = \arctan \left( \frac{1}{v_{z,1}} \sqrt{\left[ v_{\theta,2}^2 + v_{r,2}^2 + \frac{2e}{m} (\Delta U_{sc} + \Delta U_{dt}) \right] - 1} \right) \quad (\text{A.1.7})$$

$$\alpha = \arcsin \left( \frac{1}{v_{tot,1}} \sqrt{v_{\theta,2}^2 + v_{r,2}^2 - v_{z,1}^2 + \frac{2e}{m} (\Delta U_{sc} + \Delta U_{dt})} \right) \quad (\text{A.1.8})$$

$v_{\theta,2} = v_\omega + v_{ExB}$ , indicating the scenario, when the cyclotron motion ( $v_\omega$ ) and the drift motion ( $v_{ExB}$ ) are pointing in the same direction.

#### A.1.0.1 Extreme case I: Free electron in magnetic bottle

This case covers the magnetic bottle approximation, which neglects space charge ( $\Delta U_{sc} = 0$ ,  $v_\theta = v_\omega$ ) and assumes magnet field lines parallel to the z-axis at point 1. Also the electron beam does not experience different potentials ( $\Delta U_{dt} = 0$ ). Eq. A.1.8 can be reduced to:

$$v_{r,1}^2 + v_{\theta,1}^2 + v_{z,1}^2 = v_{\perp,1}^2 + v_{z,1}^2 = v_{total,1}^2 = v_{\theta,2}^2 + v_{r,2}^2 = v_{\perp,2}^2 \quad (\text{A.1.9})$$

From the conservation of magnetic moment:

$$\mu_1 = \frac{mv_{\perp,1}^2}{2B_1} = \frac{mv_{\perp,2}^2}{2B_2} = \mu_2 \quad \longrightarrow \quad \frac{v_{\perp,1}^2}{v_{\perp,2}^2} = \frac{B_1}{B_2} \quad (\text{A.1.10})$$

$$v_{\perp,1}^2 + v_{z,1}^2 = v_{total,1}^2 = v_{\perp,1}^2 \frac{B_2}{B_1} \quad (\text{A.1.11})$$

$$\frac{v_{\perp,1}^2}{v_{total,1}^2} = \sin^2 \alpha = \frac{B_1}{B_2} \quad \longrightarrow \quad \alpha = \arcsin \sqrt{\frac{B_1}{B_2}} \quad (\text{A.1.12})$$

This is the acceptance angle of a magnetic bottle is according to [Geller 1996].

### A.1.0.2 Extreme case II: Perfect matching Brillouin beam

In this case  $v_\omega = 0$  (perfect injection into the catching B-field). For the sake of simplicity also all drift tubes are on the same potentials ( $\Delta U_{dt} = 0$ ). Eq.A.1.4 can be reduced to:

$$v_{r,1}^2 + v_{\theta,1}^2 + v_{z,1}^2 + \frac{2eU_{sc,1}}{m} = v_{\theta,2}^2 + \frac{2eU_{sc,2}}{m} \quad (\text{A.1.13})$$

$$v_{tot,1}^2 + \frac{2eU_{sc,1}}{m} = \left( \frac{E_{r,2}}{B_2} \right)^2 + \frac{2eU_{sc,2}}{m} \quad (\text{A.1.14})$$

$$U_{extr} = E_{kin,1} + U_{sc,1} = \frac{m}{2e} \left( \frac{E_{r,2}}{B_2} \right)^2 + U_{sc,2} \quad (\text{A.1.15})$$

This equation leads to a not directly solvable equation. With Langrange-transformation one can derive the Bursian limit for perfectly injected Brillouin beams [Akimov et al. 2001].

## A.2 Permeability of ARMCO iron

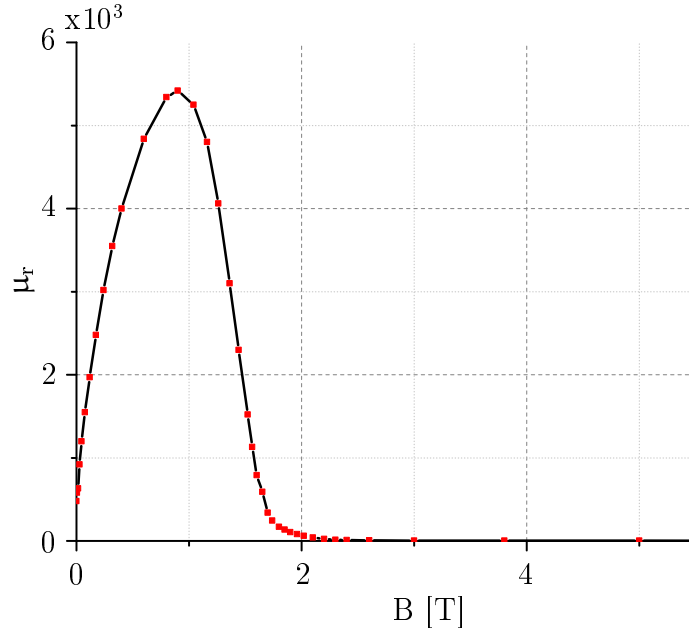


Figure A.2.1: Relative permeability of ARMCO iron [Field Precision c].

# BIBLIOGRAPHY

- P. V. Akimov, H. Schamel, H. Kolinsky, A. Ya. Ender, and V. I. Kuznetsov. The true nature of space-charge-limited currents in electron vacuum diodes: A Lagrangian revision with corrections. *Physics of Plasmas*, 8, 2001. doi: 10.1063/1.1383287.
- E. S. M. Ali and D. W. O. Rogers. Energy spectra and angular distributions of charged particles backscattered from solid targets. *Journal of Physics D: Appl. Phys.*, 41(055505), 2008.
- U. Amaldi, S. Braccini, and P. Puggioni. High Frequency Linacs for Hadrontherapy. *Rev. Accl. Sci. Tech.*, 2, 2009.
- F. Ames, R. Baartman, P. Bricault, K. Jayamanna, M. McDonald, M. Olivo, P. Schmor, and D. H. L. Yuan. Charge state breeding of radioactive ions with an electron cyclotron resonance ion source at TRIUMF. *Rev. Sci. Instrum.*, 77, 2006.
- Jr. A.S. Gilmour. *Klystrons, Traveling Wave Tubes, Magnetrons, Cross-Field Amplifiers, and Gyrotrons*. Artech House, 2011. ISBN 978-1608071845.
- A.A. Avdienko and M.D. Malev. Poisoning of LaB6 cathodes. *Vacuum*, 27(10-11), 1977.
- Y.V. Baryshev, I.V. Kazarezov, E.V. Kozyrev, G.I. Kuznetsov, I.G. Makarov, O.A. Nezhevenko, B.Z. Persov, M.A. Tiunov, V.P. Yakovlev, and I.A. Zapryagaev. A 100 MW electron source with extremely high beam area compression. *Nuclear Instruments and Methods in Physics Research*, 340(2), 1994.
- R. Becker and O. Kester. The design of an electron gun switchable between immersed and brillouin flow. *Rev. Sci. Instrum.*, 83(02A506), 2012.
- H. Beyer, H.-J. Kluge, and V. Shevelko. *X-Ray Radiation of Highly Charged Ions*. Springer, 1997. ISBN 978-3-540-63185-9.
- J. A. Bittencourt. *Fundamentals of Plasma Physics*. Springer Vienna, 2013. ISBN 978-1-4757-4030-1.
- J.L. Bobin, G. Giardino, and E. Mercier. On the Magnetic Compression of Electron Beams in E.B.I.S. or E.B.I.T. *IEEE*, 4, 1993. doi: 10.1109/PAC.1993.309600.
- M.J.G. Borge. Highlights of the ISOLDE facility and the HIE-ISOLDE project. *Nucl. Instr. Meth. B*, 2016. doi: 10.1016/j.nimb.2015.12.048.
- G. R. Brewer. Some Characteristics of a Magnetically Focused Electron Beam. *Journal of Applied Physics*, 30, 1959.
- G. R. Brewer. Focusing of high-density electron beams. Focusing of charged particles, Volume 2. Academic Press, New York and London, 1967. ISBN 978-0-12-636902-1.

- F. F. Cap. Handbook on Plasma Instabilities. Elsevier, 2012.
- T. A. Carlson, C.W. Nestor Jr., N. Wasserman, and J.D. McDowell. Calculated ionization potentials for multiply charged ions. Atomic Data and Nuclear Data Tables, 2, 1970.
- Z. Chaoui and N. Bouarissa. Positron and electron backscattering from elemental solids in the 1-10 keV energy range. Journal of physics: Condensed matter, 16, 2004.
- D. R. Chowdhury, R. Singh, A. J. Taylor, H.-T. C., and A. K. Azad. Ultrafast manipulation of near field coupling between bright and dark modes in terahertz metamaterial. Appl. Phys. Lett., (102), 2013.
- CST. Cst particle studio. <https://www.cst.com/products/cstps>, 2015. Accessed: 2016-03-29.
- E. H. Darlington and V. E. Cosslett. Backscattering of 0.5-10 keV electrons from solid targets. Journal of Physics D: Applied Physics, 5(11), 1972.
- A. Darlinkski. Measurements of Angular Distribution of the Backscattered Electrons in the Energy Range of 5 to 30 keV. Phys. stat. sol., 63, 1981.
- M. del Giorgio, J. Trincavelli, and J. A. Riveros. Backscattering of 10-35 keV Electrons from Thick Targets at Normal Incidence. X-Ray Spectrometry, 18, 1989.
- Z. Fang and S. Fukuda. Analysis of Spurious Oscillations in Klystron Due to Backstreaming Electrons from Collector. Japanese Journal of Applied Physics, 48 (116501), 2009.
- Field Precision. Setting a time step for electrons. [fieldp.com/myblog/2008/setting-a-time-step-for-electrons-in-a-strong-magnetic-field/](http://fieldp.com/myblog/2008/setting-a-time-step-for-electrons-in-a-strong-magnetic-field/), 2015a. Accessed: 2016-03-29.
- Field Precision. Field precision llc. <http://www.fieldp.com/>, 2015b. Accessed: 2016-03-29.
- Field Precision. Saturation curves for soft magnetic materials. <http://www.fieldp.com/magneticproperties.html>, 2015c. Accessed: 2016-03-29.
- M. A. Furman and M. T. F. Pivi. Probabilistic model for the simulation of secondary electron emission. Phys. Rev. ST Accel. Beams, 5(16), 2002.
- L. P. Gaffney, P. A. Butler, M. Scheck, and et al. Studies of pear-shaped nuclei using accelerated radioactive beams. Nature, 497, 2013. doi: 10.1038/nature12073.
- A. Garonna, U. Amaldi, R. Bonomi, D. Campo, A. Degiovanni, M. Garlasch, I. Mondino, V. Rizzoglio, and S. Verdu Andres. Cyclinac medical accelerators using pulsed C6+/H2+ ion sources. Journal of Instrumentation, 5(9), 2010.
- R. Geller. Electron Cyclotron Resonance Ion Sources and ECR Plasmas. CRC Press, Boca Raton, Florida, USA, 1. edition, 1996. ISBN 0750301074.
- M. Gesley and L.W. Swanson. A determination of the low work function planes of LaB6. Surface Science, 146, 1984.
- Dan M. Goebel and R. M. Watkins. Compact lanthanum hexaboride hollow cathode. Rev. Sci. Instrum. , 083504 (2010), 81, 2010.

- B. Goldstein and D.J.Szostak. Characterization of clean and oxidized (100)LaB6. *Surface Science*, 74, 1978.
- P. L. Gruzin, Yu. V. Petrikin, and A. M. Rodin. Measurement of the spectral and angular distributions of back-scattered electrons. *Atomnaya Énergiya*, 33(3), 1972.
- M. F. Gu. The Flexible Atomic Code: V. Electron Impact Ionization. *Astrophys. J.*, 582, 2003.
- L. A. Hageman and D. M. Young. *Applied Iterative Methods*. Dover Publications, 1. edition, 2004. ISBN 9780486434773.
- G. Herrmann. Optical Theory of Thermal Velocity Effects in Cylindrical Electron Beams. *J. Appl. Phys.*, 29, 1958.
- A.I. Hershcovitch and A.E. Kponou. Backscattering of electrons in EBIS collectors. *Nuclear Instruments and Methods in Physics Research*, A330, 1993.
- St. Humphries. *Charged Particle Beams*. Dover Pubn Inc, 2013. ISBN 978-0486498683.
- K. L. Jensen. Measurement and analysis of thermal photoemission from a dispenser cathode. *Phys. Rev. STAB*, 6, 2003.
- Y. S. Kim and R. H. Pratt. Direct radiative recombination of electrons with atomic ions: Cross sections and rate coefficients. *Phys. rev. A*, 27(6), 1983.
- G. I. Kuznetsov. High temperature cathodes for high current density. *Nuclear Instruments and Methods in Physics Research A*, 340, 1994.
- G. I. Kuznetsov. Cathodes for Electron Guns. *Physica Scripta*, T71, 1997.
- G. I. Kuznetsov. IrCe Cathodes For EBIS. *Journal of Physics: Conference Series*, 2, 2004.
- J. J. Lander. Auger Peaks in the Energy Spectra of Secondary Electrons from Various Materials. *Phys. Rev*, 91, 1953.
- E.P. Lee and R.K.Cooper. General Envelope Equation For Cylindrically Symmetric Charged-Particle Beams. *Particle Accelerators*, 7, 1976.
- C. Litwin, M.C. Vella, and A. Sessler. Linear electrostatic instability of the electron beam ion source. *Nuclear Instruments and Methods*, 198(2-3), 1982.
- W. Lotz. Electron-impact ionization cross-sections for atoms up to  $Z=108$ . *Zeitschrift für Physik*, 232(2), 1970.
- T. Matsukawa, R. Shimizu, and H. Hashimoto. Measurements of the energy distribution of backscattered kilovolt electrons with a spherical retarding-field energy analyser. *J. Phys D: Appl. Phys.*, 7, 1974.
- R. Mertzig. Untersuchungen zur Physik von in hochdichten EBIS-Elektronenstrahlen gespeicherten Eisenionen. Master's thesis, TU Dresden, Germany, 2011.
- Molflow+. A monte-carlo simulator package developed at CERN. <https://test-molflow.web.cern.ch/>, 2016. Accessed: 2016-03-29.



- A. Mueller and E. Salzborn. Scaling of cross sections for multiple electron transfer to highly charged ions colliding with atoms and molecules. *Physics Letters A*, 62 (6), 1977.
- M. V. Nezlin. *Physics of Intense Beams in Plasmas*. CRC Press, Boca Raton, Florida, USA, 1993. ISBN 978-0750301862.
- NIST. Nist atomic spectra database ionization energies form. <http://physics.nist.gov/PhysRefData/ASD/ionEnergy.html>, 2015. Accessed: 2016-03-29.
- Onlinelib. Online library of ion potentials. <https://project-ionpotentials.web.cern.ch/project-Ionpotentials>, 2015. Accessed: 2016-03-29.
- A. Pikin, A. Kponou, and L. Snydstrup. Optical, Thermal and Stress Simulations of a 300-kwatt Electron Collector. Brookhaven Nat. Lab, 2006.
- A. Pikin, J. G. Alessi, E. N. Beebe, D. Raparia, and L. Snydstrup. Optics modification of the electron collector for the Relativistic Heavy Ion Collider Electron Beam Ion Source. 2012.
- A. Pikin, E. Beebe, and D. Raparia. Simulation and optimization of a 10 A electron gun with electrostatic compression for the electron beam ion source. *Rev. Sci. Instrum.*, 84(3), 2013.
- A. Pikin, J. Alessi, E. Beebe, A. Shornikov, R. Mertzig, F. Wenander, and R. Scrivens. First test of BNL Electron Beam Ion Source with high current density electron beam. Brookhaven Nat. Lab, 2014.
- F. Le Pimpec, F. King, R.E. Kirby, and M. Pivi. Secondary Electron Yield Measurements of TiN Coating and TiZrV Getter Film. Technical Report SLAC-TN-03-052, Stanford Linear Accelerator Center, Menlo Park, CA (US), 2003. Technical Report.
- Python. <https://www.python.org/>, 2016. Accessed: 2016-03-29.
- R. Rao and O. Kultashev. IrCe cathodes as high-density emitters in electron beam ion sources. *Measurement Science and Technology*, 8(2), 1997.
- A. Shornikov, A. Pikin, R. Scrivens, and F. Wenander. Design study of an upgraded charge breeder for ISOLDE. *Nucl. Instr. Meth. B*, (317), 2013.
- A. Shornikov, E. N. Beebe, R. C. Mertzig, A. Pikin, and F. Wenander. High performance charge breeder for HIE-ISOLDE and TSR ISOLDE applications. *AIP Conf. Pro.*, (1640), 2015.
- A. Shornikov, R. C. Mertzig, M. Breitenfeldt, A. Lombardi, F. Wenander, and A. Pikin. Parametric study of a high current-density EBIS Charge Breeder regarding Two Stream plasma Instability (TSI). *Nucl. Instr. Meth. B*, 2016.
- A. Singh, A. Valfells, C. B. Robey, J. Goldstein, M. J. Kolander, and V. L. Granatstein. Advancements in Codes for Computer Aided Design of Depressed Collectors and Tracing of Backscattered Electrons-Part I: Improvements in Modeling of the Physics of Secondary Electron Emission and Backscattering. *IEEE Transactions on plasma science*, 30(3), 2002.
- P. Staub. Bulk target backscattering coefficient and energy distribution of 0.5-100keV electrons: an empirical and synthetic study. *Journal of applied physic*, 27, 1994.

- E. J. Sternglass. Backscattering of Kilovolt Electrons from Solids. *Phys. Rev.*, 95 (2), 1954.
- C. Guy Suits and H. E. Way. *Electrical Discharge: With Contributions in Memoriam Including a Complete Bibliography of His Works*. Elsevier, 1. edition, 1961. ISBN 9780080093567.
- A. Valfells, A. Singh, M. J. Kolander, and V. L. Granatstein. Advancements in Codes for Computer Aided Design of Depressed Collectors and Tracing of Backscattered Electrons-Part II: Improvements in Modeling of the Physics of Secondary Electron Emission and Backscattering. *IEEE Transactions on plasma science*, 30(3), 2002.
- D. von Lindenfels, M. Wiesel, D. A. Glazov, A. V. Volotka, M. M. Sokolov, V. M. Shabaev, G. Plunien, W. Quint, G. Birkel, A. Martin, and M. Vogel. Experimental access to higher-order Zeeman effects by precision spectroscopy of highly charged ions in a Penning trap. *Phys. rev. A*, (87), 2013.
- R. Vondrasek, A. Levand, R. Pardo, G. Savard, and R. Scott. Charge breeding results and future prospects with electron cyclotron resonance ion source and electron beam ion source. *Rev. Sci. Instrum.*, (83), 2012.
- M. Vretenar, A. Dallochio, V. Dimov, M. Garlaschè, A. Grudiev, A. Lombardi, S. Mathot, E. Montesinos, and M. Timmins. A Compact High-Frequency RFQ for Medical Applications. *LINAC14*, 2014.
- F. Wenander. Charge Breeding of Radioactive Ions. Technical Report CERN-2013-007, CERN, Geneva (Switzerland), 2014. Technical Report.
- U. Werner, H. Bethge, and J. Heydenreich. An analytic model of electron backscattering for the energy range of 10-100 keV. *Ultramicroscopy*, 8, 1982.
- J. S. Williams and J. M. Poate. *Ion Implantation and Beam Processing*. Elsevier Inc., 1984. ISBN 978-0-12-756980-2.
- B.H. Wolf, J. Cederkäll, O. Forstner, F. Wenander, F. Ames, K. Reisinger, L. Liljeby, Ö. Skeppstedt, B. Jonson, G. Nyman, and The REX-ISOLDE Collaboration. First radioactive ions charge bred in REXEBIS at the REX-ISOLDE accelerator. *Nucl. Instr. Meth. B*, 204, 2003.
- R. K. Yadav and R. Shanker. Energy and angular distributions of backscattered electrons from collisions of 5 keV electrons with thick Al, Ti, Ag, W and Pt targets. *PRAMANA - journal of physics*, 68(3), 2007a.
- R. K. Yadav and R. Shanker. Contribution of backscattered electrons to the total electron yield produced in collisions of 8 - 28 keV electrons with tungsten. *PRAMANA - journal of physics*, 68(3), 2007b.
- V. A. Zaytsev, S. Tashenov, A. V. Maiorova, V. M. Shabaev, and Th. Stoeckler. Parity nonconservation effect in the resonance elastic electron scattering on heavy he-like ions. *J. Phys. B: At. Mol. Opt. Phys.*, (48), 2015.
- G. Zschornack, F. Grossmann, V.P. Ovsyannikov, A. Schwan, F. Ullmann, E. Tanke, and P. Urschuetz. Status of Electron Beam Ion Sources for Particle Therapy. *HIAT09*, 2009.

## List of thesis related publications

1. Electron beam simulation from gun to collector: Towards a complete solution, R. Mertzig, A.Pikin, E. Beebe, A. Shornikov, F. Wenander, EBIST 2014, AIP Conf. Proc. 1640, 28, <http://dx.doi.org/10.1063/1.4905397>, (2015)
2. First test of BNL Electron Beam Ion Source with high current density electron beam, A.Pikin, J. Alessi, E. Beebe, A. Shornikov, R. Mertzig, F. Wenander, R. Scrivens, EBIST 2014, (2015)
3. High Performance Charge Breeder for HIE-ISOLDE and TSR@ISOLDE Applications, A. Shornikov, E. Beebe, R. Mertzig, A.Pikin, F. Wenander, EBIST14, <http://dx.doi.org/10.1063/1.4905396>, (2015)
4. Parametric study of a high current-density EBIS Charge Breeder regarding Two Stream plasma Instability (TSI), A. Shornikov, R. Mertzig, Martin Breitenfeldt, Alessandra Lombardi, F. Wenander, A.Pikin, NIM B, <http://dx.doi.org/10.1016/j.nimb.2015.12.008>, (2016)
5. A high-compression electron gun for  $C^{6+}$  production: design and simulations, to be published (NIM A, B or Journal of Instruments)
6. The TwinEBIS setup: machine description, to be published (NIM A, B or Journal of Instruments)
7. The TwinEBIS setup: commissioning results, to be published (NIM A, B or Journal of Instruments)

# Danksagung

Hiermit möchte ich in willkürlicher Reihenfolge und Länge allen danken, die mir ihre Unterstützung in verschiedenster Weise bei der Anfertigung meiner Dissertation gewährt haben. Zu jeder Zeit erachtete ich es als sehr großes Privileg und hohe Ehre mit solch einer Dissertation betraut zu werden und an diesen erlauchten Ort der Wissenschaft wirken zu dürfen. Herrn Günter Zschornack, Herrn Jürgen Fassbender und Herrn Fredrik Wenander danke ich besonders für die wissenschaftliche Förderung. Diese Dissertation würde ohne ihren Einsatz, ihre Überzeugungskraft und das gegenseitige sowie mir entgegengebrachte Vertrauen nicht erreicht werden können.

Da Promovieren auch viele Fehlschläge, scheinbar unlösbare Probleme und viel "pain&suffering" beinhaltet, bedanke ich mich besonders bei meiner HSL - Arbeitsgruppe am CERN für Zuspruch, Ratschläge und die tatkräftige Unterstützung.

Fredrik Wenander danke ich für die zahlreichen Inspirationen und Diskussionen, die essentiell zur Dissertation betrug. Seine Tür war stets geöffnet und er fand immer Zeit für meine Belange, was ich nicht als selbstverständlich erachte und immer sehr geschätzt habe. Bei Martin Breitenfeldt möchte ich mich für die vielen hilfreichen Diskussionen, Feedbacks und die große technische Unterstützung bedanken. Seine Besonnenheit angesichts (un-)vermeidbarer Katastrophen im Physikeralltag werde ich mir stets zum Vorbild nehmen. Großen Dank gilt auch Andrey Shornikov. Durch seine inspirierenden Eingebungen und Unterstützung konnte mein Beitrag zum HEC<sup>2</sup>-Projekt (auch direkt an der Beamline) und meine numerische Arbeit diese Tiefe erreichen. Desweiteren bedanke ich mich auch bei Johanna, Sebastien und Julien, die den Laboralltag auf ein sehr vornehmes Niveau gehoben haben.

Desweiteren möchte ich mich bei Richard, Alessandra, Jacques, Ville, Detlef, Jean-Baptiste, Christian, Michael, Stefano und Marc für die stets hervorragende Zusammenarbeit und Hilfe bedanken. Einen besondern Dank gilt auch Michal Husejko für die Unterstützung zur Etablierung des CST-Clusters am CERN, der die 3D-Elektronenstrahlberechnungen für mich nutzbar gemacht hat.

Einen grossen Dank gilt auch der EBIS-Arbeitsgruppe inklusive den Werkstätten am BNL, insbesondere Sasha, Ed, Bob, Dan und James. Auch möchte ich mich beim DREEBIT-Team, insbesondere bei Mike Schmidt, für die exzellente Zusammenarbeit und den regen wissenschaftlichen Austausch bedanken. Desweiteren möchte ich mich bei Herrn Reinard Becker bedanken. Durch seine Fürsprache wurde aus eine kleine Nebenrechnung zum Zeitvertreib ein wissenschaftliches Projekt.

Weiterhin möchte ich mich auch bei Pascal Hermes, Andy Langner und Riku Silvola für Diskussionen und Aktivitäten dies- und jenseits der Physik, durch die die Zeit hier fast freizeitlich wirkt, bedanken. Auch bei Tania De Melo Mendonca danke ich mich für pseudo-allfreitagliche Diskussionen jenseits der Physik und das grenzwertige Schlemmen zu Dienstag.

Auch danke ich mich sehr bei Rachel Sandler für ihr allzeit offenes Ohr, ihre große Hilfe bei den vielen kleinen Dingen im Doktorandenleben und die vielen Abenteuer um den Globus, speziell in den erbarmungslosen Wüsten des wilden Westens.

Zuletzt danke ich mich sowohl bei meinen Eltern Uwe und Marina Mertzig als auch bei meiner Schwester Katharina für und meinen Bruder Georg für die sehr verständnisvolle und unermüdliche Unterstützung während der ganzen Zeit.

# Erklärung

Hiermit versichere ich, dass ich die vorliegende Arbeit ohne unzulässige Hilfe Dritter und ohne Benutzung anderer als der angegebenen Hilfsmittel angefertigt habe. Die aus fremden Quellen direkt oder indirekt übernommenen Gedanken sind als solche kenntlich gemacht. Die Arbeit wurde bisher weder im Inland noch im Ausland in gleicher oder ähnlicher Form einer anderen Prüfungsbehörde vorgelegt.

Robert Mertzig  
Dresden, Mai 2016

